Receptor Mediated Adhesion of Circulating Cells

In Immune Cell Interaction and Cancer

A Dissertation

Presented to the Faculty of the Graduate School

of Cornell University

In Partial Fulfillment of the Requirements for the Degree of Doctor of Philosophy

by

Thong Cao

August 2019

Receptor Mediated Adhesion of Circulating Cells In Immune Cell Interaction and Cancer

Thong Cao

Cornell 2019

Circulating tumor cells (CTCs) disseminating from primary tumor sites travel to distant organs and form secondary tumor sites, known as metastasis. After leaving the primary tumor microenvironment, CTCs enter the circulatory system where they routinely interact with immune cells. This interaction can paradoxically result in both limiting or promoting the metastatic potential of CTCs. The final steps of metastasis involve CTCs invaginating into the underlining tissue and forming secondary tumor sites. One plausible mechanism of CTCs leaving the circulatory system involves a similar process to leukocyte homing - selectin-mediated interaction. The scope of the work presented here can be divided into two parts: (a) exploiting the naturally occurring immune response called NETosis when neutrophils come into contact with cancer cells as a form of cancer therapy, and (b) gaining a better understanding of the mechanism of selectin-ligand interaction that playing a pivotal role in cancer metastasis and leukocyte homing.

Immunotherapy is an emerging powerful clinical strategy for cancer therapy. NETosis is an innate immune response elicited by activated neutrophils to fight microbial infections. Activated neutrophils release DNA fibers decorated with anti-microbial proteins called neutrophil extracellular traps (NETs) into the extracellular space to trap

and kill surrounding microbes. Here, we show tumor-derived IL-8 released by cancer cells also activates the release of NETs. Until now, there have been no existing technologies that leverage NETs as an anti-tumor drug delivery vehicle. In this study, we describe the re-engineering of neutrophils to express an apoptosis-inducing chimeric protein, supercharged eGFP-TRAIL, on NETs that can ensnare and kill tumor cells while retaining all of their anti-microbial capabilities. We observed significant TRAIL-induced apoptosis in tumor cells captured by TRAIL-decorated NETs. This work demonstrates NETs as a promising technology to deliver protein in response to local cytokine signals.

The 3-member (E-, P-, L-) selectin family of cell adhesion molecules facilitates initial leukocyte tethering and subsequent cell rolling during the early stages of the inflammatory response via binding to glycoproteins expressing sialyl Lewis^{X} and sialyl Lewis^{A} (sLe$^{X/A}$) to sites of inflammation and trauma. The extracellular microenvironments at these sites often become acidic. We investigated the influence of slightly acidic pH on the binding dynamics of selectins (P-, L-, and E-selectin) to P-selectin glycoprotein ligand-1 (PSGL-1) via computational modeling (molecular dynamics) and experimental rolling assays under shear in vitro. The P-selectin/PSGL-1 binding is strengthened at acidic pH, as evidenced by the formation of a new hydrogen bond (seen computationally) and the observed decrease in the rolling velocities of model cells. In the case of L-selectin/PSGL-1 binding dynamics, the binding strength and frequency increase at acidic pH, as indicated by the greater cell-rolling flux of neutrophils and slower rolling velocities of L-selectin-coated microspheres, respectively. The cell flux is most likely due to an increased population of L-selectin in

the high-affinity conformation as pH decreases, whereas the velocities are due to increased L-selectin/PSGL-1 contacts. In contrast to P- and L-selectin, the E-selectin/PSGL-1 binding does not exhibit significant changes at acidic pH levels, as shown both experimentally and computationally.

We also investigated the allosteric influence of E-selectin's structure to ligand binding mechanics. Existing crystal structures of the extracellular lectin/EGF-like domain of E-selectin complexed with sLe^X have revealed that E-selectin can exist in two conformation states, a low affinity (bent) conformation, and a high affinity (extended) conformation. The differentiating characteristic of the two conformations is the interdomain angle between the lectin and the EGF-like domain. Using molecular dynamics (MD) simulations we observed that in the absence of tensile force E-selectin undergoes spontaneous switching between the two conformational states at equilibrium. A single amino acid substitution at residue 2 (serine to tyrosine) on the lectin domain favors the extended conformation. Steered molecular dynamics (SMD) simulations of E-selectin and PSGL-1 in conjunction with experimental cell adhesion assays show a longer binding lifetime of E-selectin (S2Y) to PSGL-1 compared to wildtype protein. The findings in this study advance our understanding into how the structural makeup of E-selectin allosterically influences its adhesive dynamics

.

BIOGRAPHICAL SKETCH

Thong Cao emigrated from Vietnam to the United States at the age of seven and grew up in Northern California with his parents. He attended University of California - Davis, where he earned a Bachelor's of Science in Biochemistry. After his undergraduate studies, he accepted a research associate position at Santa Cruz Biotechnology (SCBT). His primary role was the purification and titer quantification of polyclonal and monoclonal antibodies from goat and rabbit blood serum, respectively. After two years at SCBT, he resigned in order to continue his study at Cornell University, earning a Master's of Engineering in Biomedical Engineering while doing research in the King Lab. He went on to work in the King Lab as a research assistant. He was developing a scalable selectin-based hematopoietic stem cell enrichment device with the collaboration of a New York state-based start-up company, CellTraffix (Rochester, NY) that was funded by the United States Army. As a Ph.D. candidate, with Professor Michael King as the primary advisor, Thong's doctoral work looked at re-engineering human neutrophils to express a tumor cell apoptosis-inducing protein called Trail on NETs to ensnare and kill disseminating tumor cells. Thong's passion for teaching in conjunction with his research excellence had earned him the U.S Department of Education GAANN Fellowship. After earning a Ph.D. in Biomedical Engineering, Thong wishes to embark on a career in the development of clinically relevant, life changing therapeutics as a research scientist.

I would like to dedicate this work…

To my mom and dad for their unwavering love and sacrifice without whom none of this would have ever been possible.

To Laura and Tony for their unending support and faith in me. And to show me that the best sister and brother you can hope for do not have to be by birth.

To Chopper, my dear pal. I loved you and not a single day that I don't miss you.

ACKNOWLEDGMENTS

First and foremost, I would like to thank my advisor, Professor Michael King for his constant guidance and absolute faith in me. Without him, this academic journey would not have been possible. I drove from California to Ithaca, New York without a clear plan and a hope of finding something. You gave me a chance when few would. I feel very fortunate to have found an advisor who consistently inspires me to become a successful and confident scientist and has complete confidence in me even when I have so little. I see you as a life-long mentor and friend. Thank you.

I would like to send special thanks to my committee members, Dr. Matthew P. DeLisa and Dr. Matthew J. Paszek for their guidance regarding my thesis work.

I would like to thank a very special person, Belinda Floyd, for all the headache I have put her through. Belinda is truly a blessing for everyone in the Biomedical Engineering program who loves her graduate students almost as much as her own children.

I would like to thank all King Lab members, future and present. My gratitude goes to Jeffrey Mattison for the endless orders and for drawing blood longer after he has left the lab. I would like to thank my wonderful lab mates: Dr. Kuldeep Rana, Dr. Tait Takitani, Dr. Yue Geng, Dr. Michael Mitchell, Dr. Andrew Hughes, Dr. Jiahe Li, Dr. Siddharth Chandasekaran, Dr. Anne Rocheleau, Dr. Jocelyn Marshall, Dr. Kevin Anderson, Nerymar Ortiz-Otero, Korie Grayson, and Zeinab Mohamed for keeping lab fun and entertaining and for the stimulating scientific conversations.

I would like to thank Dr. Jean Carlos-Cruz, Dr. Jason Jones, Dr. Jose Rios and Dr. Kirk Samaroo. I cannot thank enough for meeting and becoming life-long friends with these guys. Thank you to the Cornell/Ithaca community for the many wonderful memories.

Last, but certainly not least, a very special thanks to Lauren Hapach. I cannot be more fortunate to have met you at Cornell. You are my love and my rock. You make me want to go out there to do my best so I can make you proud. I love you.

TABLE OF CONTENTS

LIST OF FIGURES AND TABLES

CHAPTER 1

CHAPTER 2

CHAPTER 3

CHAPTER 1

Portions of this chapter were published in *Annual Review of Biomedical Engineering (1)*.

INTRODUCTION

Early diagnosis in most types of cancer remains challenging due to the lack of symptoms in the early stage and the small size of the primary tumor. For instance, mammography, the most common screening tool for the detection of early-stage breast cancers, can detect on average 80–90% of breast cancers at an early stage in women without symptoms, and reduces the risk of death by 15% in all women screened. Mammography is a somewhat accurate screening tool, but the rate of false negatives remains around 20% and the rate of false positives is more than 30% *(2)*. Mammography also detects indolent localized cancers that may not require treatment *(3)*. In studies of early detection of lung cancer, computed tomography (CT) reduces mortality by 7–20% but has a low screening accuracy (96% false positive) *(4)*. Moreover, the radiation from CT scans gives rise to long-term risk for some cancers *(5)*. In another example, prostate-specific antigen (PSA) has been used for the early detection of prostate cancer, but the overdiagnosis rate and whether it contributes to a reduction in deaths remain unknown *(6)*.

Before cancer metastasizes, cancer cells are disseminated from the primary tumor site to remote sites via blood circulation (Figure 1.1). Circulating tumor cells (CTCs) were first discovered in 1869 during an autopsy of a metastatic cancer patient by Ashworth *(7)*, who observed that the cancer cells in a site distant from the tumor resembled the original

tumor. This observation implied that in order for the cancer cells to have reached the distant site, they would have had to be transported there through the blood. Ever since, CTCs have been considered an important factor in metastasis and a primary cause of deaths attributable to cancer.

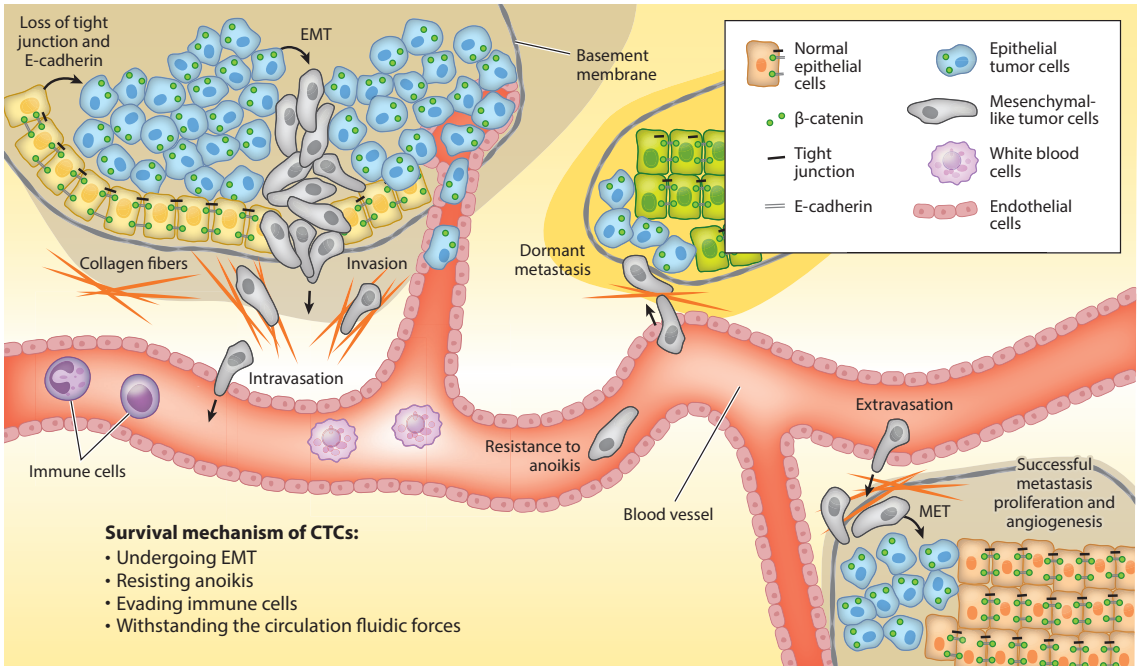

Figure 1.4: Cancer metastasis involving the detachment of circulating tumor cells (CTCs) from the primary tumor and their invasion into the circulation, survival in the circulation, extravasation, and proliferation. Abbreviations: EMT, epithelial-to-mesenchymal transition; MET, mesenchymal-to-epithelial transition. Adapted from E. Lin, T. Cao et al. Annu. Rev. Biomed. Eng. 2018. 20:329–52.

Metastasis can be described as a five-step process (Figure 1.1): (*a*) Cancer cells detach from the primary tumor, (*b*) invade the blood circulation, (*c*) survive in circulation, (*d*) extravasate into distant organs, and (*e*) proliferate at the secondary site(s). CTCs found in

the peripheral blood of cancer patients often indicate metastasis *(8, 9)*. CTCs have clinical potential as prognostic biomarkers to predict treatment efficacy, progression-free survival, and overall survival in patients *(10–14)*. There is increasing evidence that CTCs that entered the circulation could be a good surrogate biomarker not only for prognosis but also for detection and monitoring of disease *(10, 15–18)*. The potential use of CTCs in many research areas has acquired great momentum in recent years. Developments include the selection of neoadjuvant and adjuvant therapy, detection of recurrent disease, examination of pharmacodynamic biomarkers, and identification of novel therapeutic targets, enabling a personalized therapeutic approach *(13, 14, 19–22)*.

Compared with traditional tissue biopsy, which is an invasive procedure and presents a static "snapshot" of the tumor, liquid biopsy involving CTC and/or circulating tumor DNA (ctDNA) analyses is noninvasive and can provide real-time information about the disease burden, the evolution of the tumor, and the tumor's heterogeneity *(23)*. More specifically, CTCs contain in- formation related to the initiation of metastasis, whereas ctDNA is more representative of the bulk of the metastatic tumor. Although intratumor heterogeneity is widely recognized as a primary way to reduce the effectiveness of molecular targeted therapy, thorough investigation of such heterogeneity remains challenging due to the difficulty of performing multiple tissue biopsies to acquire spatial and temporal samples *(24)*. The molecular and genetic profiling of CTCs represents a possible alternative to study tumor subpopulations during disease progression and to monitor changes in response to therapy.

CTCs are strong prognostic and diagnostic factors because they are present in early disease progression *(25)*. Several studies have detected CTCs in blood in early-stage cancer. For example, Stott et al. *(15)* detected CTCs in patients with localized prostate cancer, Zhang et al. *(25)* extracted CTCs from patients with early-stage lung cancer, and Murlidhar et al. *(26)* showed the presence of CTCs in early-stage lung cancer not only in peripheral blood but also in pulmonary veins.

CTC enumeration is a powerful tool in early screening, monitoring of disease progression and treatment, and indication of cancer relapse *(27)*. CTCs also have great potential to provide clinical and therapeutic information when combined with downstream analysis. Some studies have suggested that CTC enumeration alone is not sufficient to guide therapeutic decisions *(28)* but that molecular analysis of CTCs should be performed to determine how to target therapy *(29)*. Mutations in genes such as *KRAS*, *EGFR*, and *HER2* and in the estrogen receptor (ER) genes can be identified through the screening of CTCs *(30)*. The differences between individual CTCs and the primary tumor may enable new insights through the comparison of CTC genomes with those of the primary and metastatic tumors *(27)*. RNA profiling or sequencing on single or pooled CTCs can provide extensive information to identify signaling pathways and splice variants relevant to metastatic potential and therapy resistance *(31)*. Ex vivo culture of patient-derived CTCs can be adopted in tests of drug efficacy *(32)* and can enable multiplexed proteomic analyses of CTCs *(33)*.

1.1 CIRCULATING TUMOR CELLS AS A THERAPEUTIC TARGET

Cancer therapies that target CTCs are compelling, considering that more than 90% of deaths due to cancer are related to metastasis *(34)*. Metastasis begins when a small population of tumor cells, namely CTCs, break away from the primary tumor site and intravasate into the peripheral circulation *(35, 36)*. Once in the circulation, CTCs travel to distant sites where they tether, roll, and eventually extravasate into the underlying tissue in a selectin-dependent manner *(37)*. Ultimately, metastasizing cancer cells can form secondary tumors. Although conventional surgery and radiation may be effective at excising primary tumors, secondary tumors are much smaller and more difficult to detect until they prove fatal. Therefore, the development of technologies that directly target CTCs before they have the chance to form secondary tumors could potentially reduce metastasis-related deaths.

Many cancer types metastasize into the lymph nodes, as well as the circulatory system *(38)*. At first glance, tumor cells engrafting in the lymph nodes seems counterintuitive, since the lymph nodes are epicenters of immune cell congregation and immunosurveillance. However, tumor cells can release tumor-associated factors that convert the immunogenic microenvironment of the lymph nodes into an immunosuppressive state that can tolerate and even promote the localization of metastasizing cancer cells *(39)*. The presence of cancer cells in the lymph nodes necessitates therapeutics that can not only selectively target cancer cells in lymph nodes but also reverse the immunosuppressive state of the lymph nodes.

1.2 THERAPEUTICS DIRECTED AT CIRCULATING TUMOR CELLS

Because tumor metastasis is responsible for more than 90% of cancer-related deaths and most distant metastases are formed by tumor cells leaving the primary tumor microenvironment and intravasating into the circulatory system, anti-CTC therapeutics have the potential to neutralize cancer metastasis and reduce cancer-related deaths *(40)*. A straightforward approach to reducing metastasis and cancer-related deaths is to remove CTCs from the circulation of metastasizing patients. However, two main challenges faced by all CTC-capturing techniques are the rarity of these cells and the lack of a unique identifiable marker. The number of CTCs is relatively low in circulation—around 1–100 CTCs per milliliter of blood or approximately 1–100 CTCs per 10^6 –10^7 leukocytes *(8, 41)*. Existing CTC isolation techniques, including gradient centrifugation, microfiltration, and EpCAM antibody targeting, are hampered by the limited volume of blood that can be processed per trial (10–50 mL) and by a high background level of contaminating leukocytes that routinely reduces the purity of the CTCs to below 1% *(17, 42–44)*. Therefore, any CTC selection technique must be able to process large volumes of blood while attaining high purity.

A recently proposed CTC removal process consisting of a sequential combination of two semiautomated technologies—leukapheresis followed by counterflow centrifugation elutriation— aims to address the above-described limitations *(45, 46)*. Leukapheresis is a well-established density filtration technology that is used clinically to harvest peripheral blood mononuclear cells (PBMCs) from whole blood. Importantly, it can process the entire blood volume of a patient multiple times over in a single session. Because CTCs

and PBMCs have comparable density and size, leukapheresis has been used to isolate CTCs from metastatic patients, yielding comparable results to other CTC enrichment techniques *(41, 47)*.

Following leukapheresis, the CTC isolation purity can be further improved with elutriation. Elutriation is a process that is used to separate the subpopulations, primarily monocytes, of isolated PBMCs by their size, and has been used to purify monocytes from dendritic cells (DCs) for immunotherapy applications *(48, 49)*. The size of CTCs can be similar to that of monocytes. Thus, the enriched population of monocytes after elutriation is expected to contain CTCs as well. The combination of leukapheresis and elutriation of 10 L of blood spiked with CaOV-3 tumor cells yielded enrichment of up to 78% CTCs *(45)*. CTCs with established surface markers (EpCAM, cytokeratin, and $CD45^{-}$) can further be enriched using fluorescence-activated cell sorting *(50, 51)*.

An in vivo photoacoustic flow cytometry system was recently developed to detect and ablate CTCs in tumor-bearing mice in a label-free manner *(52–54)*. The advantage of this technology is that it can process large volumes of blood; specifically, 5 L of blood can be processed in under 2 h. Also, the technique has a high threshold sensitivity, as it is able to detect a single CTC from 10^7 normal blood cells *(55–57)*. However, this technique has been tested only in a melanoma-bearing mouse model *(52)*.

1.3 TRAIL-BASED CIRCULATING TUMOR CELL THERAPEUTICS

After CTCs have entered the circulatory system, they travel to distant organs, extravasate out of blood vessels and into the underlying tissue and form secondary tumors. Similar to circulating leukocytes, CTCs use interactions between selectins and ligands to tether, roll, and arrest onto the vascular wall before subsequent extravasation into the distal site *(37, 58–60)*. This knowledge of the molecular mechanisms involved in CTC extravasation has led to the development of a selectin-based implantable shunt device that can capture and eradicate CTCs *(61)*. The device is a microtube with its luminal surface functionalized with E-selectin molecules and tumor necrosis factor–related apoptosis-inducing ligand (TRAIL) to facilitate CTC rolling and eventual tumor cell apoptosis, respectively.

TRAIL has generated extensive research attention as a cancer therapeutic because it can selectively induce apoptosis in a variety of tumor cell lines while sparing most normal cells. TRAIL induces cell death in target cells through binding to death receptors DR4 and DR5, giving rise to the extrinsic caspase-dependent apoptosis signaling pathway *(62)*. Although the clinical success of TRAIL therapy for solid tumors has been somewhat limited because some cancer cell types exhibit varying degrees of TRAIL resistance, TRAIL-resistant cancer cells become more sensitive to TRAIL after they have detached from the extracellular matrix *(63)*. Moreover, tumor cells become more "sensitized" to TRAIL when exposed to fluid shear stress *(64)*. In the circulatory system, where wall shear stress can range from 0.5 to 4.0 dyne/cm^2 in the venous circulation and up to 30.0 dyne/cm^2 in the arterial circulation, CTCs experience a significantly higher shear environment than cells in the primary tumor site *(65)*. Furthermore, CTC sensitivity to

caspase-dependent apoptosis is positively correlated with fluid shear stress level and exposure time *(64, 66, 67)*. Thus, the natural detachment of metastatic CTCs from the primary tumor microenvironment and into the higher shear environment of the circulatory system makes them especially vulnerable to TRAIL-based therapy.

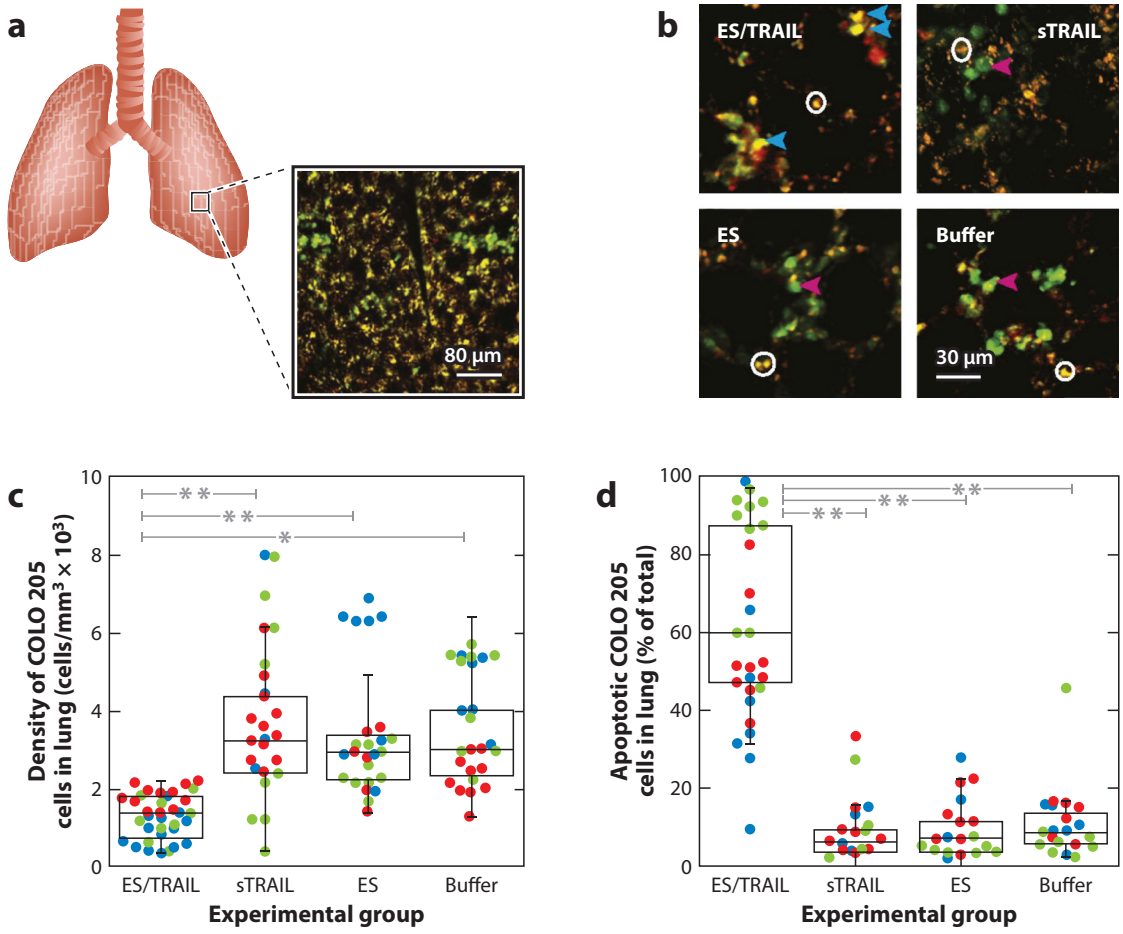

Figure 1.5: E-selectin (ES)- and tumor necrosis factor–related apoptosis-inducing ligand (TRAIL)-coated liposomes induce apoptosis of lodged COLO 205 cells in the lungs. (a) Schematic of a mouse lung and a two-photon excited fluorescence (2PEF) image of lodged COLO 205 cells (green) in the lung tissue (yellow). (b) 2PEF images of lodged COLO 205 cells (green) stained with Annexin V apoptosis marker (red) in different

*experimental groups in lung tissue. Red and blue arrows mark apoptotic and nonapoptotic cells, respectively. White circles mark regions of autofluorescence. (c) Arrested COLO 205 cell density in lung tissue of different experimental groups. (d) Percentage of apoptotic COLO 205 cells of different experimental groups. In panels c and d, red, green, and blue dots represent distinct animals in the studies. Gray asterisks represent statistical significance: *p < 0.01, **p < 0.0001 (one-way ANOVA with Tukey posttest). Bars represent (from top to bottom): maximum, Q3, median, Q1, and minimum. Abbreviation: sTRAIL, soluble TRAIL. Adapted from E. Lin, T. Cao et al. Annu. Rev. Biomed. Eng. 2018. 20:329–52.*

More recently, liposomes functionalized with TRAIL and E-selectin molecules readily attach onto circulating leukocytes under flow, thus turning these leukocytes into "unnatural killer cells" within the circulatory system that can induce apoptosis in any CTCs they come into contact with *(68, 69)*. More importantly, mice bearing colorectal CTCs experienced a reduction of tumor cells lodged in the lungs as well as a significantly higher rate of apoptosis (Figure 1.2).

Aside from leukocytes, platelets also routinely interact with CTCs in the bloodstream, making them attractive candidates for therapeutic vehicles. Platelets facilitate the progression of metastasis through CTC–platelet aggregation *(70–72)*. They do so in multiple ways: They protect CTCs by shielding antigen-derived epitopes on tumor cells that are normally recognized by circulating immune cells and increase CTC extravasation potential by inducing an epithelial- to-mesenchymal-like transition *(73–76)*. Multiple studies have introduced platelet-targeting liposomes that contain platelet aggregation

inhibitors to prevent CTC–platelet aggregation *(77–79)*. As an alternative to existing anti-aggregation therapies, several studies have proposed anti-tu moral therapeutics that exploit the natural tendency of CTC–platelet aggregation. For example, Li et al. *(80, 81)* engineered platelets to express TRAIL on their plasma membrane (Figure 1.3). With this technique, hematopoietic stem and progenitor cells were transduced with lentiviral vectors containing the TRAIL gene and a megakaryocyte-specific promoter (Figure 1.4). Sixty days after bone marrow transplantation, bioluminescence images revealed a significant reduction in metastasis in mice with TRAIL-expressing platelets (Figure 1.5). From the standpoint of CTC therapeutics, platelets are increasingly being explored as potential antitumoral vehicles due to their interactions with CTCs *(82)*.

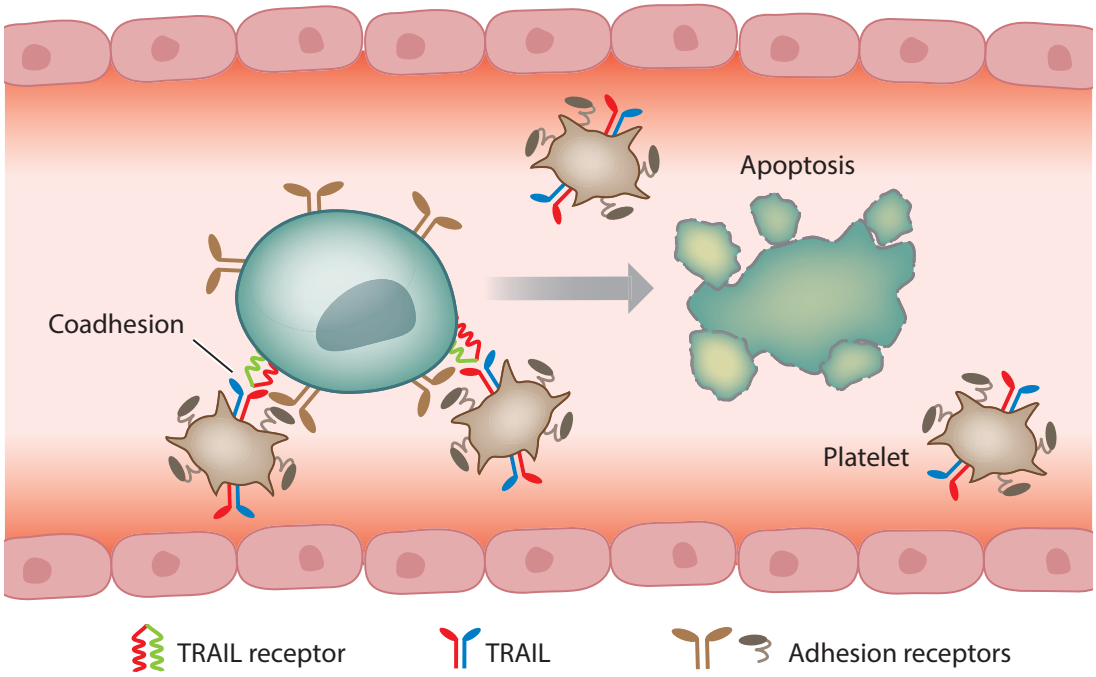

Figure 1.6: Schematic of engineered platelets expressing tumor necrosis factor–related apoptosis-inducing ligand (TRAIL) to kill circulating tumor cells in the circulation. Adapted from E. Lin, T. Cao et al. Annu. Rev. Biomed. Eng. 2018. 20:329–52.

In patients with melanomas, carcinomas, and sarcomas, the first route of metastasis is via the tumor- draining lymph nodes (TDLNs) *(83–85)*. With melanomas in particular, 80% of metastasizing tumor cells travel to the lymph nodes, while the remaining 20% enter the circulation or directly seed *(86)*. Among patients with lung, breast, and colorectal cancers, around 29–37% are diagnosed with metastases in their lymph nodes *(8)*. Therefore, metastatic lymph node prognosis is an important indicator of metastatic burden pre- and posttreatment in many types of cancer therapy *(87–90)*.

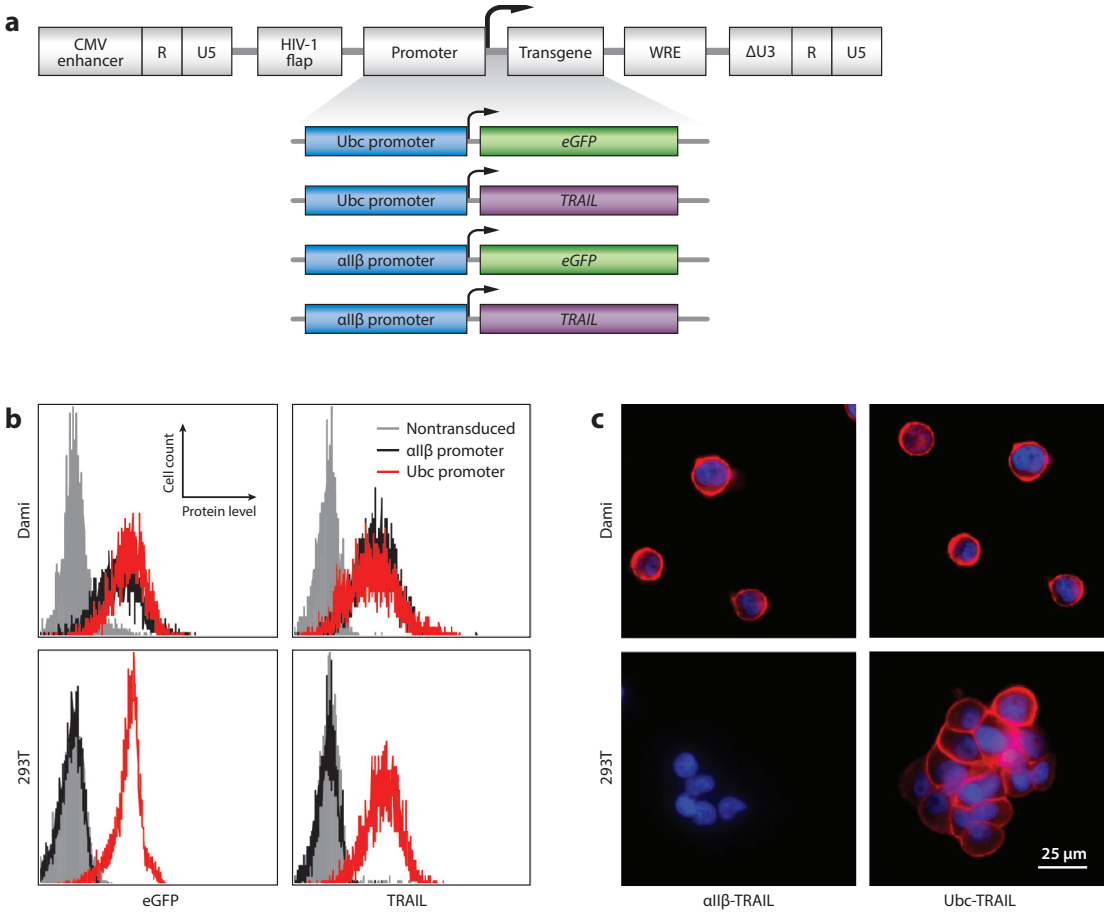

Figure 1.7: Cells transduced with megakaryocyte-specific lentiviral expression vectors express target protein only in a lineage-specific manner. (a) Schematic of lentiviral vectors for expression of enhanced green fluorescent protein (eGFP) and tumor necrosis factor–related apoptosis-inducing ligand (TRAIL) in megakaryocytes. (b) Gene expression after transduction of Ubc-eGFP, αIIβ-eGFP, Ubc-TRAIL, and αIIβ-TRAIL in the promegakaryocytic cell line Dami and the human embryonic kidney cell line 293T. (c) Immunofluorescence images of surface-bound TRAIL in Ubc-TRAIL- and αIIβ-TRAIL-transduced Dami and 293T cells. Nuclei were stained with 4′,6-diamidino-2-phenylindole (DAPI) (blue). Abbreviations: CMV, cytomegalovirus; HIV, human

immunodeficiency virus; WRE, woodchuck hepatitis virus posttranscriptional regulatory element. Adapted from E. Lin, T. Cao et al. Annu. Rev. Biomed. Eng. 2018. 20:329–52.

The lymphatic system is a network of vessels that exist throughout the interstitial space of tissues and organs in the body. The body uses these lymphatic vessels to remove waste, toxins, and other unwanted materials from the organs. More importantly, the vessels transport lymph, a fluid containing immune cells, throughout the body to protect it from unwanted antigens. All of the lymphatic vessels drain into lymph nodes, where innate immune response transitions into adaptive immunity: Antigen presenting cells such as DCs and macrophages travel there to prime naïve T and B cells with the processed antigens *(91)*.

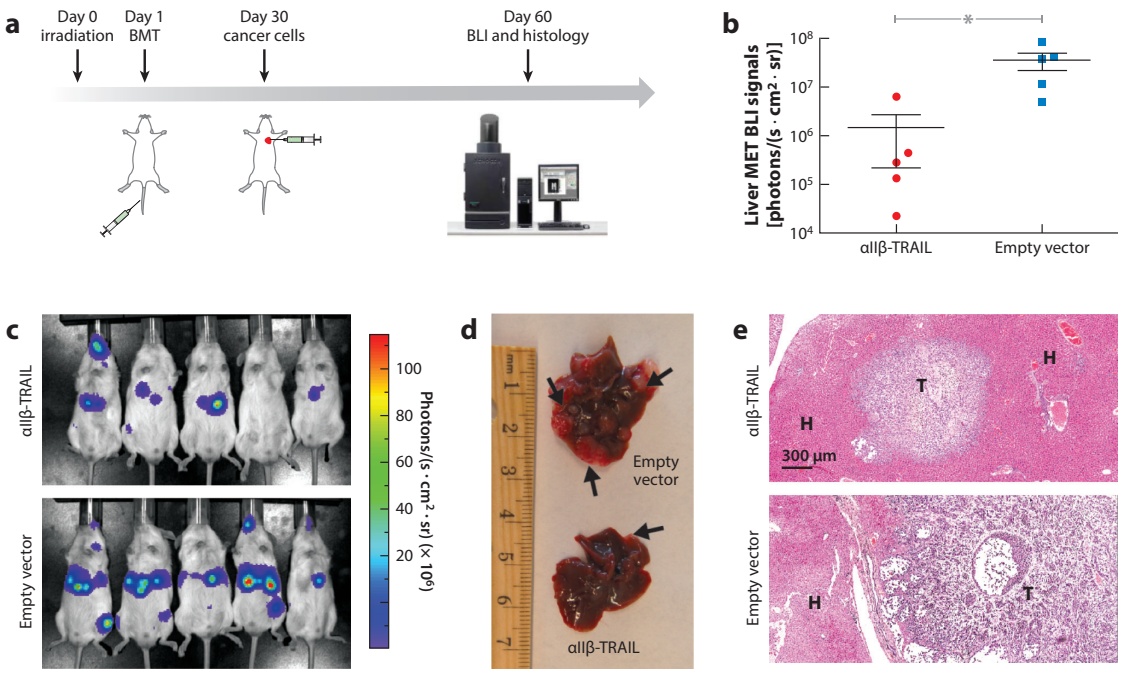

Figure 1.8: Tumor necrosis factor–related apoptosis-inducing ligand (TRAIL)-expressing platelets reduce systemic metastases. (a) Schematic of TRAIL-expressing

*platelet gene therapy in a PCa experimental metastasis model. (b) Liver metastatic burden in mice with TRAIL-expressing platelets (red circles) or empty vector–transduced platelets (blue squares) on day 60 after bone marrow transplantation (BMT). The black lines show means ± SEM (standard error of the mean). The gray asterisk indicates statistical significance: *p < 0.05. (c) Bioluminescence (BLI) images of mice on day 60 after BMT. (d) Liver samples from mice with empty vector–transduced or TRAIL-expressing platelets. (e) Hematoxylin and eosin staining of liver sections. Abbreviations: H, hepatocytes; T, cancer cells. Adapted from E. Lin, T. Cao et al. Annu. Rev. Biomed. Eng. 2018. 20:329–52.*

Tumor cells have several means of escaping the immune response, including the production and release of immunosuppressive factors, impairment of immune cell priming, and recruitment of suppressive immune cells instead of cytotoxic immune cells *(92–94)*. When these cancer- derived immunosuppressive factors drain into the lymph nodes, they can change the lymphatic system from an immune-responsive environment into an immune-repressive one that tolerates tumor metastasis.

Natural killer (NK) cells are innate response immune cells that reside mostly in the paracortex of the lymph nodes. NK cells exert a natural cytotoxic effect against TRAIL-sensitive tumor cells through their constitutive expression of TRAIL on the cell surface and on their cytoplasmic granules, which are released during an immune response *(95–97)*. However, tumor cells possess many mechanisms to evade NK cell–mediated tumor cytotoxicity, including downregulation of their expression of major histocompatibility complex (MHC) class I, shedding of ligands for activation receptors, and secretion of

inhibitory cytokines that can reduce TRAIL expression on NK cells *(39, 98–101)*. To overcome these limitations, researchers have explored enhancing NK cell proliferation and cytokine production with in vivo stimulation using cytokines or ex vivo activation/expansion methods *(102–104)*. However, these studies were met with limited success due to an increase in systemic toxicity, suppression by MHC molecules, and rejection from the host *(105)*. To enhance the intrinsic tumor-suppressing capability of NK cells in the TDLN,

Chandrasekaran et al. *(106, 107)* developed TRAIL-decorated liposomes that specifically bind to NK cells in the tumor-draining inguinal lymph node and effectively prevent the metastatic spread of the primary tumor (Figure 1.6). Liposomes were functionalized with TRAIL and anti-NK1.1 antibody via thiolation; the liposomes then selectively bound to

NK cells (Figure 6). After 6 weeks, NK cells

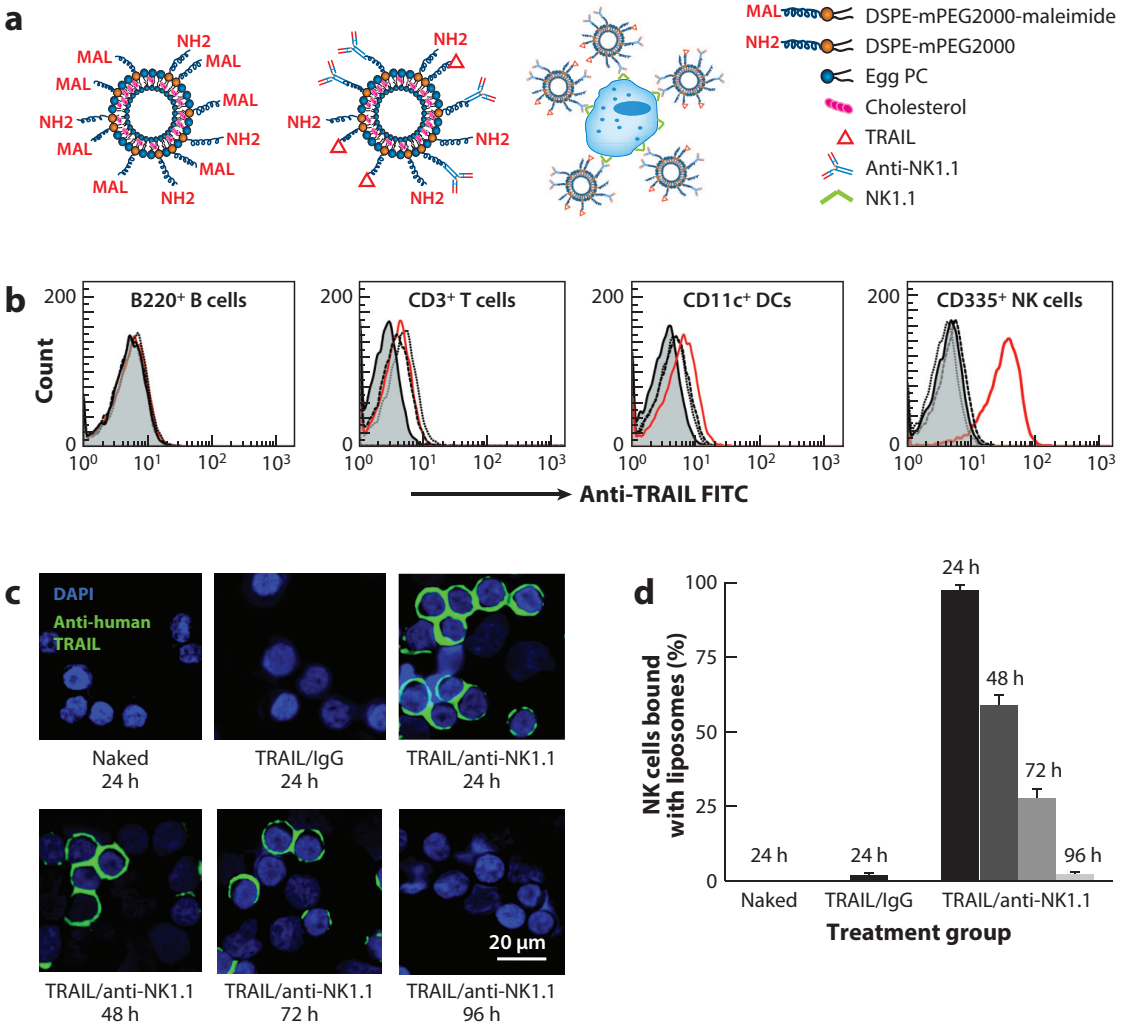

Figure 1.6: Pharmacokinetics of tumor necrosis factor–related apoptosis-inducing ligand (TRAIL)/anti-NK1.1 liposomes. (a) Schematic of liposome formulation. (b) Representative flow cytometry histograms showing TRAIL/anti-NK1.1 liposomes' attachment level to different cell types within the lymph nodes. (c) Confocal fluorescence images of TRAIL/anti-NK1.1 liposomes bound to natural killer (NK) cells isolated from the inguinal lymph. (d) Percentage of NK cells bound with liposomes at different time points. Abbreviations: DC, dendritic cell; DAPI, 4′,6-diamidino-2-phenylindole; DSPE,

1,2-distearoyl-sn-glycero-3- phosphoethanolamine; FITC, fluorescein isothiocyanate; IgG, immunoglobulin G; mPEG, monomethoxypoly(ethylene glycol); PC, phosphatidylcholine. Adapted from E. Lin, T. Cao et al. Annu. Rev. Biomed. Eng. 2018. 20:329–52.

in the tumor-draining inguinal lymph nodes were able to significantly suppress the metastatic burden (Figure 1.7). These results substantiate the antitumoral therapeutic potential of NK cells in the draining lymph nodes and elsewhere. Although NK cells naturally exhibit antitumoral capability, they are susceptible to becoming anergic against tumor cells. Current and future NK cell–based immunotherapy must overcome NK cell paralysis while expanding these cells' existing antitumoral potential.

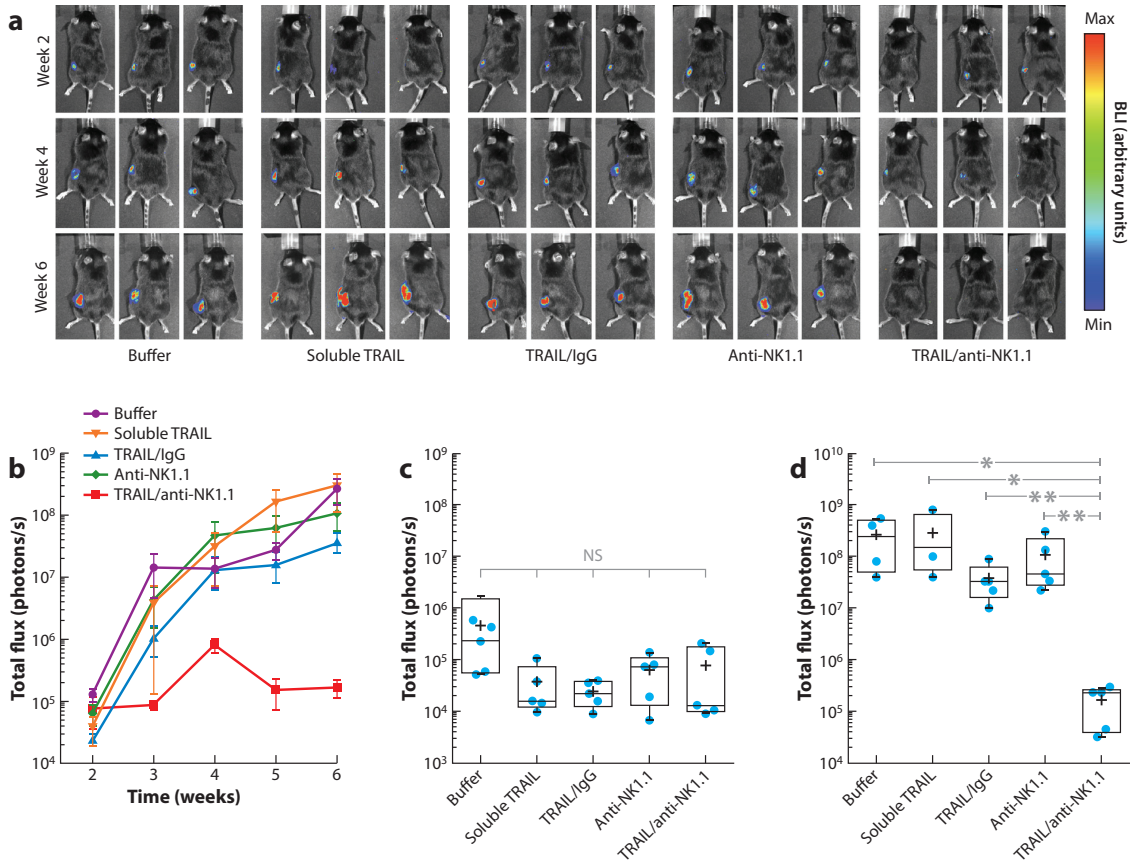

*Figure 1.7: Metastatic burden in the tumor-draining inguinal lymph nodes. (a) Bioluminescence (BLI) images of mice treated with tumor necrosis factor–related apoptosis-inducing ligand (TRAIL)/anti-NK1.1 liposomes showing a reduction of tumor growth in the inguinal lymph node. (b) Total tumor flux in the inguinal lymph nodes with time. (c) Total flux from the inguinal lymph nodes in mice from different treatment groups at week 2. (d) Total flux from the inguinal lymph nodes in mice from different treatment groups at week 6. In panels c and d, bars represent (from top to bottom): maximum, Q3, median, Q1, and minimum. Plus signs represent means. In panel d, gray asterisks represent statistical significance: *p < 0.05, **p < 0.01. Abbreviations: IgG,*

immunoglobulin G; NK, natural killer; NS, nonsignificant. Adapted from E. Lin, T. Cao et al. Annu. Rev. Biomed. Eng. 2018. 20:329–52.

1.4 ANTITUMOR VACCINES

As antigen presenting cells, DCs sample the tissue and tumor microenvironments and phagocytose tumor-derived antigens *(108, 109)*. DCs have the special ability to process the phagocytosed antigens, present them to naïve T cells residing in the lymph nodes, and trigger the proliferation of $CD8^+$ cytotoxic T lymphocytes (CTLs) against the tumor cells in the lymph nodes *(110)*. Several strategies have been proposed that utilize DCs as vehicles to deliver tumor antigens to the lymph nodes with the aim of activating or expanding the patient's immune response against tumor cells. One such strategy is to co-administer tumor lysates in conjunction with the potent DC adjuvants CpG oligodeoxynucleotides so as to elicit an immune response *(111, 112)*. However, the tumor-induced immunosuppressive microenvironment of the TDLNs prevents a sustained and robust CTL response, even in the presence of highly immunogenic antigens *(113, 114)*. Interestingly, the administration of an adjuvant alone, without tumor antigen, is enough to elicit an immune response despite the immunosuppressive state of the TDLNs *(115, 116)*. However, novel therapeutic strategies that prevent and/or reverse the immunosuppressive state of TDLNs may still be warranted to maximize the potential of antitumoral CTL responses.

Synthetic implantable scaffolds that mimic the natural lymph nodes chemically and structurally and can accommodate an immunogenic microenvironment provide great spatiotemporal control and are promising alternative locations for immune cells to cross-

talk, proliferate and disperse *(92)*. Hydrogels made from monomethoxy-PEG-*co*-polylactic-*co*-glycolic acid copolymer hydrogels release granulocyte-macrophage colony-stimulating factor to attract DCs into the matrix *(117)*. Viral vectors containing tumor antigens are then injected locally into the implanted hydrogels to activate the recruited DCs. These cells then travel to the TDLNs to activate the proliferation of CTLs. In a different model, proposed by the Mooney group *(118, 119)*, instead of using viral vectors to introduce tumor-derived antigens to DCs, the antigens and adjuvants are immobilized into the hydrogel matrix. These authors observed sustained DC recruitment into the scaffolds that resulted in a significant and sustained proliferation of antigen-specific CTLs. These results convincingly demonstrate the superior antitumoral therapeutic potential of DC priming using implantable synthetic scaffolds in comparison to treatments without scaffolds.

CHAPTER 2

Supercharged eGFP-Trail Decorated NETs to Ensnare and Kill Disseminated Tumor Cells

2.1 INTRODUCTION

NETosis is an innate immune response elicited by activated neutrophils to fight microbial infections. Activated neutrophils release DNA fibers decorated with anti-microbial proteins called neutrophil extracellular traps (NETs) into the extracellular space to trap and kill surrounding microbes. Here, we show tumor-derived IL-8 released by cancer cells also activates the release of NETs. Until now, there have been no existing technologies that leverage NETs as an anti-tumor drug delivery vehicle. In this study, we describe the re-engineering of neutrophils to express an apoptosis-inducing chimeric protein, supercharged eGFP-TRAIL, on NETs that can ensnare and kill tumor cells while retaining all of their anti-microbial capabilities. We observed significant TRAIL-induced apoptosis in tumor cells captured by TRAIL-decorated NETs. This work demonstrates NETs as a promising technology to deliver protein in response to local cytokine signals.

Neutrophils play a significant role in all stages of tumorigenesis from the initial genotoxic insult, to metastasis to distant organs. Chronic inflammation drives neutrophils to release mutagenetic agents including reactive oxygen species (ROS) and hypochlorous acid (HOCl) that induce DNA damage and mutagenicity on surrounding cells *(120–122)*. Neutrophils make up a significant percentage of white blood cells that infiltrate the tumor microenvironment *(123)*. In that setting, infiltrating neutrophils continue to promote

tumor development by secreting pro-inflammatory and pro-angiogenesis chemokines and cytokines such as matrix metallopeptidase 9 (MMP9) and interleukin 6 (IL-6) *(124–126)*. Tumor metastasis through hematogenous dissemination involves circulating tumor cells (CTCs) shedding from the primary tumor site and reaching distant organs via the circulatory system. In a recent study, neutrophils have been found to support CTC survival during hematogenous dissemination *(127)*. Furthermore, neutrophils have been identified as the main driver in establishing the pre-metastatic microenvironment in several mouse breast cancer models *(128)*.

NETosis is a unique form of innate immune response elicited primarily by neutrophils to combat microbial infections *(129)*. In the presence of antigens, neutrophils undergo NETosis by following a program of cell death and releasing condensed DNA fibers decorated with cationic antimicrobial proteins, collectively called NETs, into the extracellular space *(130)*. Tumor cells release tumor-derived interleukin 8 (IL-8), a potent neutrophil chemoattractant, to increase tumor growth and metastatic potential by: (a) promoting tumor neovascularization and (b) inducing infiltrating neutrophils to release pro-metastatic enzymes*(131)*. Initially, NETosis was found to specifically occur in the presence of bacterial antigens, but here we show that tumor-derived IL-8 released by tumor cells also elicits NETosis in neutrophils (Figure 2.1b, c). Blocking the tumor-derived IL-8 pathway with a small molecule, reparixin, returned NETosis back to basal level (Figure 2.1e). Moreover, we quantified cell-free serum DNA levels in cancer patients and found a significant increase in serum DNA level compared to the healthy cohort suggesting that NETs may also have an elevated presence in the circulatory system in cancer patients (Figure 2.1a). These results support previous findings that malignant

and non-malignant neutrophils in tumor-bearing mice have increased sensitivity toward undergoing NETosis *(132)*. Given data shown here of the ubiquitous presence of neutrophils in all stages of tumor development, we proposed a unique anti-tumor drug delivery system by exploiting the ability of neutrophils to spontaneously undergo NETosis in the presence of cancer cells.

Although NETs have been shown to ensnare cancer cells, they lack the ability to kill cancer cells. More insidiously, trapped tumor cells show increased metastatic potential *(133)*. In the current study, we proposed to re-engineer human neutrophils to express NETs decorated with an apoptosis-inducing peptide, TRAIL, that could selectively destroy cancer cells during NETosis. TRAIL is a small cytokine expressed by most cell types that selectively induces apoptosis in tumor cells overexpressing death receptors while sparing healthy cells *(68, 80)*. In this model, we successfully knocked in our gene of interest (GOI), expressing the chimeric protein eGFP-TRAIL, into the safe harbor site AAVS1 on chromosome 19 of the proto-neutrophilic cell line PLB-985 using the CRISPR/Cas system (Figure 2a,b). PLB-985 is a leukemic cell line that can be induced into neutrophil-like cells capable of undergoing NETosis *(134, 135)*. Aside from serving as a fluorescent marker, eGFP serves a more important function by selectively allowing the chimeric protein to electrostatically bind to the DNA fibers of NETs during NETosis (Figure 2a). By modifying the surface charge of eGFP to become increasingly more positive, we were able to increase its avidity to the negatively-charged DNA fibers in a charge-dependent manner (Supp. Figure 2.1). The transfected cells stably expressed eGFP-TRAIL-decorated NETs during NETosis (Figure 2.2e-f). mRNA data showed successful expression of the transgene (Figure 2.2c-d). Immunostaining scanning electron

microscopy with TRAIL antibody-conjugated gold nanoparticles of NET DNA fibers revealed that eGFP-TRAIL protein molecules are decorated along the DNA fibers (Figure 2.2f).

PLB-985 derived neutrophils expressing NETs decorated with eGFP-TRAIL co-cultured with multiple human tumor cell lines showed significant apoptosis-inducing potential. In COLO-205, after 16 h of co-culture, 7% and 12% of the tumor cells underwent early and late apoptosis, respectively, while over 55% of the population were classified as necrotic (Figure 2.3a). In the presence of eGFP-decorated NETs we observed an over 60% kill rate of cancer cells in the three cell lines SW620, COLO 205 and MDA-MB-213 (Figure 2.3b). SEM images clearly showed significant NETosis when neutrophils were co-cultured with tumor cells. However, only when NETs were decorated with eGFP-TRAIL did the tumor cells undergo apoptosis as evident by membrane blebbing (Figure 2.3c).

The constant presence of neutrophils near tumor cells in all stages of cancer development and in conjunction with the unique ability of neutrophils to undergo NETosis in the presence of cancer cells, make neutrophils a promising candidate for the delivery of cancer therapeutics. Here we introduced a novel form of cancer therapy by leveraging these unique aspects of neutrophils by re-engineering the cell to express a chimeric eGFP-TRAIL protein. This form of treatment exemplifies the potential of employing neutrophils as a drug delivery vehicle that, until now, has been largely unexplored.

2.2 METHODS

Cell culture and differentiation

The acute myeloid leukemia PLB-985 cell line (derivative of HL-60) stably expressing Cas9 protein was a generous gift from the Collins Lab (University of California, Davis). The cells were cultured in RPMI 1640 media supplemented with 2 mM L-glutamine, 25 mM HEPES, 10% (v/v) FBS, and 2 □g/mL Blastincidin at 37C and 5% CO_2. Cultured cells were regularly tested for mycoplasma using the Universal Mycoplasma Detection Kit (ATCC 30-1012K).

Neutrophil differentiation of logarithmically growing PLB-985 cells was induced by reduction of FBS to 5% and supplementation of 0.5% (vol/vol) DMF. After 3 days, an equivalent of the initial volume of differentiating medium was added and the differentiation continued until day 7.

Plasma cell free DNA isolation and quantification

Plasma was isolated from whole blood of cancer patients and healthy donors by centrifugation. To 1 mL of plasma, 100 □l of Tris-HCl (pH 8.0) buffer containing 250 mM EDTA, 750 mM NaCl, 100 g/L of sodium dodecyl sulfate and 20 mg/mL of proteinase K was added and incubated for 2 h at 56°C. Next proteins were precipitated with 200 □l of 6M NaCl solution. The cell-free DNA (cfDNA) was extracted from the supernatant using phenol-chloroform-isoamyl alcohol (25:24:1) followed by ethanol precipitation. DNA concentration was quantified using nano-drop.

Vector design

pAAVS1-eGFP-TRAIL was constructed starting with the plasmid template of pMK232 (Addgene 72834) containing the AAVS1 homology arms. The eGFP-TRAIL sequence was inserted downstream of the CMV promoter. pX330-U6-AAVS1 was constructed using the plasmid template of pX330 (Addgene 42230). The sgRNA oligonucleotides targeting the AAVS1 region were inserted into the plasmid downstream of the U6 promoter using restriction sites AgeI and EcorI.

Supercharged eGFP-Trail DNA sequences were constructed by using site-directed mutagenesis (Agilent) PCR. Indicated amino acids of the wildtype eGFP sequence were replace with neutral or positively charged amino acids. Protein surface charge was calculated by summing up the total charge of the eGFP sequence based on the predicted charge of the amino acids in the sequence. All plasmid constructs were verified by sequencing.

CRISPR/CAS9 Knock-In of eGFP-TRAIL

$2x10^6$ PLB-985 cells were nucleofected (AMAXA Cell Nucleofector Kit V and Amaxa Nucleofactor II, program C-023) With 20 □g of pAAVS1-eGFP-TRAIL and 20 □g of pX330-U6-AAVS1. Immediately after nucleofection 500 □l of medium was added to the cuvette and the cells incubated at room temperature for 10 min. Then the cells were cultured for 48 h. After 48 h, GFP-expressing cells were selected with culture medium supplemented with 2 □g/mL Puromycin.

Chemical and Antibodies

TACS® Annexin V Kit (Gaithersburg, MD, USA) was used for assaying cell apoptosis. Reagents for SEM were obtained from Electron Microscopy Sciences (Hatfield, PA,

USA): glutaraldehyde, osmium tetroxide and uranyl acetate. Antibodies for human TRAIL were purchased from Biolegend (San Diego, CA, USA). Primary antibodies for human TRAIL and β-actin were obtained from PeproTech (Rocky Hill, NJ, USA) and Santa Cruz Biotech (Santa Cruz, CA, USA). HRP-conjugated anti-mouse and anti-rabbit antibodies were obtained from Santa Cruz Biotech. IL-8 human Elisa Kits were purchased from ThermoFisher.

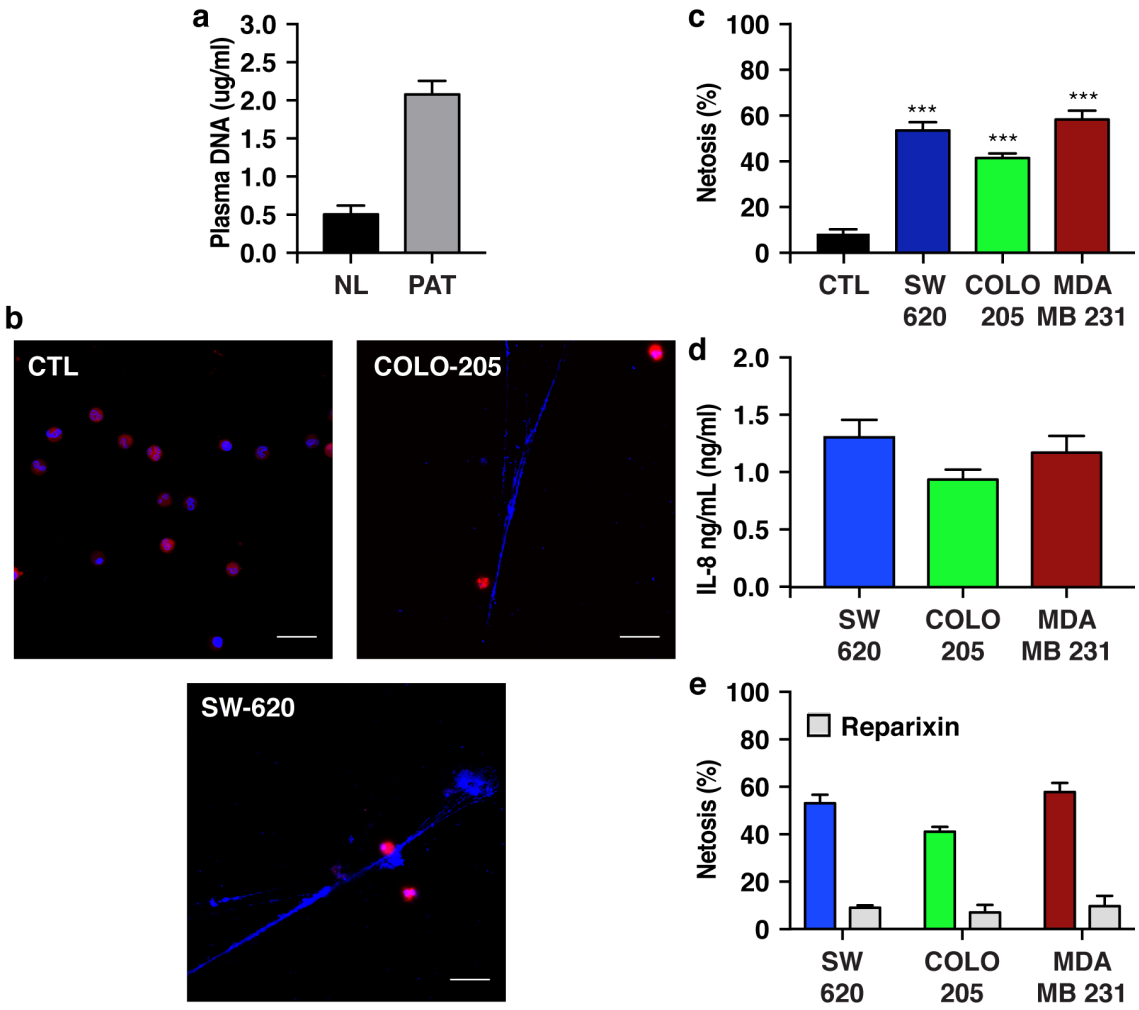

Figure 2.1: Neutrophils undergo spontaneous NETosis in the presence of tumor cells. (a) cfDNA plasma DNA level of normal donors (ND) and cancer patients (PAT). (b) Confocal images of neutrophils underwent NETosis in conditioned media. (CTL) – control group, COLO-205 and SW-620 are condition media collected after 48 h from these indicated cell lines. (c) NETosis level of neutrophils after culturing in conditioned media for 24 h. (d-e) Extracellular tumor-derived IL-8 levels in conditioned media. Reparixin concentration (20 □g/mL).

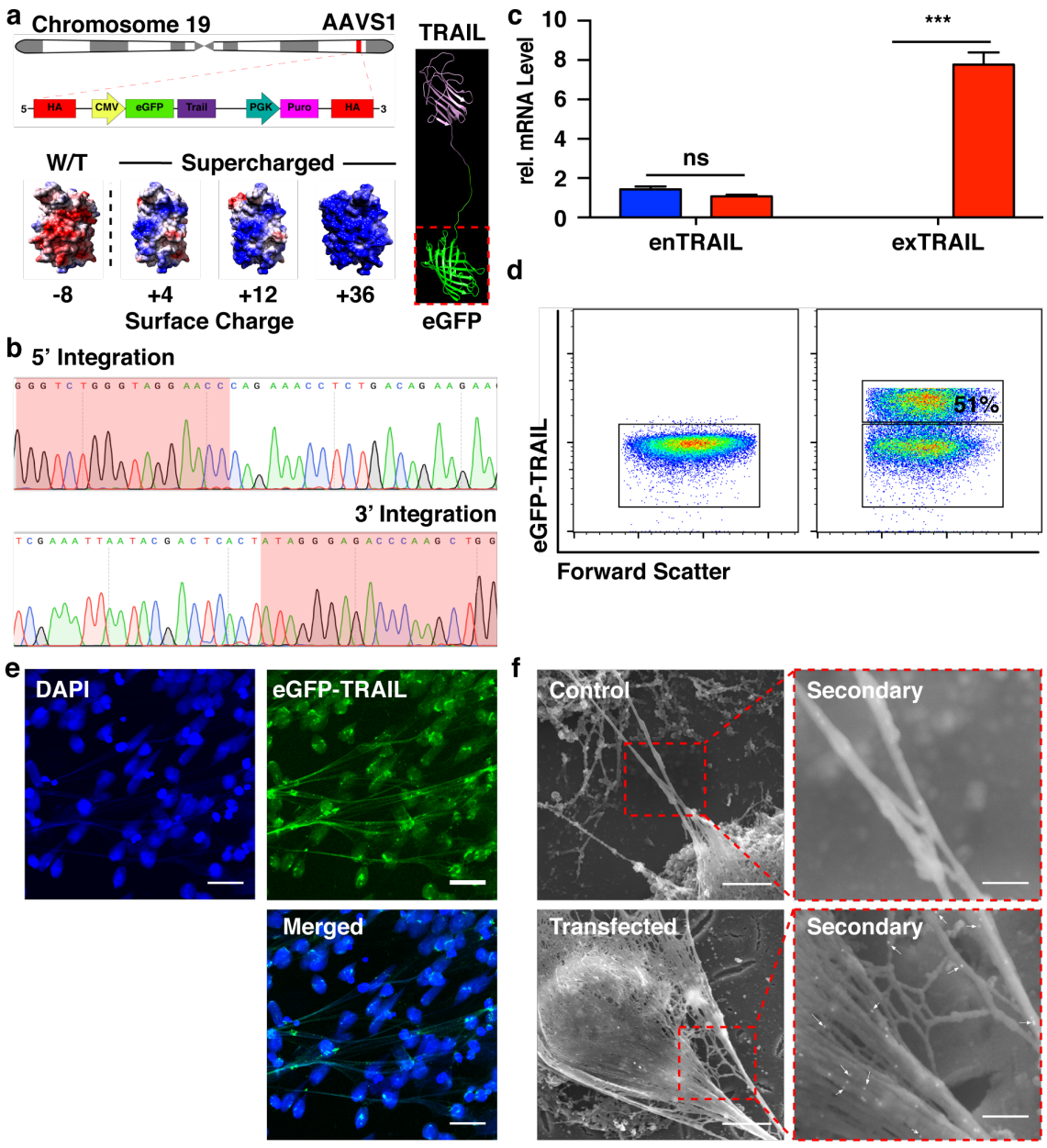

Figure 2.2: Engineered neutrophils express supercharged eGFP-TRAIL on NETs during NETosis (a) Schematic of the insertion site, AAVS1, on chromosome 19. Cartoon representation of eGFP-TRAIL chimeric protein. Surface charge of eGFP ranging from -4 to +36 (Red - negative charge, Blue - positive charge. (b) DNA sequencing result of genomic DNA isolated from cells positive for eGFP-TRAIL. (c) relative mRNA level of endogenous (enTRAIL) and exogenous (exTRAIL) TRAIL levels. (d) Flow cytometry of

cells expressing eGFP-TRAIL 24 h after nucleofection. (e) Confocal images of NETs decorated with eGFP-TRAIL (Blue – DAPI stain, Green – eGFP-TRAIL. (f) Immuno-gold SEM images of neutrophils expressing eGFP-decorated NETs (White arrows – eGFP-TRAIL).

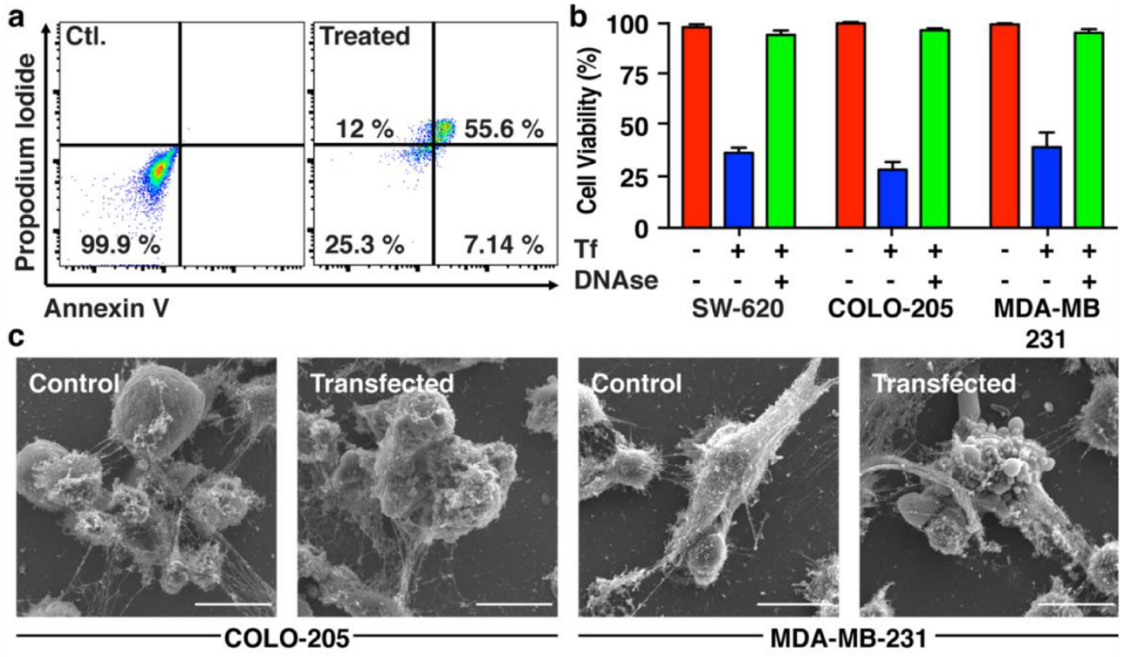

Figure 2.3: Supercharged eGFP-TRAIL expressing neutrophils trap and destroy tumor cells during NETosis (a) Representative flow cytometry result of COLO-205 cells co-cultured with eGFP-TRAIL expressing neutrophils for 24 h and stained for apoptosis and necrosis using Annexin V and Propodium Iodide, respectively. (b) Cell viability quantification of indicated cancer cell lines co-cultured with wildtype neutrophils or cells positive for eGFP-TRAIL (Tf). (c) Immuno-gold SEM images of indicated cancer cells co-cultured with neutrophils.

CHAPTER 3

Effect of Extracellular pH on Selectin Adhesion: Theory and Experiment

This chapter were published in *the Biophysical Journal (136).*

3.1 ABSTRACT

Selectins mediate circulatory leukocyte trafficking to sites of inflammation and trauma, and the extracellular microenvironments at these sites often become acidic. In this study, we investigated the influence of slightly acidic pH on the binding dynamics of selectins (P-, L-, and E-selectin) to P-selectin glycoprotein ligand-1 (PSGL-1) via computational modeling (molecular dynamics) and experimental rolling assays under shear in vitro. The P-selectin/PSGL-1 binding is strengthened at acidic pH, as evidenced by the formation of a new hydrogen bond (seen computationally) and the observed decrease in the rolling velocities of model cells. In the case of L-selectin/PSGL-1 binding dynamics, the binding strength and frequency increase at acidic pH, as indicated by the greater cell-rolling flux of neutrophils and slower rolling velocities of L-selectin-coated microspheres, respectively. The cell flux is most likely due to an increased population of L-selectin in the high-affinity conformation as pH decreases, whereas the velocities are due to increased L-selectin/PSGL-1 contacts. In contrast to P- and L-selectin, the E-selectin/PSGL-1 binding does not exhibit significant changes at acidic pH levels, as shown both experimentally and computationally.

3.2 INTRODUCTION

The localization of circulating leukocytes to sites of injury or inflammation is a multistep adhesion cascade *(137, 138)* involving a), the initial tethering and rolling of leukocytes along the vasculature wall; b), integrin-mediated firm adhesion; and c), the extravasation of cells into tissues *(139)*. Selectins (P-, L-, and E-selectin) are membrane adhesion molecules that facilitate the initial tethering and rolling of leukocytes. Although selectin-mediated cell rolling is ubiquitously observed for leukocytes, accumulating evidence suggests that circulating tumor cells (CTCs) also exhibit selectin-mediated rolling *(140, 141)*.

Selectins are differentially expressed on many cell types. P-selectin is stored in the a-granules of platelets and the Weibel-Palade bodies of endothelial cells, and upon activation of the endothelial cells is rapidly transported to the surface *(142, 143)*. E-selectin expression is limited to the endothelial lining *(144)*, and in addition to mediating leukocyte rolling during inflammation, it has also been shown to assist human CD34þ hematopoietic cell homing to the bone marrow *(145)*. Whereas P- and E-selectin are endothelial selectins, L-selectin is expressed on most circulating leukocytes, with the exception of several subpopulations of memory cells *(146)*. The presenting architectures of selectins are highly conserved. Their structures consist of a C-type lectin domain at the N-terminus, an epidermal growth factor (EGF)-like module, two to nine short consensus repeats, a transmembrane region, and a cytoplasmic tail *(147)*. Selectin ligands consist of a structurally diverse array of surface glycoproteins (e.g., GlyCAM-1, CLA, HCELL, and PSGL-1) *(148–150)*. These ligands require post-translational N- and/or O-linked

glycosylation of their backbone with a tetrasaccharide carbohydrate called sialyl Lewis X (sLe^X) to gain selectin-binding activity. sLe^X and its derivative sLe^A are the most basic binding determinants for all three selectins. In this study, we focus on selectin/PSGL-1 binding because PSGL-1, a glycoprotein heavily decorated with sLe^X, is a common vascular selectin ligand that can readily bind to all three selectins.

The physiologic pH level in extracellular microenvironments can significantly decrease due to various pathological and physiological phenomena. For example, anaerobic lactate buildup and inadequate extraction of metabolites during prolonged ischemia can decrease the extracellular pH level, a condition known as acidosis *(151, 152)*. Studies have shown that acidosis occurs in the early stages of wound healing *(153, 154)*, which also involves periods of elevated leukocyte and platelet recruitment. Serrano et al. *(155)* showed that under acidic conditions, neutrophil adhesion to the vascular endothelium is enhanced. Acidic conditions also promote angiogenesis of injured tissues *(156)*. Further- more, tumor microenvironments are often acidic, with pH levels as low as 6.2 *(157, 158)*. In addition, because the recruitment of leukocytes to targeted tissues is selectin mediated, these observations suggest that acidic pH might alter selectin/ligand-binding mechanics, resulting in a change in cell binding dynamics compared with the homeostasis pH level of 7.4.

In this study, we investigated the influence of acidic extra- cellular pH on P-, L-, and E-selectin interactions with PSGL-1 and sLe^x. We used molecular dynamics (MD) and steered MD (SMD) to predict changes in adhesion characteristics while performing cell-

rolling assays with selectin- coated capillary tubing to characterize the effects of pH on cell rolling and adhesion in vitro.

3.3 MATERIALS AND METHODS

MD

The lectin and EGF crystal structures of P-selectin bound to PSGL-1 (1G1S *(159)*), E-selectin (1G1T *(159)*), and L-selectin (3CFW) were obtained from the Protein Data Bank for use as starting atomic coordinates. Free-dynamics and SMD simulations were performed using the YASARA (http://yasara.org) package of MD programs with the YAMBER3 self-parameterizing force field *(160)*, and therefore no external force field parameters were specified. For all types of simulations, the temperature and pressure were held constant at 300 K and 1 atm, respectively. Periodic boundary conditions, the particle mesh Ewald method for electrostatic interactions *(161)*, and the recommended 7.86 A° force cutoff for long-range interactions were also used.

For equilibration simulations, each selectin was individually solvated in a water box and neutralized by adding Ca^{2p} and Cl ions to a concentration of ~50 mM calcium. To allow for free protein rotation, the water boxes were defined as cubes with lengths measuring ~10 A° away from the two farthest atoms in each complex. The P-selectin (subunit A), E-selectin, and L-selectin water cube lengths were ~100 A°, 80 A°, and 80 A°, respectively. The water boxes were allowed to adjust slightly to constrain the water density to 0.997 g/L. The conformational stresses were then removed via short steepest-descent minimizations followed by simulated annealing until sufficient convergences were

reached. To simulate the effect of pH, changes in pKa values for the amino acids were computed by the fast empirical pKa prediction method as implemented by YASARA *(162)*. At the physiologically neutral pH condition, amino acids with pKa values R 7.4 were protonated, and at physiologically relevant acidic pH conditions, amino acids with pKa values R 6.2 were protonated. Free-dynamics simulations were then run for each selectin in both neutral and acidic conditions for 10 ns time periods.

Predicted structures of PSGL-1 bound to L- and E-selectin were obtained by aligning the L-selectin (3CFW) and E-selectin (1G1T) crystal structures on the P-selectin/PSGL-1 complex (1G1S, subunit a) via the MUSTANG algorithm *(163)*. This approach is similar to that used in previous studies of L-selectin/PSGL-1 binding dynamics *(164, 165)*. After the structures were overlaid, free-dynamics simulations were run for the L-selectin/PSGL-1 and E-selectin/PSGL-1 complexes at physiologically neutral pH conditions and the above MD parameters for 10 ns time periods. The equilibrated complex structures were then run for another 10 ns after the protonation of relevant amino acids in neutral and acidic conditions.

Following previous SMD studies on the P-selectin/PSGL-1 complex *(166)*, the Gly-147 residue was held frozen as the Ca atom of the Pro-18 residue was pulled through a spring with a spring constant of 70 pN/A$^{\circ}$ and a speed of 5 A$^{\circ}$/ns. To reduce the computational cost of these simulations, the simulation cells were changed to a water box of 140 50 60 A$^{\circ 3}$ and were also neutralized by adding $CaCl^2$ to a concentration of ~50 mM Ca. To further prevent the EGF domain from unfolding during SMD simulations with the YAMBER3 force field, the Gln-130 residue was also held frozen. SMD simulations were

run until the PSGL-1 completely dissociated from the P-selectin binding site. The same conditions were also used for L-selectin/PSGL-1 SMD simulations, except that the Gly-129 residue of the EGF domain was held frozen instead of residue 130. All SMD simulations were run in triplicate to verify the dissociation times.

Reagents and antibodies

RPMI 1640 cell culture media, fetal bovine serum (FBS), penicillin-streptomycin, phosphate-buffered saline (PBS), and Hank's balanced salt solution (HBSS) were purchased from Invitrogen (Grand Island, NY). Recombinant human P-, L-, and E-selectin/IgG chimera were purchased from R&D Systems (Minneapolis, MN).

Cell lines and cell culture

The acute myeloid leukemic KG1a cell line (ATCC number CCL-264.1) was purchased from ATCC (Manassas, VA) and cultured in RPMI 1640 media supplemented with 2 mM L-glutamine, 25 mM HEPES, 10% (v/v) FBS, and 100 U/mL penicillin-streptomycin at 37C and 5% CO_2.

Neutrophil isolation

Human peripheral blood was collected from healthy adult donors after they provided informed consent. Neutrophils were isolated using 1-Step Polymorphs (Accurate Chemical and Scientific; Westbury, NY) according to a previously described protocol *(167)*. Isolated neutrophils were resus- pended at a concentration of 10^6 cells/mL in HBSS buffer supplemented with 0.5% (wt/vol) human serum albumin, 10 mmol/L

HEPES, and 2 mmol/L $CaCl^2$. In specified experiments, 35 mmol of TAPI-0 was added to mitigate mechanical shedding of L-selectin *(168)*. Experiments involving neutrophils were completed within 6 h after the neutrophils were extracted from the donor.

Microtube functionalization

Micro-Renathane (MRE) tubes (300 mm i.d. and 50 cm long; Braintree Scientific, Braintree, MA) were sterilized with 75% ethanol for 15 min. After three washes with PBS (Ca^{++} and Mn^{++} free), the microtubes were incubated with Protein G (2 mg/ml PBS) for 1 h. Next, the inner luminal surface was functionalized with recombinant human P-selectin, E-selectin, or PSGL-1 at specified concentrations for 2 h. The microtubes were then incubated with dry milk powder (5% w/v) in PBS for 1 h to prevent nonspecific adhesion *(169)*. For control experiments, microtubes were prepared as indicated above except that the adhesion molecule was replaced with BSA.

Microsphere functionalization

SuperAvidin-coated microspheres (CP01N/10216) and Protein-A-coated microspheres (CP02N/10279) were purchased from Bangs Laboratories (Fishers, IN). Microspheres were washed three times with PBS buffer. Next, the microspheres were incubated with adhesion proteins at specified concentrations for 1 h with gentle mixing every 15 min. Finally, the micro- spheres were washed twice and resuspended in buffer (1×10^6 micro-spheres/ml) at varying pH levels.

Microtube flow experiment

Cells or microspheres suspended in flow buffer (PBS supplemented with 2 mmol Ca^{bb}) at varying pH were perfused through the microtubes using a syringe pump at specified wall shear stresses. Videos were recorded for 1 min at random locations along the length of the microtube after 5 min of perfusion.

Data acquisition

Videos of the rolling cells were captured using a microscope-linked Hitachi CCD camera KP-M1AN (Hitachi, Japan) and a Sony DVD Recorder DVO- 1000MD (San Diego, CA). Rolling velocity was determined using ImageJ (U.S. National Institutes of Health, Bethesda, MD). Rolling cells were defined as any cell translating along the tube surface for >2 s at a velocity < 50% of the free stream velocity of a noninteracting cell near the tube wall. Rolling flux was determined by counting the number of cells that entered the field of view over a period of 1 min.

Statistical analysis

Rolling velocity and rolling flux were plotted and analyzed using Prism (GraphPad Software, San Diego, CA). Two-tailed unpaired t-tests were used to analyze results.

3.4 RESULTS AND DISCUSSION

P-selectin/PSGL-1 adhesion at acidic pH—SMD analysis

Figure 3.1 depicts the equilibrated P-selectin/PSGL-1 complex structures at physiologically neutral pH (A) and acidic pH (B), and the histidine pKa values for P-selectin bound (pKa*) and unbound (pKa) from PSGL-1 are shown in Table 3.1. When

P-selectin was not bound to PSGL-1, the pre- dicted histidine pKa values were <5.8, suggesting that no significant change in histidine protonation states or protein conformation occurs in slightly acidic pH environments. On the other hand, when P-selectin was bound to PSGL-1, the predicted H114 pKa value increased from 5.0 to 7.1, thus allowing H114 to be protonated in slightly acidic environments. As a result, a hydrogen bond between H114 and Y7 (on PSGL-1) was formed after H114 protonation, which would suggest an increase in binding energy and possibly longer interaction lifetimes.

To examine the effect of H114 protonation on the binding lifetime of the P-selectin/PSGL-1 complex, we used SMD to manually dissociate PSGL-1 from P-selectin. Representative SMD force versus time graphs are shown in Figure 3.2 to illustrate variations between neutral and acidic environments. Interestingly, there was a remarkable difference in the dissociation dynamics depending on the protonation state of H114. At the start of the simulation (Figure 3.1), the P-selectin/PSGL-1 complex conformations were nearly identical where clear H114/Y7 and R85/Y10 contacts were present, as suggested by Somers et al. *(159)*. However, after 6 ns in neutral conditions, R85 had already dissociated from Y10 to form a hydrogen bond to sLe^X (Figure 3.2b), whereas in acidic conditions the R85/Y10 contact was preserved (Figure 3.2d), most likely due to the increased inter-action energy from the hydrogen-bonded H114/Y7 contact. Moreover, Y5 was hydrogen-bonded to both K8 and the P-selectin backbone, resulting in a total of four contacts in acidic conditions, compared with two contacts in neutral conditions. As PSGL-1 was pulled away from P-selectin in neutral conditions, the Y5 and Y7 amino acids underwent several sliding-rebinding events involving K8, K112, and the P-selectin

backbone, resulting in a force plateau from 8.5 to 10.5 ns. Subsequent to the numerous sliding-rebinding events, Y5 was pulled too far to contact P-selectin significantly (Figure 3.2c). In contrast, at ~9 ns in acidic conditions, there was a rupture of all contacts (except for coordination bonding), signified by a dramatic decrease in the pulling force. The R85 and Y7 contacts were then bonded to sLe^X and H114, respectively, while Y5 was kept within the binding range of K8 and K112 (Figure 3.2e). On average, the protonation of H114 increased the binding lifetime by >1 ns, and therefore cells expressing PSGL-1 were predicted to roll more slowly at slightly acidic pH than at physiologically neutral pH on P-selectin surfaces.

P-selectin/PSGL-1 adhesion at acidic pH—experimental rolling analysis

To further substantiate our SMD results, we investigated P-selectin/PSGL-1 complex binding dynamics in acidic environments in vitro by perfusing KG1a cell suspensions through P-selectin-coated microtubes at varying pH levels (6.2–7.4) with a flow rate of 0.111 ml/min, an equivalent shear stress of 7 dyn/cm^2 (Figure 3.3a). Cell rolling was confirmed to be specifically mediated by P-selectin/ PSGL-1 binding, because all interactions were abrogated when cells were perfused in $Ca^{2þ}$-free buffer containing 5 mM of EDTA (data not shown). As the buffer pH level decreased from 7.4 to 6.8, KG1a cells rolled more slowly, with the average rolling velocity reaching a minimum of 4.25 5 0.21 mm/s at pH 6.8, suggesting longer P-selectin/PSGL-1 interaction lifetimes at slightly acidic pH levels. Conversely, pH levels below 6.8 decreased the binding interaction life- time of P-selectin to PSGL-1, which was manifested by an increase in rolling velocity. Rolling-assay experiments were also performed with PSGL-1 coated microspheres as shown in

Figure 3.3b. The microspheres exhibited rolling characteristics similar to those of KG1a cells: the average rolling velocity decreased at slightly acidic pH, with a minimum at pH 6.6, and increased from the minimum at pH levels below 6.6. This increase in rolling velocity may be a consequence of the on-rate kinetics. Microspheres that were functionalized with carbohydrate sLe^X (effectively eliminating the putative PSGL-1 backbone responsible for hydrogen binding) did not exhibit enhanced binding lifetime in slightly acidic environments (Figure 3.3 C).

Circulating myeloid cells express PSGL-1 on their surfaces, which serve as a counterreceptor for P-selectin *(170)*. As previously mentioned, P-selectin/ligand binding facilitates the tethering and eventual rolling of myeloid cells on the activated endothelial lining during physiological events such as injury to the vessel wall and inflammation. These phenomena are often coupled with a decrease in pH level in the microenvironment where adhesion occurs *(171)*. The results of both the computational and experimental studies presented here suggest that in slightly acidic environments, the binding of the P-selectin/PSGL-1 com- plex is enhanced due to the formation of a hydrogen bond between the protonated H114 (P-selectin) and Y7 (PSGL-1) residues. Our findings suggest that during inflammation, a drop in pH may have a contributory effect on recruiting circulating myeloid cells by increasing the binding strength and lifetime between P-selectin to PSGL-1, which slows cell rolling velocities at and around the target site.

L-selectin/PSGL-1 adhesion at acidic pH—MD analysis

Given the good agreement between theory and experiment for P-selectin, a similar computational analysis was per- formed for L-selectin, as shown in Figures 3.4 and 3.5.

L-selectin contains three histidine residues that potentially can be protonated. The H4 and H130 residues had predicted pKa values of 6.9 and 6.8 (Table 3.2), respectively, when not bound to PSGL-1, and therefore likely change protonation states in slightly acidic conditions. The main effect of protonating these two residues in acidic conditions was the dissociation of the hydrogen bond between the N138 residue (of the EGF domain) and the lectin domain. This hydrogen bond is important, because Phan et al. *(172)* found that a single point mutation of N138 to glycine increased cell flux, decreased cell rolling velocities, and increased the duration of cell-tethering events. They suggested that these changes were due to a greater L-selectin population in the extended (high-affinity) conformation.

The predicted L-selectin/PSGL-1 complex showed an increase of the H110 pKa value from 4.6 (unbound) to 6.5 (bound) and was also expected to be protonated in slightly acidic conditions. The protonation of H110 dramatically changed the PSGL-1 conformation, yielding a stacking interaction between H110 and L13, and increased the likelihood of hydrogen bonding between Y7 and the L-selectin backbone (Figure 3.5). SMD simulations demonstrated that the protonation of H110 increased the L-selectin/PSGL-1 binding lifetime by >1.5 ns, as shown by the representative SMD force versus time graphs in Figure 3.5. A similar result was discovered via the mutation of A108 of L-selectin (an amino acid neighboring H110) to histidine, where the mutation was proposed to increase the stacking interactions of L-se- lectin and PSGL-1, resulting in an increased binding interaction *(164)*. Therefore, an acidic pH environment should produce considerable changes in the rolling profiles of cells expressing L-selectin when

perfused over PSGL-1-coated surfaces via a change in selectin conformation and an increased selectin/PSGL-1 binding interaction.

L-selectin/PSGL-1 adhesion at acidic pH— experimental rolling analysis

Rolling-assay experiments with isolated human neutrophils perfused through PSGL-1-coated microtubes showed that the neutrophils maintained a statistically constant rolling profile at pH levels ranging from 7.4 down to 6.6, but steadily increased as the pH level became more acidic than 6.6 (Figure 3.6a). Interestingly, pH had an effect on the number of neutrophils that adhered and rolled on the PSGL-1-coated surface, causing the cell flux to increase in more acidic conditions over a range of shear stresses (Figure 3.6 c). This suggests that slightly acidic pH may increase the binding frequency of L-selectin to PSGL-1, as manifested by a higher rolling flux at lower pH. Rolling-assay experiments using L-selectin-coated micro- spheres perfused over PSGL-1-coated surfaces were also conducted (Figure 3.6b). Interestingly, the microspheres rolled more slowly at pH 7.2 than at 7.4 and remained at this depressed velocity at pH levels as low as 6.4 before they began to increase to higher velocities at pH levels below 6.4, indicating stronger L-selectin/PSGL-1 interactions at slightly acidic pH. In contrast to a uniformly coated microbead, the surface of neutrophils primarily express L-selectin on the tips of microvilli *(167, 173)*. Neutrophils use these L-selectin-decorated microvilli to attach to the targeted surface expressing L-selectin receptors. Furthermore, neutrophils can passively deform and modulate the number of microvilli attached to the substrate in accordance with external stimuli to allow maximum stability—a mechanism that is unavailable to microspheres *(174, 175)*. These observations may explain why the effect of pH on L-

selectin/ PSGL-1 interactions are more pronounced on rolling micro- spheres than on neutrophils. However, the rolling flux for the microspheres exhibited the same behavior as neutro- phils: at lower pH conditions, a greater flux of rolling micro- spheres was observed on PSGL-1-coated surfaces (data not shown).

E-selectin/PSGL-1 adhesion at acidic pH—MD analysis

To complete our study of selectins, we performed a pKa analysis of E-selectin as shown in Figure 3.7. In this case, only two histidine residues were present, where the H25 predicted pKa was 6.8 (Table 3.3) and could change protonation states in slightly acidic conditions. However, H25 is not near the calcium ion and was not observed to increase amino acid contacts between E-selectin and PSGL-1 (structure not shown). Moreover, the N138 residue did not contact the lectin domain in either neutral or acidic conditions. Hence, pH is not expected to affect the binding strength or the binding affinity of PSGL-1 to E-selectin, and no significant change in rolling profiles is expected for cells expressing PSGL-1 when perfused over E-selectin-coated surfaces.

E-selectin/PSGL-1 adhesion at acidic pH— experimental rolling analysis

Figure 3.8a displays the rolling velocity profile for KG1a cells perfused through E-selectin-coated microtubes, where only a steady rise in rolling velocities was observed as the pH level became more acidic. However, the PSGL-1-coated microspheres did not demonstrate any significant change in rolling velocity at any pH level (Figure 3.8b). These data, along with the computational predictions, indicate that the pH range

investigated in this study does not significantly affect E-selectin/PSGL-1 binding dynamics.

3.5 CONCLUSIONS

Acidic extracellular pH does indeed alter the adhesion dynamics of certain selectins to PSGL-1, which causes differential rolling and adhesion characteristics of cells dependent on selectin-mediated rolling. P-selectin/PSGL-1 binding was enhanced at slightly acidic pH due to the formation of a new hydrogen bond between H114 (P-selectin) and Y7 (PSGL-1). As a result, the P-selectin/PSGL-1 binding lifetime increased, and, correspondingly, cell roll- ing velocities on P-selectin-coated surfaces were experimentally shown to decrease. When cells expressing L-selectin were perfused through PSGL-1-coated micro- tubes, cell flux increased at slightly acidic pH, whereas rolling velocities remained unchanged. The cell flux is primarily due to the altered structure of L-selectin at acidic pH, where the hydrogen bond between residue N138 (EGF domain) and the lectin-binding domain is dissociated as a result of protonating the H4 and H130 residues. The dissociation of this hydrogen bond allows L-selectin to assume a more flexible conformation (high affinity) that results in improved frequency of binding to PSGL-1. On the other hand, residue H110 is also predicted to be protonated when bound to L-selectin in acidic conditions that increase contacts and strengthen the binding interaction. We only observed this effect (i.e., slower rolling velocity) when we eliminated cellular effects by using L-selectin-coated micro- spheres. A previous study by Serrano et al. *(155)* also showed that neutrophil recruitment is enhanced in acidic conditions due to the upregulation of CD18 by the neutrophils. In this study, we showed

that before firm adhesion facilitated by the CD18/ICAM-1 interaction occurs, acidic pH also enhances neutrophil recruitment in the initial step of the adhesion cascade through the mediation of L-selectin/PSGL-1 binding dynamics. In contrast to P- and L-selectin, E-selectin/ PSGL-1 binding was not significantly affected by acidic pH. In conclusion, both theoretical predictions and experimental observations indicate that the extracellular pH level modulates selectin adhesion under flow. Thus, the extracellular pH level may serve as an external signaling stimulus for leukocytes trafficking during the inflammatory response. These results further suggest an additional axis that can be used to control applications such as the selectin-based isolation of CTCs and hematopoietic stem cells *(169, 176)*.

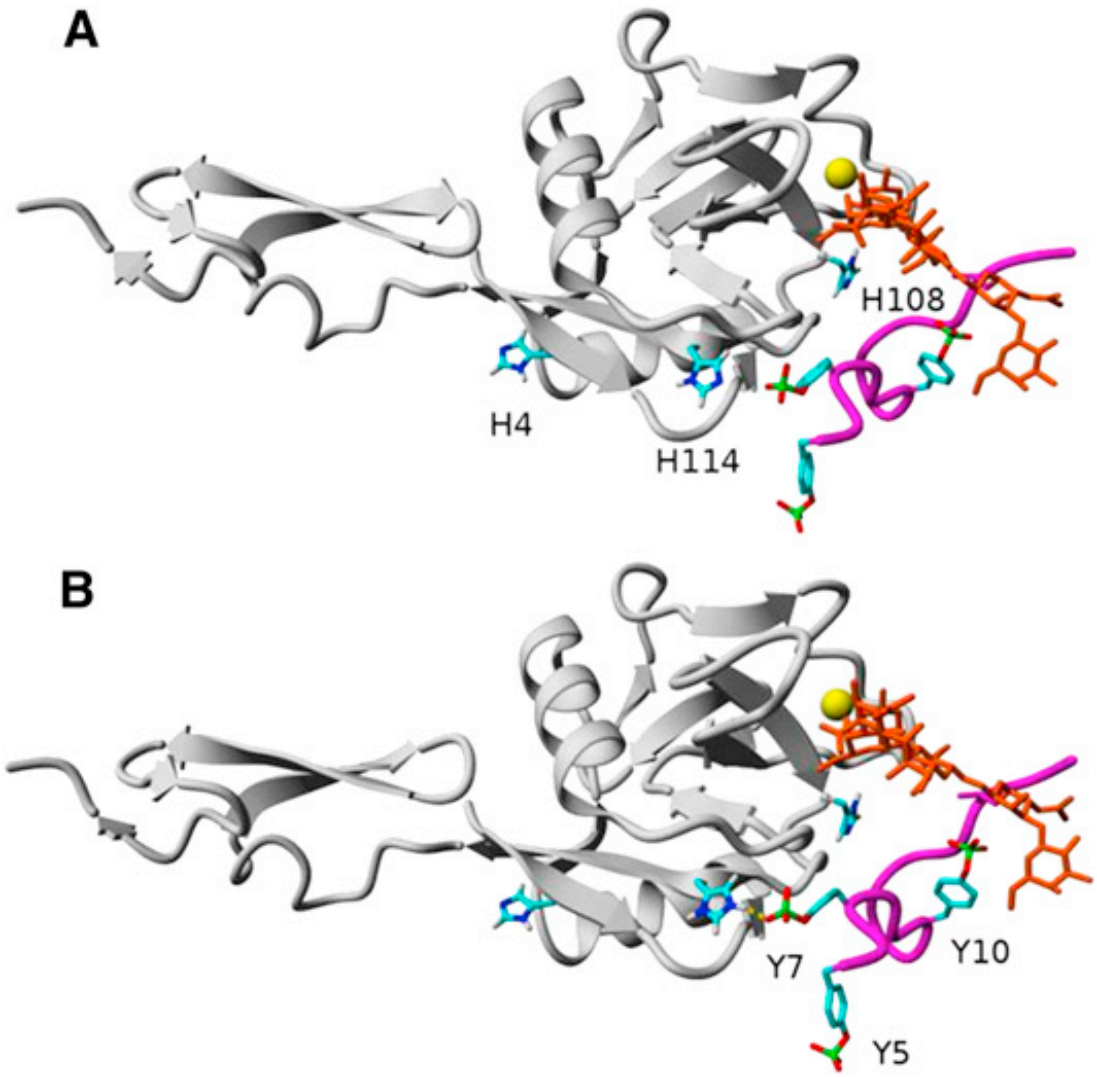

Figure 3.1: (A) Equilibrated PSGL-1 (magenta) and sLe^X (orange) structures bound to P-selectin (gray) at physiologically neutral pH. (B) Equilibrated P-selectin/PSGL-1 structure at physiologically acidic pH, where the H114/Y7 contact forms a hydrogen bond. All hydrogens except for those on the imidazoles of histidines are omitted for clarity, and the yellow sphere is the calcium ion. All figures available online in color. Adapted from T. Cao et al. Biophys. J. 104, 292–299 (2013).

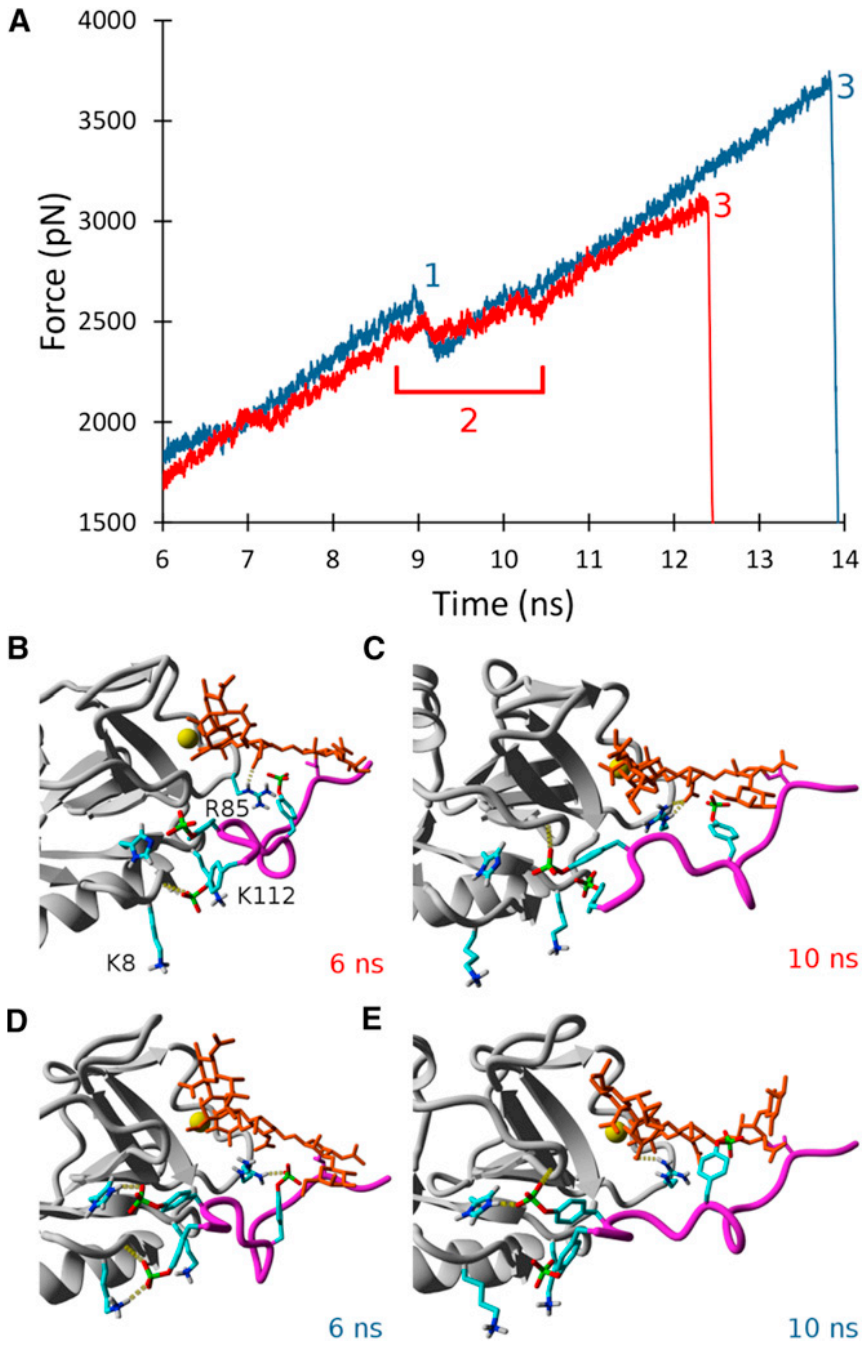

Figure 3.2: (A) Representative SMD force versus time graphs depicting the dissociation of PSGL-1 from P-selectin in physiologically neutral (red) and acidic (blue) conditions. Time point 1 represents the rupture of all amino acid contacts, except for coordination bonding, in the acidic case. Time point 2 represents a long force plateau in the neutral

case, where several sliding and rebinding events occur. Time point 3 represents the complete rupture of all bonds, leading to the dissociation of PSGL-1 from P-selectin in both conditions. (B) Representative P-selectin/PSGL-1 structure in neutral conditions for time periods < ~6 ns, where R85 forms a hydrogen bond with sLe^X, and Y5 forms a hydrogen bond with the back- bone structure of P-selectin. (C) Representative structure in neutral condi- tions for a time period > ~10 ns, where Y5 has no contacts and Y7 forms a contact with the backbone structure of P-selectin. (D) Representative structure in acidic conditions for time periods < ~6 ns, where Y5 has two hydrogen bonds with K8 and the backbone structure of P-selectin, Y7 forms a hydrogen bond to H114, and Y10 is hydrogen bound to R85. (E) Representative structure in acidic conditions for time periods > ~10 ns, where Y7 is still hydrogen bound to H114 and forms a hydrogen bond with the P-selectin backbone structure, and R85 is now hydrogen bound to sLe.^{X} Adapted from T. Cao et al. Biophys. J. 104, 292–299 (2013).

TABLE 1 Predicted histidine pKa values for unbound P-selectin (left) and P-selectin bound to PSGL-1 (right)

Residue	pKa	pKa*
H4	5.0	6.1
H108	5.8	5.9
H114	5.0	7.1

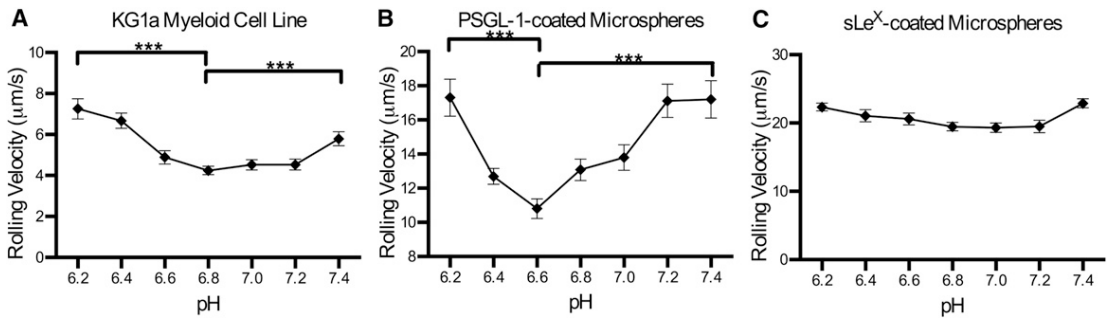

*Figure 3.3: (A) 10^6 cells/ml of KG1a cells were perfused through MRE tubing functionalized with 2 mg/ml of recombinant human P-selectin/Fc at a wall shear stress of 7 dyn/cm^2. (B and C) Protein-A-coated microspheres (10^6 beads/ml) functionalized with 14.47 mg/mg particles of recombinant human PSGL- 1/Fc (B), or with 0.017 mg/mg particles of sialyl Lewis-x-PAA-biotin (C) were perfused through MRE tubing functionalized with 10 mg/ml recombinant human P-selectin/Fc at a wall shear stress of 1 dyn/cm^2. Experiments were recorded for 1 min each at three randomly selected locations along the tube (unpaired t-test was performed; errors are mean 5 SE; *** $p < 0.0001$; $n = 3$). Adapted from T. Cao et al. Biophys. J. 104, 292–299 (2013).*

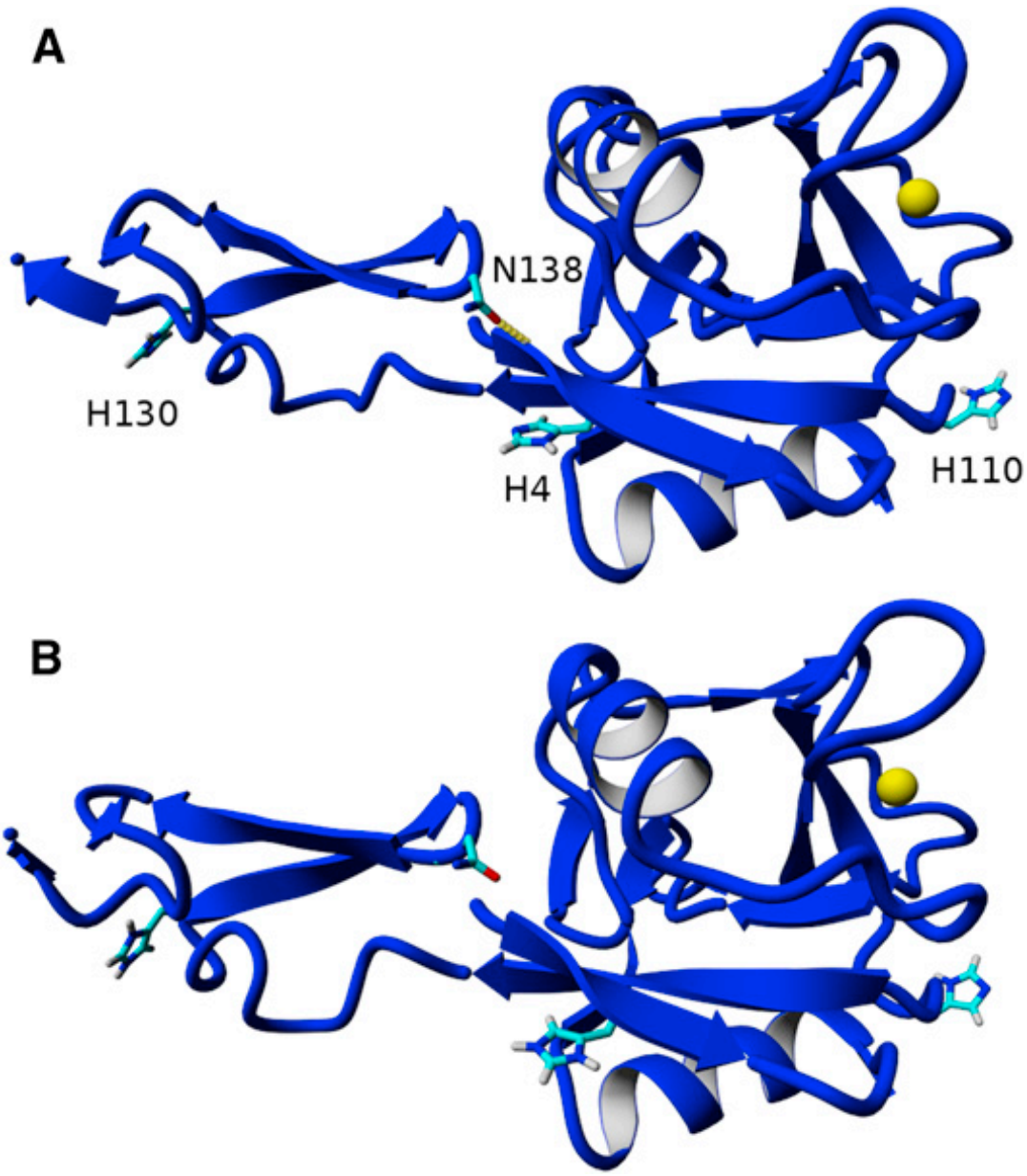

Figure 3.4: (A) Equilibrated L-selectin (blue) at physiologically neutral pH, where N138 is hydrogen bound to the backbone structure of L-selectin. (B) Equilibrated L-selectin structure at physiologically acidic pH, where N138 is no longer close enough to form a hydrogen bond. All hydrogens except for those on the imidazoles of histidines are omitted for clarity, and the yellow sphere is the calcium ion. Adapted from T. Cao et al. Biophys. J. 104, 292–299 (2013).

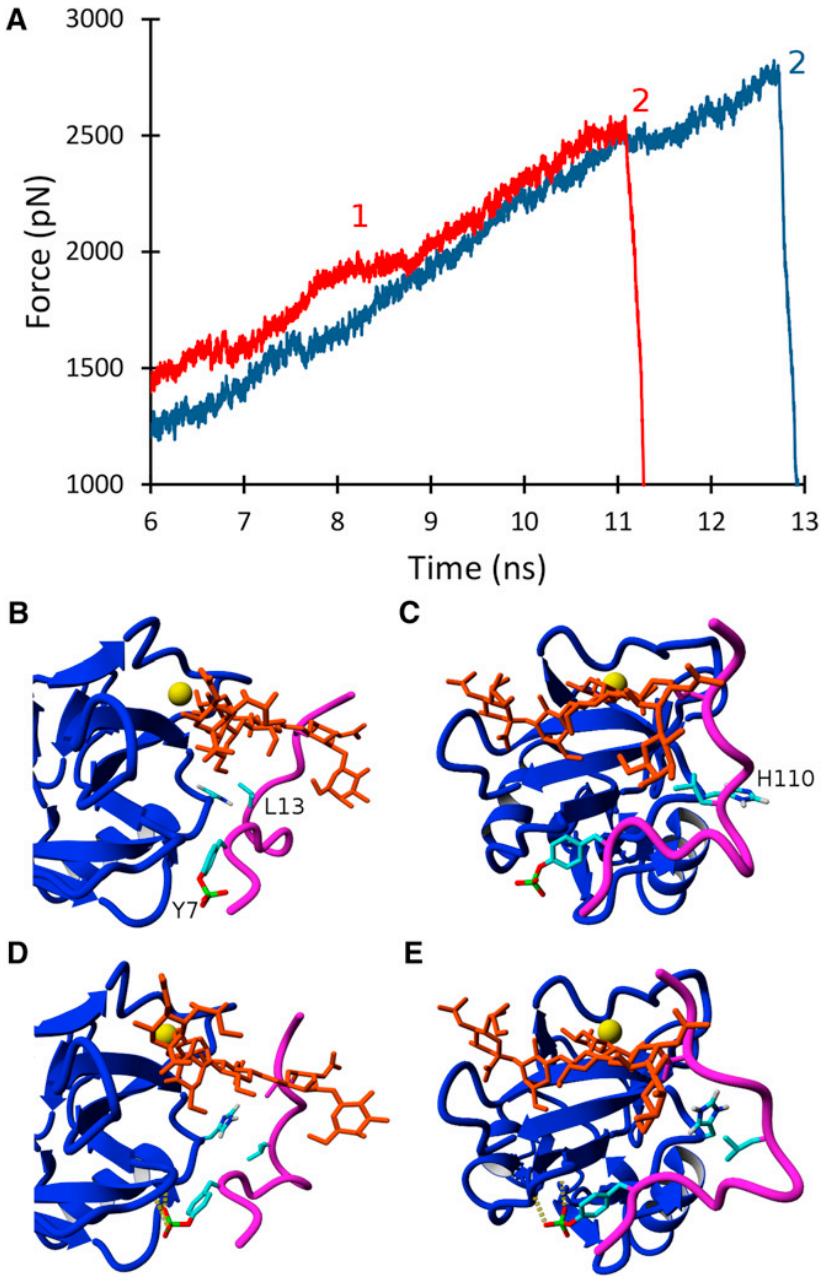

Figure 3.5: A Representative SMD force versus time graphs depicting the dissociation of PSGL-1 from L-selectin in physiologically neutral (red) and acidic (blue) conditions. Time interval 1 represents a long force plateau in the neutral case, where several sliding and rebinding events occur. Time point 2 represents the complete rupture of all bonds, leading to the dissociation of PSGL-1 from L-selectin in both conditions. (B and C)

Equilibrated PSGL-1 (magenta) and sLe^X (orange) structures bound to L-selectin (blue) at physiologically neutral pH. (D and E) Equilibrated PSGL-1/L-selectin structure at physiologically acidic pH, where Y7 forms contacts with the L-selectin backbone and L13 contacts H110 via a stacking interaction. Adapted from T. Cao et al. Biophys. J. 104, 292–299 (2013).

TABLE 2 Predicted histidine pKa values for unbound L-selectin (left) and L-selectin bound to PSGL-1 (right)

Residue	pKa	pKa*
H4	6.9	7.1
H110	4.6	6.5
H130	6.8	6.9

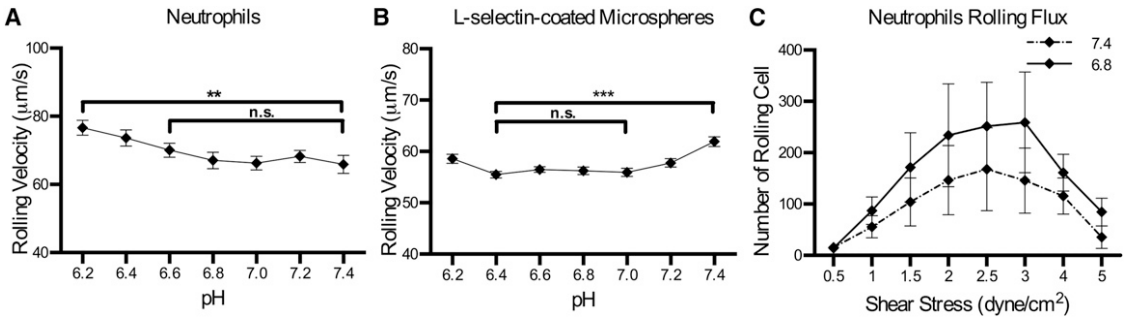

Figure 3.9 (A and B) Human neutrophils (10^6 cells/ml) (A) or protein-A-coated microspheres functionalized with 14.47 mg/mg particles of recombinant human L-selectin/Fc (B) were perfused through MRE tubing functionalized with 10 mg/ml of

*recombinant human PSGL-1/Fc at a wall shear stress of 2 dyn/cm^2. (C) Human neutrophils (10^6 cells/ml) were perfused in buffer of indicated pH through MRE tubing functionalized with 10 mg/ml recombinant human PSGL-1/Fc, and the number of rolling cells through the cross-sectional area of the tube was recorded for varying shear stresses (unpaired t-test; errors are mean 5 SE; ** $p < 0.0012$, *** $p < 0.0001$; $n = 3$ Adapted from T. Cao et al. Biophys. J. 104, 292–299 (2013).*

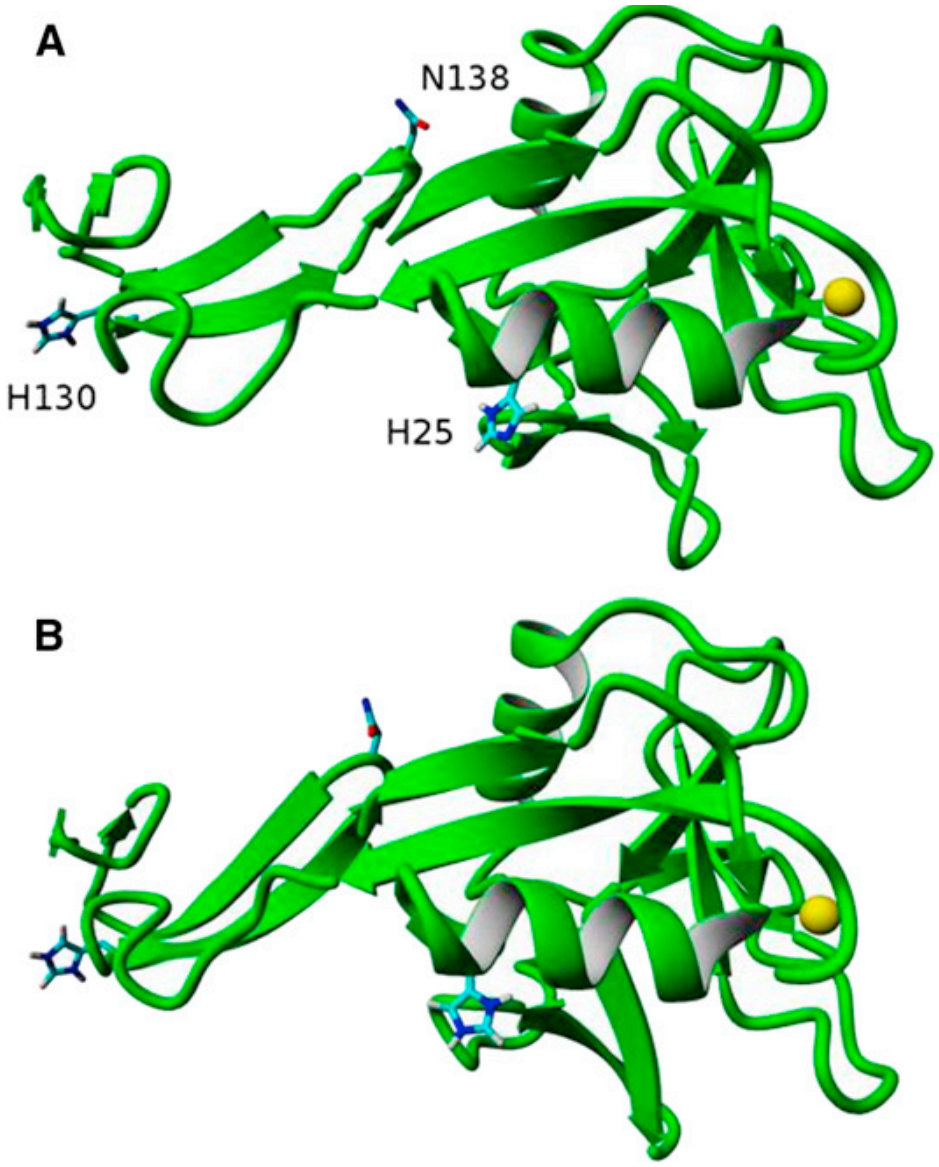

Figure 3.10: (A) Equilibrated E-selectin (green) at physiologically neutral pH. (B) Equilibrated E-selectin structure at physiologically acidic pH. All hydrogens except for those on the imidazoles of histidines are omitted for clarity, and the yellow sphere is the calcium ion. Adapted from T. Cao et al. Biophys. J. 104, 292–299 (2013).

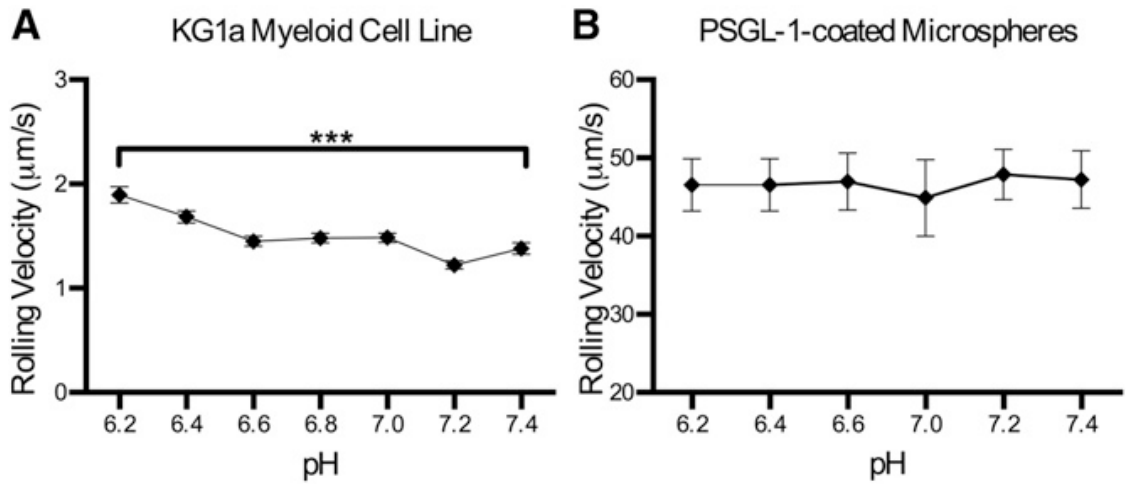

*Figure 3.11: (A and B) KG1a cells (10^6 cells/ml) (A) or protein-A-coated microspheres functionalized with 14.47 mg/mg particles of recombinant human E-Sel/Fc (B) were perfused through MRE tubing functionalized with 2 mg/ml of recombinant human E-selectin/Fc at a wall shear stress of 7 dyn/cm^2 (unpaired t-test; errors are mean 5 SE; *** $p < 0.0001$; $n = 3$). Adapted from T. Cao et al. Biophys. J. 104, 292–299 (2013).*

TABLE 3 Predicted histidine pKa values for unbound E-selectin (left) and E-selectin bound to PSGL-1 (right)

Residue	pKa	pKa*
H25	6.8	6.6
H130	7.8	7.4

CHAPTER 4

Stem Cell Enrichment with Selectin Receptors: Mimicking the pH Environment of Trauma

This chapter was published in *the Sensors (177)*.

4.1 ABSTRACT

The isolation of hematopoietic stem and progenitor cells (HSPCs) is critical for transplantation therapy and HSPC research, however current isolation techniques can be prohibitively expensive, time-consuming, and produce variable results. Selectin-coated microtubes have shown promise in rapidly isolating HSPCs from human bone marrow, but further purification of HSPCs remains a challenge. Herein, a biomimetic device for HSPC isolation is presented to mimic the acidic vascular microenvironment during trauma, which can enhance the binding frequency between L-selectin and its counter-receptor PSGL-1 and HSPCs. Under acidic pH conditions, L-selectin coated microtubes enhanced CD34+ HSPC adhesion, as evidenced by decreased cell rolling velocity and increased rolling flux. Dynamic light scattering was utilized as a novel sensor to confirm an L-selectin conformational change under acidic conditions, as previously predicted by molecular dynamics. These results suggest that mimicking the acidic conditions of trauma can induce a conformational extension of L-selectin, which can be utilized for flow-based, clinical isolation of HSPCs.

4.2 INTRODUCTION

Human hematopoietic stem and progenitor cells (HSPCs) originating from the bone marrow (BM) play a critical role in treating many hematological malignancies due to their unique multipotent, stem cell quality *(178, 179)*. In cancer patients with depleted immune cells, HSPCs transplantation is used to repopulate blood cell lineages *(180, 181)*. On the other hand, increasing evidence has shown that mutagenesis which occurs during the development of HSPCs converts these cells to leukemic stem cells *(182, 183)*. Therefore, a reliable and simple means for the acquisition and enrichment of HSPCs for both transplantation therapy and to better understand leukemia is needed. HSPCs routinely leave the BM to enter the circulatory system and distant tissues to establish and maintain hematopoiesis *(184–187)*. During embryogenesis, HSPCs migrate to the fetal liver and differentiate *(188–190)*. In adults, HSPCs participate in the innate immune response against foreign antigens *(191–193)*. HSPCs express a repertoire of surface ligands that include unique markers as well as markers shared with leukocytes and circulating tumor cells *(64, 66)* that can bind the family of adhesion molecules called selectins (E-, L- and P-), which facilitates their migration from (and to) the BM and distant tissues *(169, 194–197)*. In a recent study, we observed that acidic extracellular pH enhances L-selectin:PSGL-1 interactions under flow *(136)*. Extracellular pH becomes acidic during the early stages of wound healing and inflammation *(198, 199)* which is also a period of elevated recruitment of HSPCs to target sites *(200, 201)*. It follows that HSPCs may experience altered adhesion due to L-selectin:ligand binding in acidic environments. In this study, we determined that L-selectin ligands expressed on the surface of HSPCs bind with enhanced affinity to L-selectin under acidic extracellular pH. Furthermore, the

enhanced L-selectin:ligand binding affinity is due to L-selectin undergoing conformational change in acidic pH as quantified by dynamic light scattering measurements of selectin-PEG-decocorated liposomes. Finally, by mimicking this physiological phenomenon, we demonstrate its potential use to capture and enrich HSPCs by perfusing a suspension of BM cells through L-selectin coated microtubes under acidic pH.

4.3 MATERIALS AND METHODS

Reagents and Antibodies

Phosphate-buffered saline (PBS) and Hank's balanced salt solution (HBSS) were purchased from Invitrogen (Grand Island, NY, USA). Recombinant human P-, L-, and E-selectin/IgG chimera were purchased from R&D Systems (Minneapolis, MN, USA). Phycoerythrin (PE)-conjugated mouse anti-human CD34 (clone 581) and PE-conjugated mouse IgG1 κ-isotype control were purchased from Biolegend (San Diego, CA, USA). APC-conjugated mouse anti-human L-selectin (clone DREG-56) was purchased from BD Biosciences (San Jose, CA, USA).

Isolation of Bone Marrow

Cells Bone narrow mononuclear cells (MNCs) were extracted from consenting adult donors following a protocol approved by the Research Subjects Review Board of the University of Rochester, as described previously *(169)*. Briefly, bone marrow samples were diluted 3-fold (vol/vol) in Ca2+ and Mg2+-free PBS, with 35 mL of the diluted sample carefully layered over 15 mL Ficoll cell separation solution (GE Healthcare,

Piscataway, NJ, USA) in 50 mL Falcon tubes. Samples were then centrifuged at 800 g for 20 min at RT to separate bone marrow MNCs from excess cells and tissue debris. The buffy coat of MNCs was extracted and place into a separate tube and washed twice in PBS. Bone marrow MNCs were quantified and placed in flow buffer (PBS supplemented with Ca2+) for flow-based assays.

Isolation of CD34+ Population using Microbeads

To characterize the rolling characteristics of CD34+ HSPCs in acidic pH, CD34+ bone marrow HSPCs were isolated using EasySep Human CD34 Positive Selection Kit by StemCell Technology (Vanvouver, BC, Canada) per manufacturer's instructions. Briefly, a solution of mononuclear cells was incubated with tetrameric antibody complexes against CD34 for 15 min, followed by incubation with dextran-coated magnetic nanoparticles (MNP) for 10 min. The cell-containing tube was then placed in an EasySep® magnet for positive selectin, allowing the MNP-conjugated CD34+ cells to remain in the tube while the supernatant was poured off. The cell population was washed, and the magnetic separation was repeated until the desired purity was achieved.

Microtube Functionalization

Micro-renathane (MRE) tubes (300 μm inner diameter, 50 cm long; Braintree Scientific, Braintree, MA, USA) were sterilized with 80% ethanol for 10 min. The tubes were then washed (3×) with PBS buffer (Ca2+-free). The inner surface was functionalized with recombinant human L-selectin/Fc at specified concentration for 2 h. The microtubes were then incubated in PBS supplemented with dry milk (5% w/v; Sigma-Aldrich, St. Louis,

MO, USA) for 1 h to prevent nonspecific adhesion. All steps were performed at room temperature (RT). In several experiments microtubes were labeled with APC conjugated mouse anti human L-selectin for 30 min. Microtubes were washed three times with buffer and images were acquired on an inverted research microscope (Olympus America, Melville, NY, USA).

Flow-Based Cell Adhesion Assay

Cells suspended in PBS buffer (supplemented with 2 mM Ca2+) at a specified pH (6.6 or 7.4) were perfused through functionalized microtubes using a syringe pump at a wall shear stress of 2.0 dynes (dyn)/cm2 . Videos of rolling cells were captured and analyzed using ImageJ (US National Institutes of Health, Bethesda, MD, USA). Cell rolling velocity was determined by measuring the displacement of a rolling cell over time, while rolling flux was determined by quantifying the number of rolling cells entering the image frame over the course of 1 min. 2.6. CD34+ HSPC Flow-Based Isolation A cell suspension of bone marrow MNCs (5 × 106 cell/mL) in PBS buffer (supplemented with 2 mM Ca2+) at specified pH was perfused through L-selectin functionalized microtubes at a wall shear stress of 1.0 dyn/cm2. To collect captured cells, the microtube was incubated with fresh PBS buffer (Ca2+ free and supplemented with 2 mM of EDTA) for 15 min, and then the cell gently collected into a 1.5 mL Eppendorf tube. Captured cells were also detached from the surface via air embolism. An air bubble is introduced into the microtube using an empty syringe. The bubble is then slowly pushed through the entire length of the microtube to dislodge any remaining captured cells into the collecting tube at the opposing end.

Preparation of Selectin-Conjugated Liposomes

Multilamellar liposomes were prepared using a thin lipid film hydration method as previously described *(202, 203)*. Briefly, lipids were hydrated in 125 mM ammonium sulfate (Sigma-Aldrich) to form multilamellar liposomes, followed by 10 freeze-thaw cycles and then extrusion as previously described *(204, 205)* to prepare unilamellar liposomes. Recombinant human E-, L-, and P-selectin/Fc chimera (rhE/Fc) (R&D Systems, Minneapolis, MN, USA) was conjugated to 1,2-distearoyl-sn-glycero-3-phosphoethanolamine-N-maleimide 2000 (DSPE-PEG2000 maleimide) (Avanti Polar Lipids, Alabaster, AL, USA) via thiolation, and PEG or selectin-PEG conjuguates were covalently attached to diluted unilamellar liposomes as described previously *(206)*. All liposomes were stored at 4 °C for no more than one week until usage.

Dynamic Light Scattering

To detect changes in selectin protein conformation, freshly prepared selectin-conjugated liposomes (<24 h) were diluted (1,000×) in buffer at specified pH. To remove aggregates, samples were filtered through a 0.45 μm filter (MicroLiter Analytical Supplies, Inc., Suwanee, GA, USA). Samples were analyzed for changes in particle size and polydispersity index (PDI) using a Malvern Zetasizer Nano-ZS (Malvern, Worcestershire, UK).

Flow Cytometry

Isolated cells were stained with mouse anti-human CD34 (clone 581), or mouse IgG1 κ-isotype purchased from Biolegend (San Diego, CA, USA). Cells were washed twice with

PBS (supplemented with 1% BSA) and then incubated with antibody at 4 °C for 30 min. Cells were washed twice with buffer and analyzed using a Guava EasyCyte flow cytometer (Millipore, Billerica, MA, USA). CD34+ post-isolation cell populations were quantified and plotted using FlowJo software (Treestar Inc., San Carlos, CA, USA).

Statistical Analysis

Cell rolling velocity and flux were plotted and statistically analyzed using Prism (GraphPad Software, San Diego, CA, USA). Two-tailed unpaired t-test was used to determine statistical significance.

4.4 RESULTS AND DISCUSSION

CD34+ Human BM Cell Interaction with L-Selectin is Enhanced under Acidic Extracellular pH

To characterize the influence of acidic extracellular pH on the interaction of human HSPCs and L-selectin, CD34+ cells were perfused through microtubes coated with L-selectin (Figure 4.1A) at 2 dyn/cm^2. This level of shear stress was chosen because it is within the physiological shear stress range that mononuclear cells experience in the human circulatory system. CD34+ cells exhibited a significantly lower rolling velocity on L-selectin under acidic conditions (Figure 4.1D), when compared to L-selectin mediated CD34+ cell rolling at a pH of 7.4. At pH 6.6, CD34+ cells had an average rolling velocity of 22.14 ± 1.87 μm/s, compared to an average rolling velocity of 31.24 ± 3.23 μm/s at pH 7.4. This indicates that under acidic conditions, CD34+ HSPCs experience enhanced binding to L-selectin. To show that the observed interaction between the

perfused cells and the coated microtube is L-selectin:ligand specific, cells were perfused through microtubes coated with milk alone. Cell adhesion was not observed in this case (Figure 1B). In contrast, microtubes coated with L-selectin showed extensive cell rolling and adhesion (Figure 4.1C). In addition, Ca^{2+}-dependent cell rolling *(207, 208)* was abrogated by perfusion with HBSS (Ca^{2+} free buffer supplemented with 2mM EDTA) (data not shown) thus confirming that cell interaction was mediated specifically by L-selectin:ligand adhesion. The average rolling velocity of CD34+ cells was significantly lower compared to MNCs from bone marrow (Figure 4.1E). This observation supports previous work, which suggested that CD34+ cells have stronger binding affinity to L-selectin than CD34- cells *(209)*. In contrast, no significant differences in CD34- cells were observed under physiological and acidic pH conditions (Figure 4.1E). An increase in cell rolling flux of MNCs in acidic pH was also found, in comparison to the cell flux measured at physiological pH (Figure 4.2). These results suggest that acidic pH can be utilized to enhance the number of cell interactions with the L-selectin coating, thus improving the number of cells captured.

Previous work showed that L-selectin can adopt an "extended" (high affinity) conformation with a point mutation of an amino acid in the EGF domain of L-selectin *(172)*. This extended conformation results in decreased cell rolling velocity, and an increase in cell flux on the L-selectin ligand PSGL-1. Furthermore, it was previously established that pH can encourage L-selectin to adopt this extended, high affinity conformation due to the abolition of hydrogen bonding between the EGF and lectin domains of L-selectin which normally confines the protein in the "low affinity" conformation *(136)*. Therefore, we sought to determine whether acidic pH can induce a

measurable, extended conformation of L-selectin. Dynamic light scattering (DLS) was utilized to determine changes in the protein size of selectins (E, P and L) presented on nanoscale liposomes in buffer at specified pH. While liposomes in the absence of selectin protein (Table 4.1) or conjugated with E- or P-selectin exhibited minimal, non-significant changes in hydrodynamic radius (Figure 4.3), L-selectin significantly increased its average length by 1.3 nm (Figure 4.3, Table 4.1) as evidenced by an increase in hydrodynamic radius.

Together, these results indicate that, in comparison to physiological pH, L-selectin can extend its conformation under acidic pH, which is consistent with an observed enhancement in CD34+ cell adhesion. An extended conformation of L-selectin can allow the protein to bind to its ligands more strongly and at higher frequency, as evidenced by a lower CD34+ cell rolling velocity and increased flux (Figure 4.4).

Selectin-coated microdevices have been shown to effectively capture viable stem cells *(210, 211)* and circulating tumor cells from whole blood with high yield *(212)*. To mimic the physiological phenomenon of L-selectin:ligand interaction under acidic conditions for the isolation and enrichment of CD34+ bone marrow cells, low-density bone marrow cells isolated from healthy adult donors using Ficoll were perfused at a concentration 5×10^6 cells/ml through L-selectin coated microtubes (50 μg/mL) at 1.0 dyn/cm^2 in PBS buffer supplemented with 2 mM Ca^{2+}. Adherent cells were dislodged from the surface using both buffer supplemented with 2 mM EDTA and air embolism. Isolated cells were stained using an anti-CD34 monoclonal antibody. L-selectin coated microtubes were

found to capture and enrich CD34+ HSPCs from the bone marrow at >19% purity (Figure 4.5).

4.5 CONCLUSIONS

During tissue inflammation, extracellular pH can become increasingly acidic. Furthermore, it is also known that HSPCs are recruited to sites of inflammation via selectin-mediated cell rolling. In this study, we showed that acidic extracellular pH enhances CD34+ HSPCs adhesion to L-selectin, consistent with a measurable extended conformational change of L-selectin to a "high affinity" orientation in acidic pH. This conformational change is taken to increase the frequency of L-selectin:ligand binding. These biophysical insights were applied to the isolation and enrichment of CD34+ HSPCs from bone marrow using an L-selectin coated microtube. The described biomimetic technique allows for both rapid and simple isolation of viable CD34+ HSPCs from patient bone marrow.

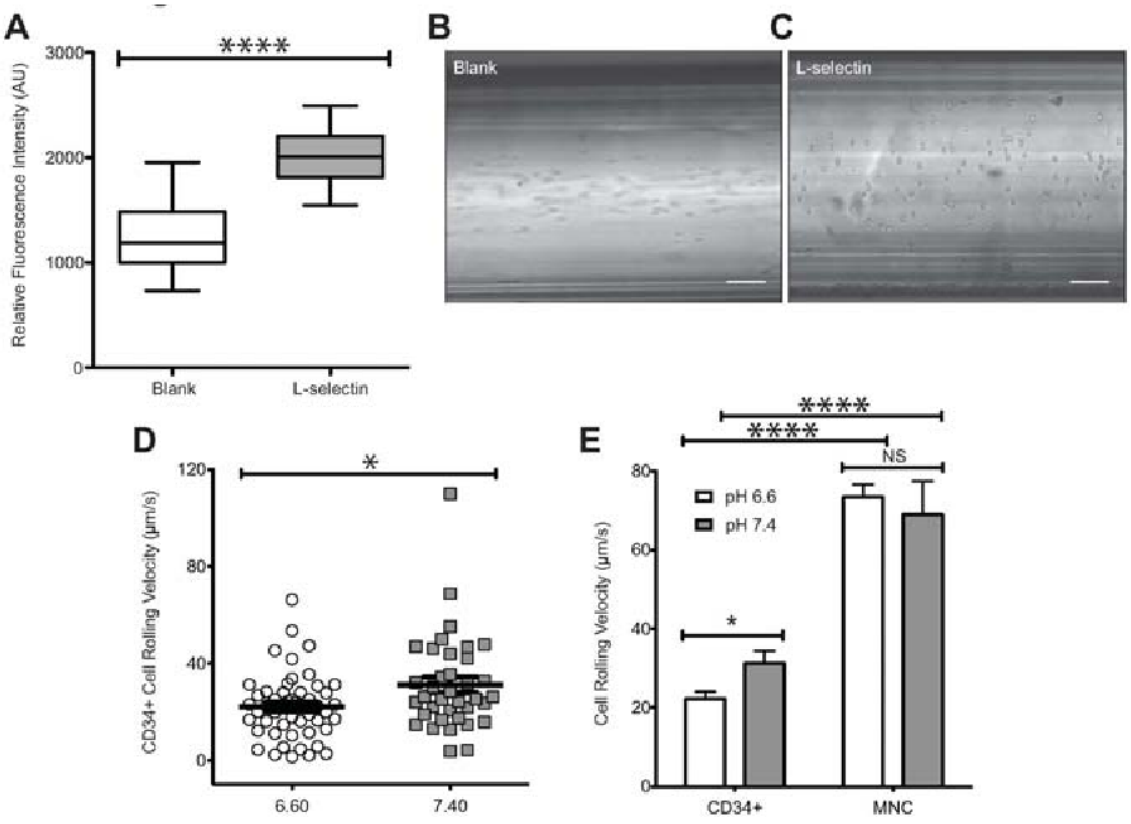

*Figure 4.1: Enhanced adhesion of CD34+ cells to L-selectin at acidic pH. (A) Relative fluorescence intensity of L-selectin coated and blank microtubes labeled with APC-anti human L-selectin. (B–C) Images of perfused cells interacting with blank or functionalized microtubes, respectively. Scale bars are 100 µm. (D) Rolling velocity of CD34+ cells under normal (7.4) and acidic (6.6) pH. CD34+ cells at a concentration of 1 × 106 cells/mL were perfused through L-selectin coated (20 µg/mL) microtubes at a shear stress of 2.0 dyn/cm2 in buffer at specified pH. (E) Comparison of rolling velocities of CD34+ cells and MNCs (unpaired t-test, error bars indicate standard error of the mean; * $p < 0.05$, **** $p < 0.0001$; $n = 3$). Adapted from T. Cao et al. Sensors (Switzerland)* (2013).

Lyposome Type	Radius (nm) pH 7.4	Radius (nm) pH 6.6	PDI pH 7.4	PDI pH 6.6
PEG only	52.33 ± 0.83	52.99 ± 0.95	0.103 ± 0.008	0.102 ± 0.013
PEG + ES	74.06 ± 0.94	74.86 ± 1.18	0.101 ± 0.008	0.105 ± 0.007
PEG + LS	61.10 ± 0.99	63.08 ± 0.94	0.102 ± 0.011	0.101 ± 0.007
PEG + PS	83.65 ± 1.17	84.57 ± 0.83	0.108 ± 0.007	0.106 ± 0.009

Table 4.1: Mean particle radius and polydispersity index (PDI) measurements of selectin-coated liposome samples under neutral and acidic conditions. Data reported as mean ± standard deviation. Results recorded in triplicate. Adapted from T. Cao et al. Sensors (Switzerland) (2013).

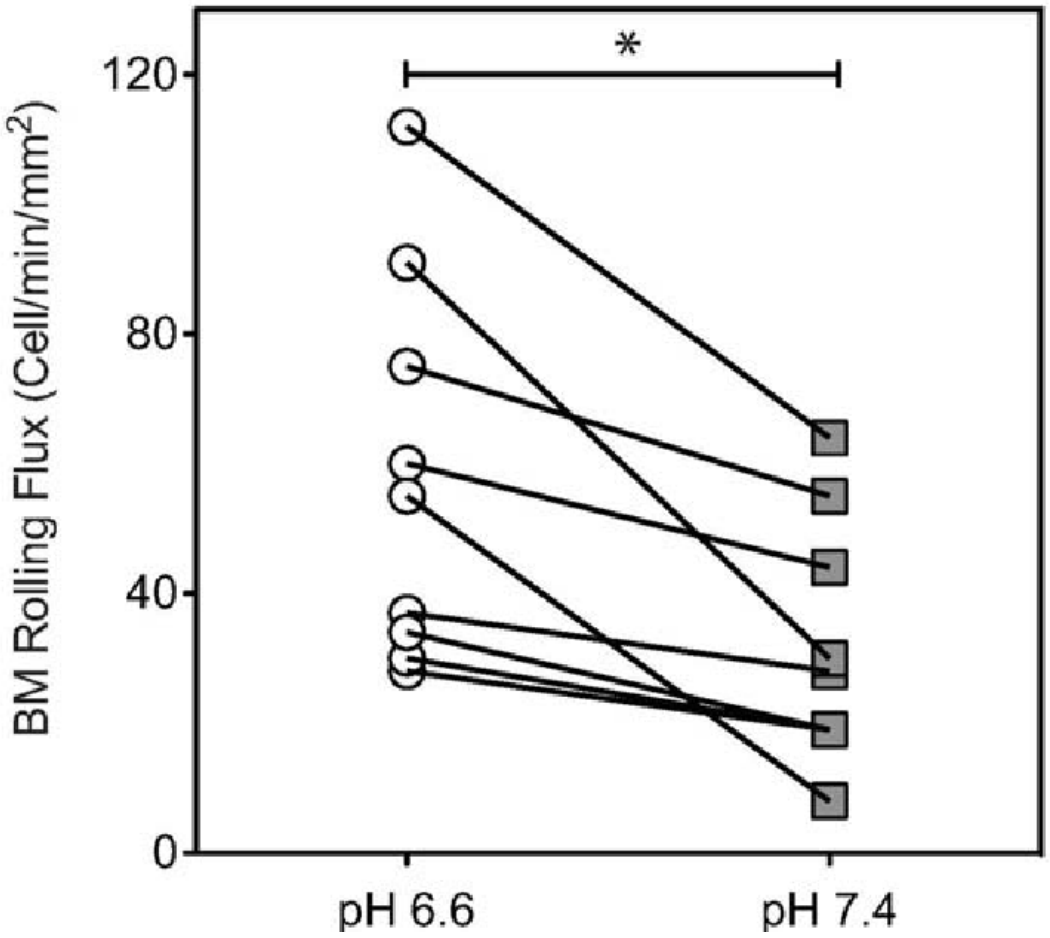

*Figure 4.2: MNCs isolated from bone marrow display higher binding affinity to L-selectin in acidic pH. A suspension of MNCs (1 × 106 cells/mL) was perfused through L-selectin coated (20 μg/mL) microtubes at a shear stress of 2.0 dyn/cm2 in buffer at specified pH. Cell rolling flux was measured by counting the number of rolling cells crossing into the image frame over 1 min (unpaired t-test, error bars indicate standard error of the mean; * $p < 0.05$; $n = 3$). Adapted from T. Cao et al. Sensors (Switzerland)* (2013).

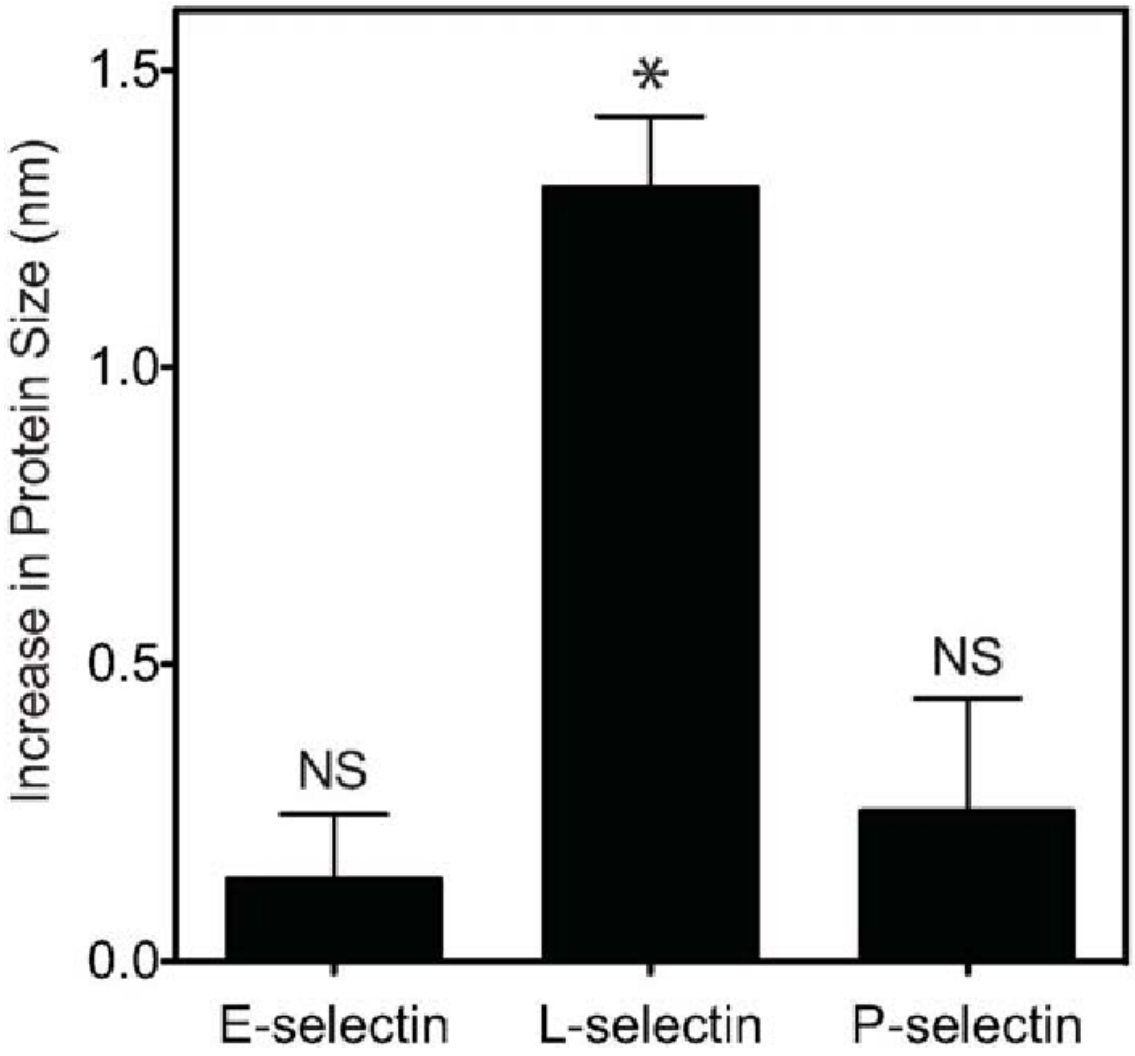

*Figure 4.3: Extension of E-, L-, and P-selectin protein size (in nanometers) upon exposure to acidic (pH 6.6) conditions. Changes in E-, L-, and P-selectin protein size were determined using dynamic light scattering by subtracting the mean particle radius of selectin-coated liposomes under neutral conditions from the mean particle radius of selectin-coated liposomes under acidic conditions. * $p < 0.05$. NS = not significant. Adapted from T. Cao et al. Sensors (Switzerland)* (2013).

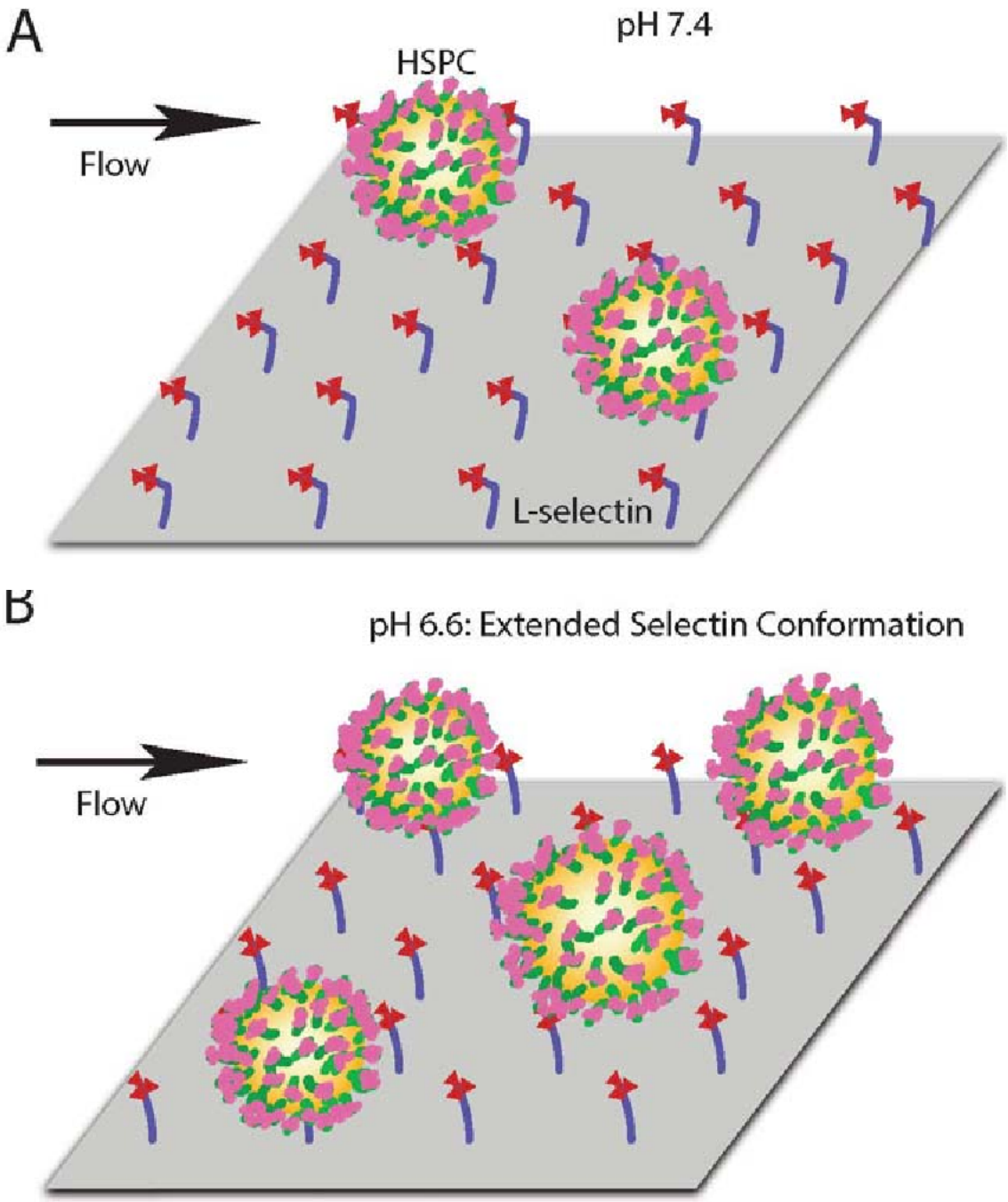

Figure 4.4: Schematic of increased HSPC adhesion to L-selectin in high affinity, extended conformation under acidic pH (B) compared to the lower affinity, bent conformation (A). Adapted from T. Cao et al. Sensors (Switzerland) (2013).

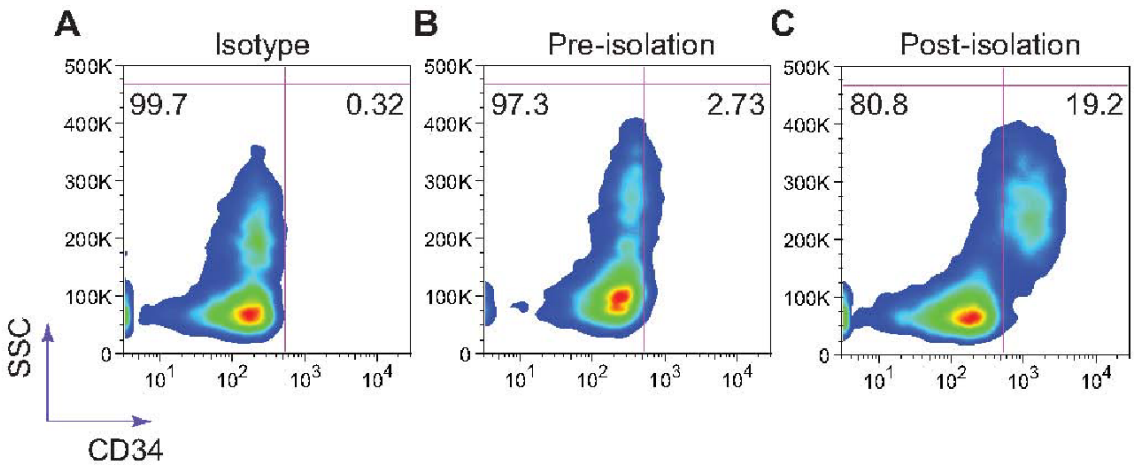

Figure 4.5: L-selectin mediated isolation of CD34+ cells from patient bone marrow samples under acidic pH. Captured cells were labeled using a mouse anti-human CD34 monoclonal antibody. Flow cytometry plots are a representation of experiments done in triplicate. SSC = side scatter. Adapted from T. Cao et al. Sensors (Switzerland) (2013).

CHAPTER 5

Comparison of human and mouse E- selectin binding to Sialyl-Lewis^{x}

This chapter was published in *the Sensors (213).*

5.1 ABSTRACT

Background: During inflammation, leukocytes are captured by the selectin family of adhesion receptors lining blood vessels to facilitate exit from the bloodstream. E-selectin is upregulated on stimulated endothelial cells and binds to several ligands on the surface of leukocytes. Selectin:ligand interactions are mediated in part by the interaction between the lectin domain and Sialyl-Lewis x (sLe^{X}), a tetrasaccharide common to selectin ligands. There is a high degree of homology between selectins of various species: about 72 and 60 % in the lectin and EGF domains, respectively. In this study, molecular dynamics, docking, and steered molecular dynamics simulations were used to compare the binding and dissociation mechanisms of sLe^{X} with mouse and human E-selectin. First, a mouse E-selectin homology model was generated using the human E-selectin crystal structure as a template.

Results: Mouse E-selectin was found to have a greater interdomain angle, which has been previously shown to correlate with stronger binding among selectins. sLe^{X} was docked onto human and mouse E-selectin, and the mouse complex was found to have a higher free energy of binding and a lower dissociation constant, suggesting stronger binding. The mouse complex had higher flexibility in a few key residues. Finally, steered

molecular dynamics was used to dissociate the complexes at force loading rates of 2000–5000 pm/ps^2. The mouse complex took longer to dissociate at every force loading rate and the difference was statistically significant at 3000 pm/ps^2. When sLe^x-coated microspheres were perfused through microtubes coated with human or mouse E-selectin, the particles rolled more slowly on mouse E-selectin.

Conclusions: Both molecular dynamics simulations and microsphere adhesion experiments show that mouse E-selectin protein binds more strongly to sialyl Lewis x ligand than human E-selectin. This difference was explained by a greater interdomain angle for mouse E-selectin, and greater flexibility in key residues. Future work could introduce similar amino acid substitutions into the human E-selectin sequence to further modulate adhesion behavior.

Keywords: E-selectin, Receptor, Cell adhesion, Molecular dynamics, Docking, Steered molecular dynamics

5.2 INTRODUCTION

Selectins are a family of transmembrane adhesion molecules that mediate the inflammatory response and the cancer metastasis cascade. There are three members of the selectin family: P(latelet)-selectin, E(ndothelial)-selectin, and L(eukocyte)-selectin. All three contain an N-terminal lectin domain, epidermal-growth-factor-like (EGF) domain, a varying number of consensus repeat units, a transmembrane portion, and a cytoplasmic tail *(170, 214, 215)*. During inflammation, fast binding and dissociation of bonds between cells and endothelium contributes to rolling. Selectin:ligand interactions

are mediated partially by the interaction between the lectin domain and Sialyl Lewis x (sLe^X), a tetra saccharide on cell surface proteins common to selectin ligands. E-selectin binds particularly well to PSGL-1, CD44, and ESL-1 *(170, 216)*.

There is a high degree of amino acid identity between selectins of various species: about 72 and 60 % in the lec- tin and EGF domains, respectively *(215)*. Mouse E-selectin differs from human E-selectin by 29 substitutions in the lectin and EGF domains (Figure 5.1). The amino acid differences between human and mouse E-selectin are fairly evenly distributed within and between the domains (Figure 5.1).

Molecule conformational changes are essential to physio- logical processes *(217)*. Selectin interdomain hinge flexibility greatly affects the on-rate of selectin:ligand binding. All the selectins have shown "open" and "closed" states that correspond to whether or not they are in complex; for instance, there is a 52° increase in the interdomain angle from unliganded P-selectin to P-selectin in complex *(159)*. Hydro- dynamic forces in the bloodstream favor the open conformation as it can strengthen selectin:ligand bonds *(172)*. A flexible hinge encourages the oscillation between the two states, which facilitates greater range of motion for the lectin domain and thus provides more opportunity for binding *(218, 219)*. Lou et al. used molecular dynamics (MD) and site mutagenesis at the interdomain hinge of L-selectin to learn that increasing hinge flexibility via mutation caused an in- crease in binding on- and off-rates of selectin:ligand interactions *(166)*. Of particular interest are the binding site and interdomain angle, since prior dissociation studies of P- selectin:sLe^X suggest these to be important modulators of dissociation time and final conformation *(220)*.

MD simulations are a useful tool to study the movement of a protein chain over time, given specified starting parameters *(221)*. The goal of this study was to determine how the structural differences between human and mouse E-selectin affect their corresponding binding and thus cell rolling behavior. MD, docking, and steered molecular dynamics (SMD) were used in conjugation with microtube rolling experiments to address this link between molecular properties and cellular scale adhesion phenomena under flow.

5.3 MATERIALS AND METHODS

MD to prepare receptor (E-selectin or mutants) for docking the lectin and EGF crystal structure of human E- selectin (1ESL) was obtained from the Protein Data Bank to provide starting atomic coordinates. The lectin and EGF domains are the effective binding unit of E-selectin.

The E-selectin:sLe^X complex crystal structure (1G1T) was not used as a starting structure as the bound com- plex does not allow for full flexibility of E-selectin when amino acid substitutions are made. MD, docking, and SMD simulations were performed using the YASARA (YASARA Biosciences GmbH, Vienna, Austria) package of MD programs with the YAMBER3 self-parameterizing force field. For all simulations, the temperature and pressure were held constant at 298 K and 1 atm, respectively. Other parameters used include periodic boundary conditions, the particle mesh Ewald method for electro- static interactions, and the recommended 7.86 Å force cutoff for long-range interactions *(136)*. A predicted model of mouse E-selectin was created using human E- selectin as a template and substituting 29 residues.

For equilibrium simulations, human and mouse E- selectin were each solvated in a water box and neutralized by adding Na^+ and Cl^- ions to a concentration of ~50 mM. To allow for free protein rotation, the water box was de- fined as a cube with sides 80 Å, at least 10 Å from the structure. The conformational stresses were removed using short steepest-descent minimizations followed by simulated annealing until sufficient convergences were reached. Free dynamics simulations were run for 10 ns. Similar equilibration simulations were run for sLe^X (taken from the 1G1T PDB structure) with a water box of size 30 × 30 × 30 Å. The average structure for each simulation run was used for further simulation steps.

Binding sLe^X to human and mouse E-selectin

Molecular docking predicts the conformation of a protein-ligand complex and enables calculation of the binding affinity *(221)*. sLe^X was docked to the human and mouse E-selectin structures using the AutoDock program with YAMBER3 force field. sLe^X was allowed full flexibility and E-selectin had a fixed backbone with flex- ible sidechains. 250 docking runs were completed, and the AutoDock scoring function sorted the runs by

binding energy. Complex conformations were assumed to be different if the ligand RMSD was greater than 5 Å. Of the final conformations with positive binding energy, those for which there was no contact (5 Å or less) be- tween the fucose residue of sLe^X and the calcium ion were eliminated as they would not be physiologically realistic. The docked complexes were solvated using the same MD steps as before with a water box of size 100 × 100 × 100 Å. The distance from the ligand to the calcium ion was analyzed

over the simulation, and if it remained relatively constant, the complex was considered stable. The average free dynamics complex structures were used for the subsequent dissociation steps.

SMD to simulate dissociation under applied force

SMD was used to simulate dissociation under applied force. Constant acceleration was applied to the ligand center of mass to move it away from the receptor center of mass. The simulations were run until all the hydrogen bonds between sLe^X and E-selectin broke and the two proteins dissociated.

Microtube functionalization

Microrenathane tubes (300 μm i.d. and 50 cm long; Braintree Scientific, Braintree, MA) were sterilized with 75 % ethanol for 15 min. After three washes with PBS, the inner luminal surface was functionalized with recombinant human E-selectin (5 μg/mL) by incubating for 2 h, to allow for passive adsorption to the surface. Next, the microtubes were then incubated with dry milk powder (5 % w/v) in PBS for 1 h to prevent nonspecific adhesion. For control experiments, microtubes were pre- pared as indicated above except that E-selectin was replaced with BSA.

Microsphere functionalization

SuperAvidin-coated microspheres (9.94 μm diameter; CP01N, Bangs Laboratories, Fishers, ID) were washed with PBS buffer per manufacture instruction. Next, the microspheres were incubated with Sialyl-$Lewis^X$-biotin at specified concentrations for 1

h with gentle mixing every 15 min. Finally, the microspheres were washed twice and resuspended in flow buffer (PBS supplemented with 2 mM Ca^{2+}). The surface density of sLe^x on the microspheres was not measured in this study, however our previous work with similar sLe^x-coated microspheres and selectin surface coatings show that these materials re- create the physiological rolling behavior of leukocytes in the vasculature, with comparable rolling velocities *(222)*.

Rolling experiment

Functionalized microspheres ($2x10^6$/mL) suspended in flow buffer were perfused through the microtubes using a syringe pump at 8 dyne/cm^2. Recorded videos of rolling microbeads were captured and analyzed using ImageJ similarly to prior publications *(223, 224)*.

5.4 RESULTS

Mouse E-selectin homology model exhibits a greater interdomain angle than human E-selectin

Human and mouse E-selectin structures were solvated and equilibrated over the course of 10-ns MD simulations. Three simulations were performed for each species; the average structures for each species over the MD simulations were examined and compared. The most prominent structural difference between the two species was the interdomain angle between the EGF and lectin geometric centers. The mean interdomain angle for hu- man E-selectin was 93.8° and the mean for mouse E- selectin was 104.8°, a difference of 11°.

Figure 5.2a shows overlaid representative human and mouse structures, and Figure 5.2b shows the interdomain angle quantification.

Figure 5.3 shows the dynamic secondary structure by residue of each simulation run. The lectin domain for each species contains two α-helices: the C-terminal end of the first α-helix is shorter by one or two residues for mouse E-selectin, and both species show some fluctuation, known as "fraying" *(225)*, in the length of the second α-helix, particularly on the C-terminal end. The β- strands in the remainder of the lectin domain vary in length for both species. In the EGF domain, the main structural features are two antiparallel β-strands. For the human runs 1 and 2, the beta-strands show little change in their length. In the human run 3, the two β-strands became fragmented into three after 2 ns. For the mouse, the β-strands show some variation in length for runs 1 and 2 but remain mostly stable for run 3. Overall, the mouse E-selectin lectin and EGF domains contains more random coil and turns than human E-selectin.

Looking more specifically at the residue differences be- tween species, the average backbone root mean square deviation (RMSD) by residue was compared (Figure 5.4a). Mouse E-selectin exhibited a greater backbone RMSD across nearly all residues. Specifically, the regions 1–3, 6–8, 21–25, 41–42, 64–66, 79–87, 96–100, 118–121, 124–126, 139, 145–151, and 153–157 showed a difference of more than 1 Å. Each of these regions contains amino acid differences between species. Importantly, many of these regions are involved with the pivot point between the lectin and EGF domains *(226)*. The flexibility of each residue was compared between species by examining the root mean square fluctuation (RMSF). Figure 5.4b shows the RMSF by residue for each species,

averaged over the three runs. The RMSF by residue was nearly similar between human and mouse, but the mouse shows peaks at residues 21, 43, and 124 whereas the hu- man protein does not. As expected, these are all locations where there are one or more amino acid differences between species and all are locations of in- creased backbone RMSD (see Figure 5.4a). Residue 21 and 43 are at the C-terminal end of the first and second α-helices, respectively. As shown in Fig. 2, the length of both α-helices fluctuated over the equilibration MD simulation. Residue 124 shows the greatest increase in RMSF and is located in a section of turns and coils in the EGF domain that is roughly parallel to the main β- strands. Figure 5.4c shows the locations of two residues where there was the greatest difference in RSMD for the mouse E-selectin. Residue 22 is located very close to the lectin/EGF domain interface, and residue 85 is close the binding pocket in the lectin domain.

Mouse E-selectin is predicted to bind more strongly to sLe^X than human E-selectin Equilibrated sLe^X was then docked onto the human and mouse E-selectin structures. The free energy of binding and the dissociation constant were ranked for each of the resulting complexes. Only stable complexes for which there was interaction with the calcium ion were considered *(227)*, resulting in four feasible complexes for each species, and the highest free energy complex of each species was chosen for further study *(228)*. The mouse E- selectin complex yielded a higher free energy of binding as well as a lower dissociation constant (Figure 5.5).

Differences in dissociation time among complexes are caused more by interdomain flexibility rather than by contacts between receptor and ligand.

The complexes were solvated and equilibrated for 10 ns. The average equilibrated complexes were examined prior to dissociation as per other studies of selectin binding *(229, 230)*. The geometric parameters analyzed included the distance and angle between the lectin and EGF domain centers of mass, the number of interdomain contacts and hydrogen bonds, the hinge distance, and the number of contacts and hydrogen bonds between the ligand and the receptor. Contacts were de- fined as less than 5 Å distance between two residues. As shown in Fig. 6a, the mean interdomain angle for the mouse-sLe^X complex was higher than for the human- sLe^X complex. Increased interdomain angle has been shown to increase flow-enhanced tether rate for N138G L-selectin *(231)*, so it is predicted that mouse E-selectin will have a greater tether rate than human E-selectin. The secondary structure composition of both E-selectin species was examined (Figure 5.6b). There was no significant difference in the percentage of α-helices and coil between species. However, mouse E-selectin in complex had a smaller percentage of β-strands and an increased percentage of turns compared with human E-selectin.

The secondary structure of each complex was examined over the solvated free dynamics simulation (Figure 5.7). There was a notable difference in the antiparallel β- strands of the EGF domain between species. The mouse

complex showed two such β-strands during each individual run and the length between the strands varied. However, all of the human complex runs oscillated be- tween two or three short β-strands. For both species, the two α-helices in the lectin domain showed some fluctuation in the length, particularly on the C-terminal end of the second α-helix; this is similar to the trajectories of E-selectin alone (Figure 5.2). The residue flexibility

of each species complex was examined by studying average RMSF values over the 10-ns free dynamics (Figure 5.8a). Comparing the two species, the mouse complex exhibited a higher RMSF at several key pivot residues, including 2, 30, and 125 (Figure 5.8b). There is also an RMSF peak at residue 43, which is at the C- terminal end of the second α-helix. Adhesion is largely regulated by the interdomain hinge, so increased flexibility in this area could indicate a prolonged bond lifespan and lower off-rate *(218)*.

The E-selectin residues in contact with sLe^X were examined for the average solvated 1G1T structure and human and mouse configuration complexes (Figure 5.9). The human complex exhibited more contacts with sLe^X, defined as the number of atoms of E-selectin that were within 5 Å of any atoms of sLe^X. (Figure 5.9a). The specific residues and number of contacts for each complex are shown in Figure 5.9b. All of the E-selectin residues except residue 99 had RMSF values within 1 Å (Figure 5.8a), indicating relatively low flexibility. This is consistent with their location within or near the binding site. Residue 82 had the most contacts, with residues 97, 105, 107, and 111 showing the next highest number of contacts. There were several contacting residues in the human complexes that had no or negligible contact for the mouse complexes, including 47, 48, 77, 78, 79, and 100. All of these residues had fewer than 50 contacts among the three runs. Conversely, two residues for which there was significantly more contact for mouse complexes than for human were 99 and 108 (Figure 5.9c). Both residues 99 and 108 experienced about 100 contacts between the three mouse complexes; they are located on either end of the sLex and may serve as anchor points. Thus, despite having fewer total contacts and a similar number of resi- dues in contact with sLe^X, the data suggest that

residues 99 and 108 are of particular importance in dissociation. Residue 99 is lysine and residue 108 is arginine, both large and positively-charged amino acids. Neither of these are residues that are different between human and mouse E- selectin but both are one or two residues away from substitutions at 98, 101, and 110.

Mouse E-selectin complex takes longer to dissociate than human E-selectin Each species complex was subjected to force loading rates between 2000 and 5000 pm/ps^2, and dissociation was determined as the point when all hydrogen bonds between the ligand and receptor were broken and did not reform. In all simulations, higher force-induced loading rates led to faster dissociation times (Figure 5.10). Under all force-induced loading rates, mouse complexes took longer on average to dissociate. However, only the rate of 3000 pm/ps^2 led to a statistically significant dif- ference between species. sLe^x-coated microspheres were perfused through E- selectin coated microtubes and the average rolling vel- ocity of the microspheres on each E-selectin species were compared (Figure 5.11). Microspheres were used in- stead of cells to eliminate effects of cell deformability or other selectin:ligand pairs not considered within the scope of this study. As expected, the microspheres roll- ing on mouse E-selectin showed a statistically significantly lower rolling velocity compared to microspheres perfused over human E-selectin; the average rolling vel- ocity on human E-selectin was 11.2 μm/s and the aver-age for mouse E-selectin was 0.63 μm/s. Rolling velocity is largely affected by off-rate *(232)*, so the longer dissociation exhibited by simulations of the mouse E-selectin complex versus the human complex (Figure 5.0) is consistent with this trend.

5.5 DISCUSSION

Excessive leukocyte extravasation out of the blood- stream has been linked with chronic inflammation *(216)*. Thus, potential therapies for controlling the inflammatory response could involve inhibiting or moderating the selectin adhesion that mediates leukocyte tethering and rolling to the blood vessel walls. Homology model- ing and amino acid substitutions, particularly those that affect molecular flexibility, and have been shown to be highly effective in changing adhesion and inhibitive function *(233–235)*. In this study, a mouse homology model comprising 29 point substitutions to the human E-selectin crystal structure greatly affected dissociation of sLe^X from the resulting complex. The adhesive characteristics of the mouse E-selectin homology model qualitatively match results from experiments that showed slower rolling velocity of sLe^X-coated microspheres. These results provide new insight into the connection be- tween structure and function of species-specific E-selectin. These results suggest that differences in dissociation time result more from interdomain flexibility than by contacts between receptor and ligand. Docking a homology model structure does accumulate more errors than using a crystal structure *(236)*, but in this case, a crystal structure for mouse E-selectin was not available. The docking algorithm accounts for two import- ant details: protein flexibility is a key determinant in binding, and physiologically, complexes are solvated in a salt solution *(227)*. The docking algorithm included flexibility in the E-selectin side chains and full flexibility in the sLe^X.

The docked structures were solvated after docking using 10-ns MD simulations to allow for more physiological conditions. Intramolecular distortion of the lectin and EGF

domains was not evident for most simulations, particularly at higher force-induced loading rates. It has been shown that shear flow can have a contribution to intramolecular distortion *(230)*, but as with most selectin:ligand dissociation simulations *(136)*, shear flow is not directly considered in these SMD simulations.

This study demonstrates the significance of combining simulations with experimental rolling studies to gain in- sights into the functional differences between proteins that share sequence similarity. The differences in amino acid structure can be exploited for applications such as selectin-based leukocyte and circulation tumor cell isolation *(176)*. The combined methodology involving docking,

5.6 CONCLUSION

Molecular simulations were used to elucidate the binding of sLe^X to mouse and human E-selectin. Docking simulations predicted that mouse E-selectin would bind more strongly to sLe^X than human E-selectin, and SMD simulations predicted that the mouse E-selectin:sLe^X complex would exhibit a longer dissociation time. Mouse E-selectin alone and bound to sLe^X exhibited a greater interdomain angle than human E-selectin, and there were fewer receptor:ligand contacts. When tested experimentally, sLe^X-coated microspheres rolled more slowly in tubes coated with mouse E-selectin rather than human E-selectin.

Figure 5.1: Sequence alignment of EGF and lectin domains of human and mouse E-selectin. The lectin domain is shown in green, and the EGF domain is shown in teal. Residue differences between species are noted in red, and the binding pocket for human E-selectin is noted in yellow and underlined. Adapted from A. Rocheleau, T. Cao et al. BMC Structural Biology (2016).

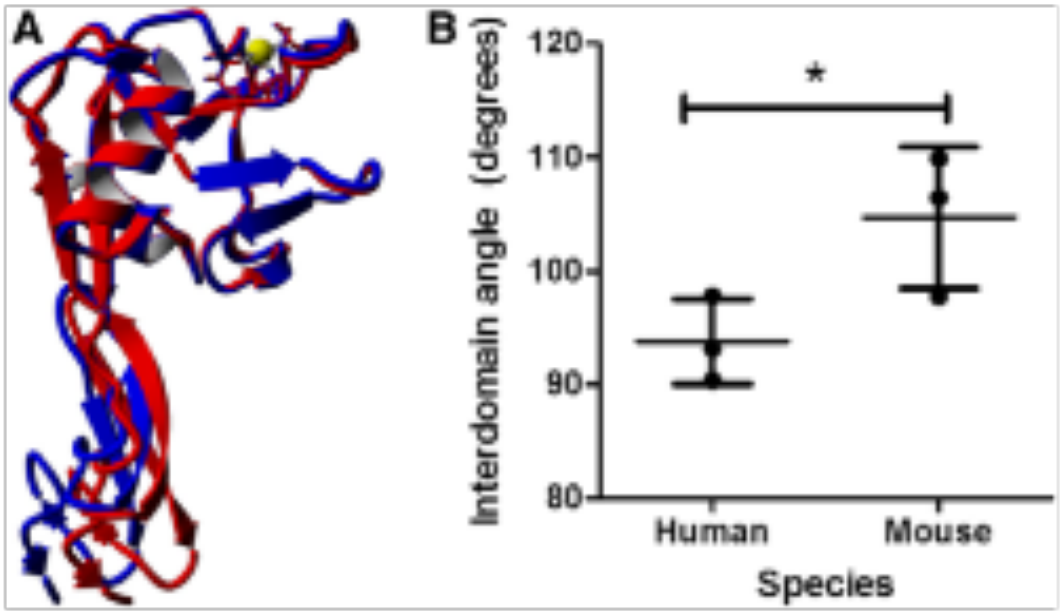

*Figure 5.2: Mouse E-selectin showed a greater interdomain angle than human. a Mouse E-selectin is shown in blue and human E-selectin is shown in red. b The angle is measured from geometric center of residues 1–118 to the geometric center of residues 119–157 with a hinge at the pivot. Mean and standard deviation are plotted. Calcium ion is shown in yellow. *P value < 0.05 (two-tailed t-test). Adapted from A. Rocheleau, T. Cao et al. BMC Structural Biology (2016).*

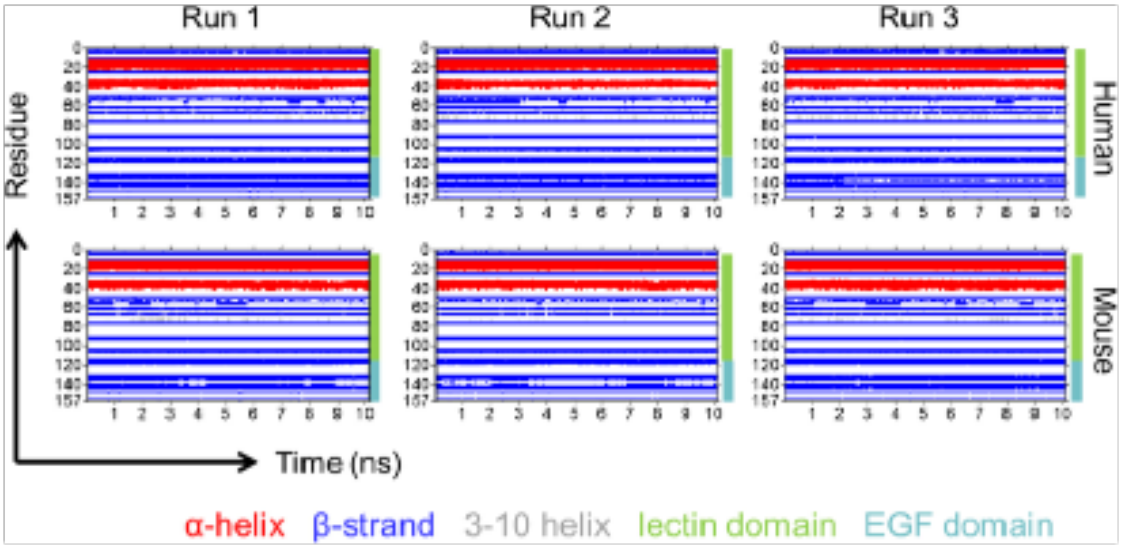

Figure 5.3: Dynamic secondary structure by residue of human and mouse E-selectin over 10 ns MD simulations. Residues are labeled by secondary structure according to their color: α-helices are red, β-strands are blue, 3–10 helices are grey, and coils and turns are not colored. The lectin domain includes residues 1–118, and the EGF domain is 119–157. Adapted from A. Rocheleau, T. Cao et al. BMC Structural Biology (2016).

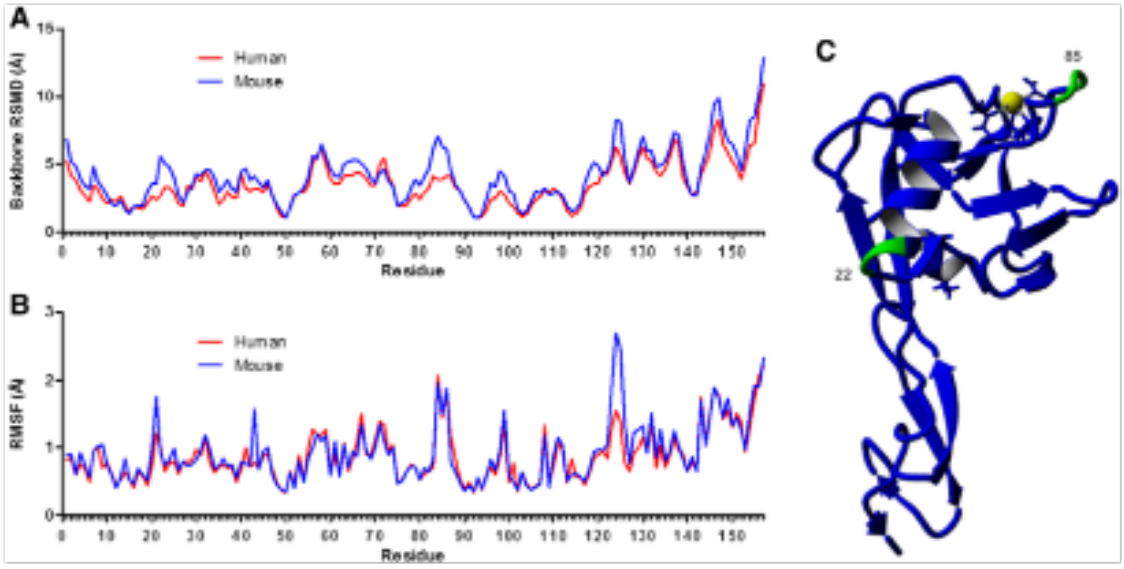

Figure 5.4: Residue differences between human and mouse E-selectin. Average backbone RMSD by residue (a) and average RMSF by residue (b)of human and mouse E-selectin during 10 ns MD simulations. c Mouse structure showing locations of residues 22 near the domain interface and 85 near the binding pocket. Adapted from A. Rocheleau, T. Cao et al. BMC Structural Biology (2016).

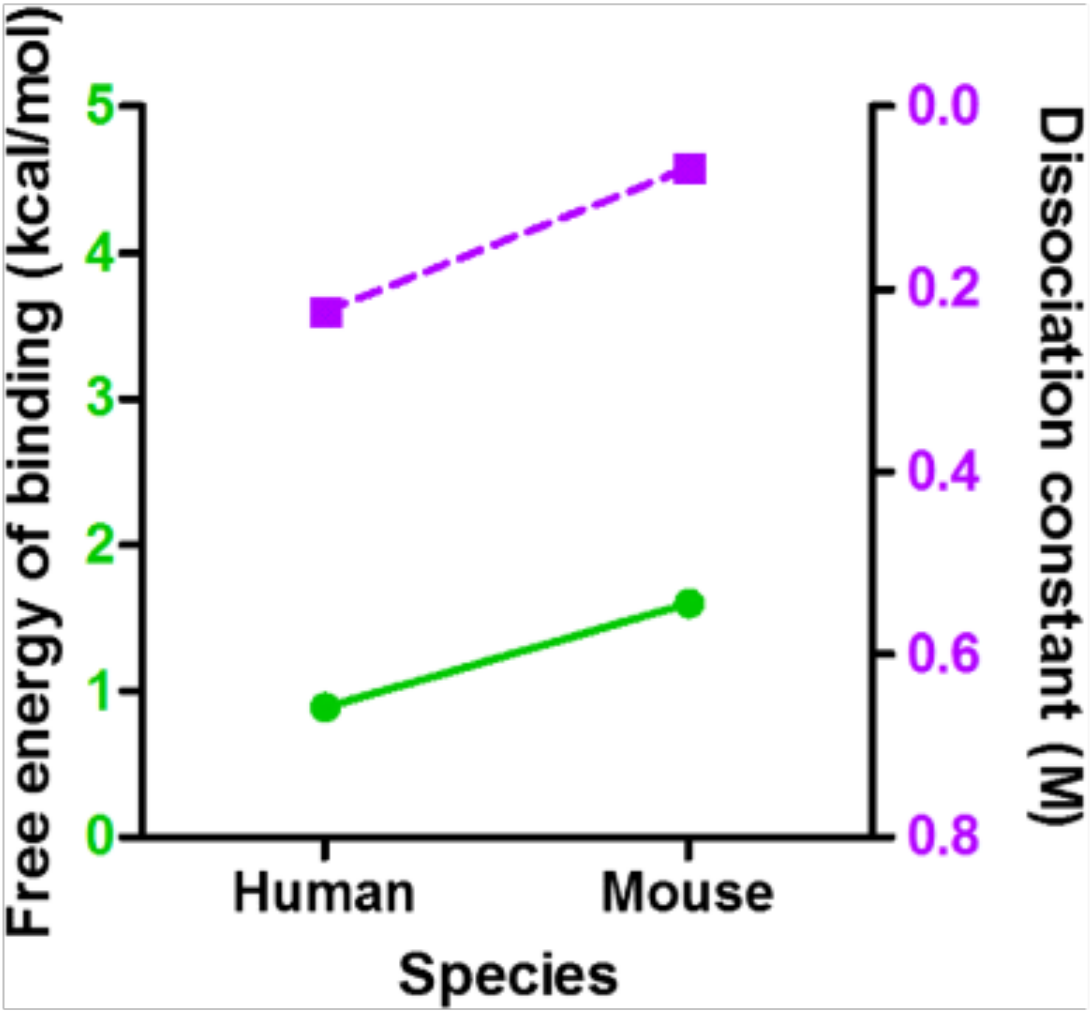

Figure 5.5: Free energies of binding and dissociation constants for human and mouse E-selectin:sLex complexes. Free energies of binding are shown with green circles and a solid line and dissociation constants are shown with purple squares and a dashed line. Adapted from A. Rocheleau, T. Cao et al. BMC Structural Biology (2016).

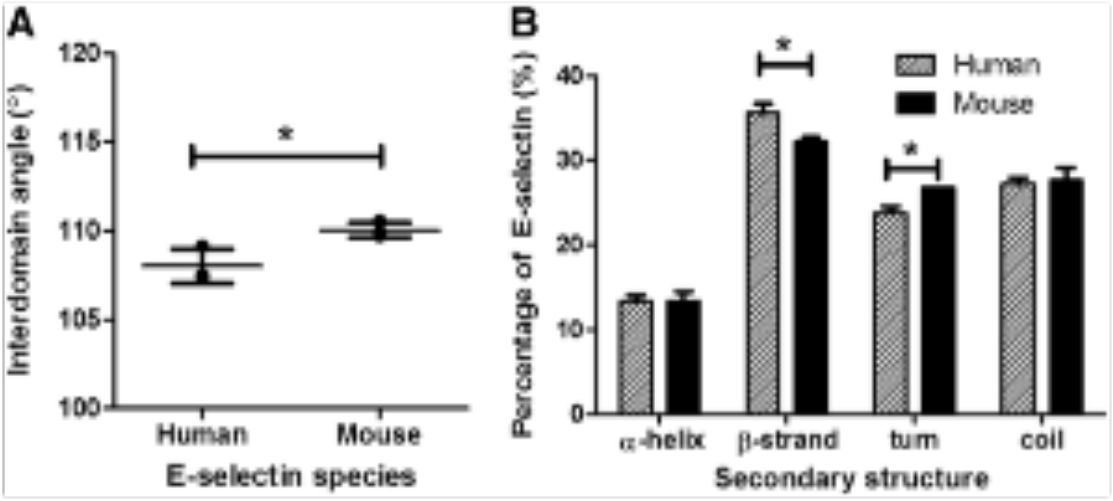

*Figure 5.6: Differences in domain angle and secondary structure composition between species. a Angle between geometric center of residues 1–118 and geometric center of residues 119–157 for human and mouse complex configurations. b Secondary structure composition of E-selectin by species. Mean and standard deviation are shown. *P < 0.05 (two-tailed t-test). Adapted from A. Rocheleau, T. Cao et al. BMC Structural Biology (2016).*

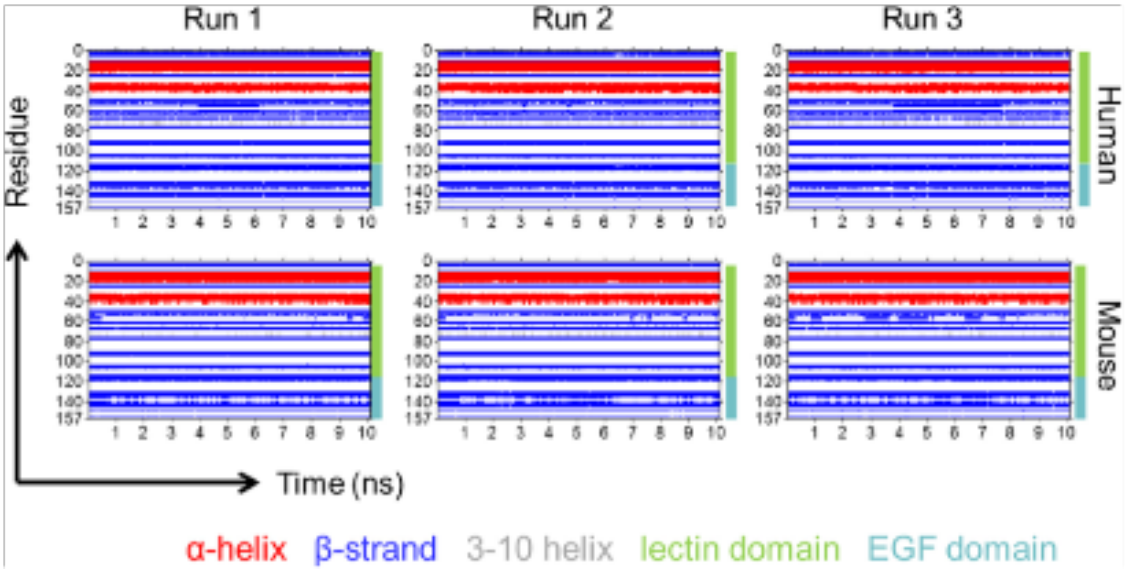

Figure 5.7: Dynamic secondary structure by residue of human and mouse E-selectin complexes over 10 ns MD simulations. Residues are labeled by secondary structure according to their color: α-helices are red, β-strands are blue, 3–10 helices are grey, and coils and turns are not colored. The lectin domain includes residues 1–118, and the EGF domain is 119–157. Adapted from A. Rocheleau, T. Cao et al. BMC Structural Biology (2016).

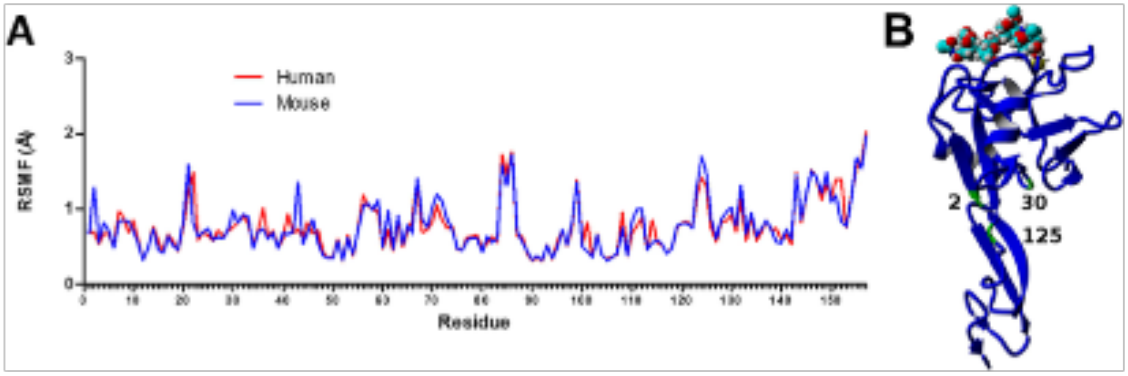

Figure 5.8: Interdomain hinge differences between species. a RMSF by residue for human mouse configuration complexes. b Mouse structure showing locations of residues 2, 30, and 125 near the domain interface. Adapted from A. Rocheleau, T. Cao et al. BMC Structural Biology (2016).

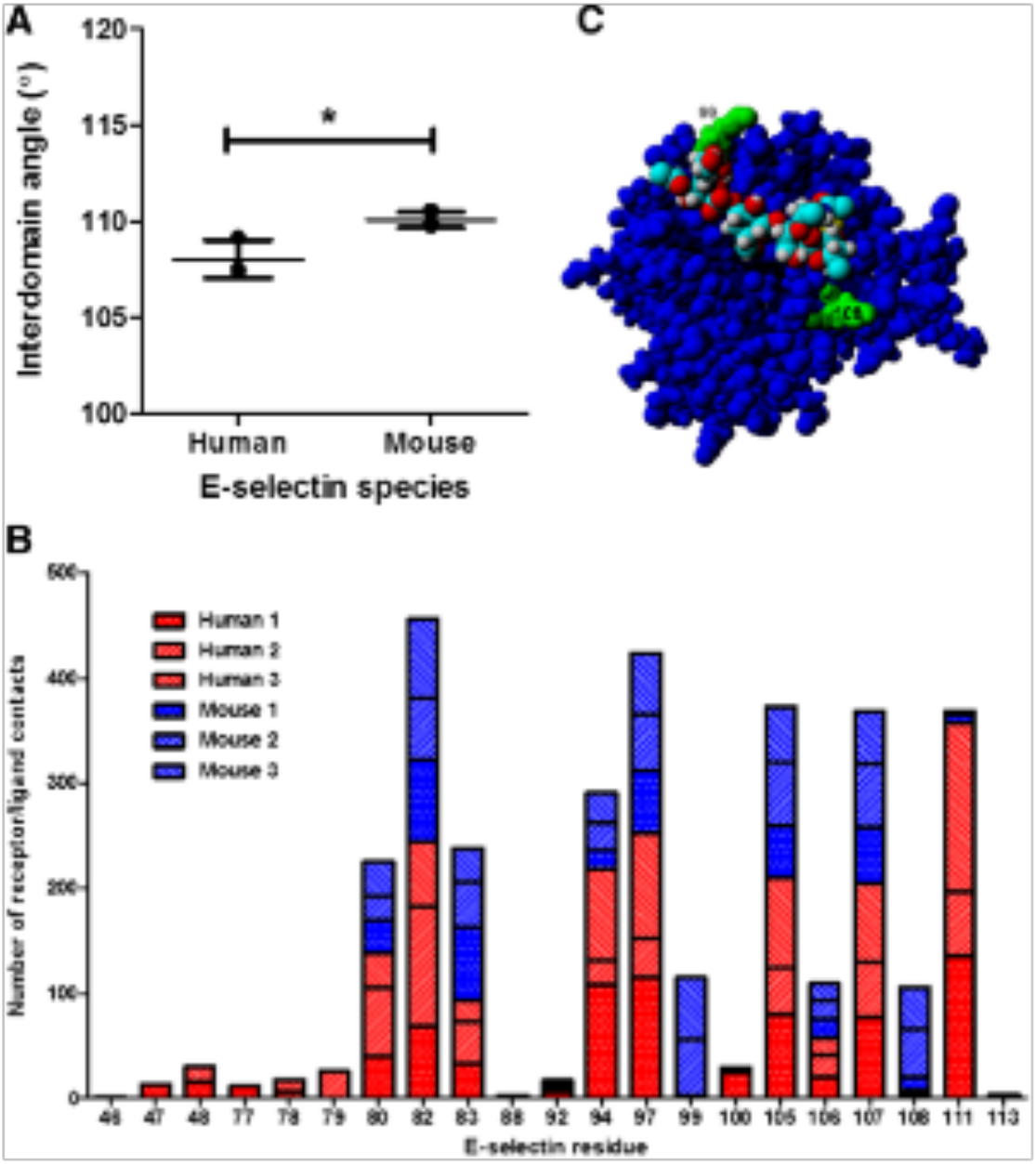

*Figure 5.9: Receptor/ligand interface differences between human and mouse complexes. a Number of contacts between ligand and receptor within 5 Å. Mean and standard deviation are shown. *P < 0.05 (two-tailed t-test). b Distribution and quantification of receptor/ligand contacts for E-selectin residues that are within 5 Å of sLex for each human and mouse complex. c Mouse E-selectin looking down on lectin domain, showing*

locations of residues 99 and 108 relative to sLex. Adapted from A. Rocheleau, T. Cao et al. BMC Structural Biology (2016).

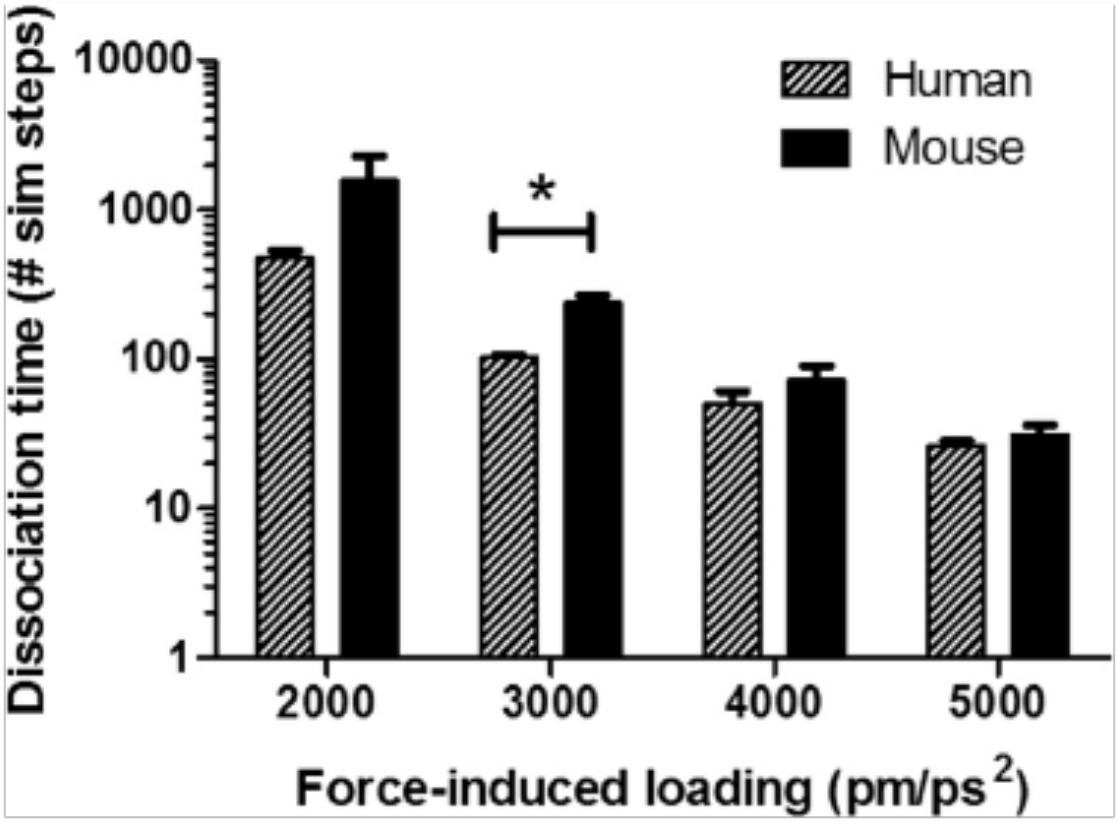

*Figure 5.10: Dissociation time for mouse:sLex and human:sLex complexes at varying force-induced loading rates. Mean and standard deviation are shown. *P < 0.05 (two-tailed t-test). Adapted from A. Rocheleau, T. Cao et al. BMC Structural Biology (2016).*

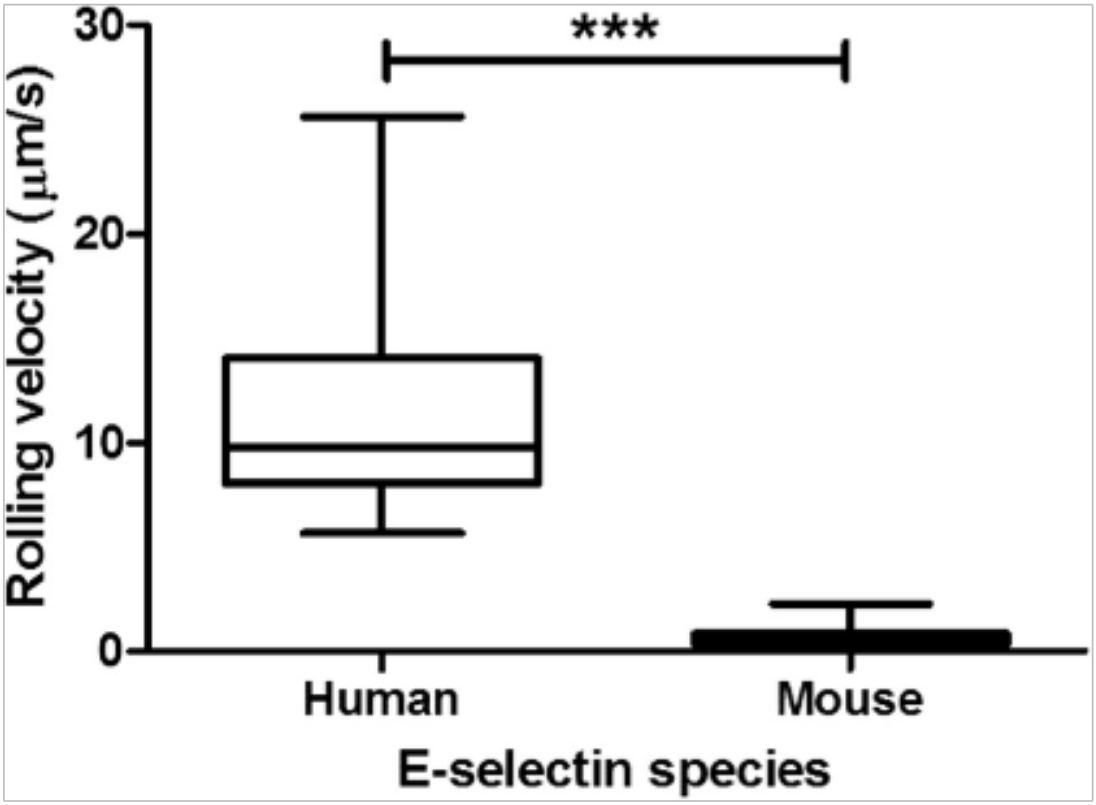

*Figure 5.11: Rolling velocity of sLex-coated microspheres perfused through an E-selectin coated microtube. Mean and standard deviation shown. ***P < 0.001 (two-tailed t-test). Adapted from A. Rocheleau, T. Cao et al. BMC Structural Biology (2016).*

CHAPTER 6

Stabilization of the Hinge Region of Human E-selectin Enhances Binding Affinity to Ligands Under Force

This chapter is in submission in *the Scientific Report.*

6.1 ABSTRACT

E-selectin is a member of the selectin family of cell adhesion molecules expressed on the plasma membrane of inflamed endothelium and facilitates initial leukocyte tethering and subsequent cell rolling during the early stages of the inflammatory response via binding to glycoproteins expressing sialyl Lewis^X and sialyl Lewis^A (sLe$^{X/A}$). Existing crystal structures of the extracellular lectin/EGF-like domain of E-selectin complexed with sLe^X have revealed that E-selectin can exist in two conformation states, a low affinity (bent) conformation, and a high affinity (extended) conformation. The differentiating characteristic of the two conformations is the interdomain angle between the lectin and the EGF-like domain. Using molecular dynamics (MD) simulations we observed that in the absence of tensile force E-selectin undergoes spontaneous switching between the two conformational states at equilibrium. A single amino acid substitution at residue 2 (serine to tyrosine) on the lectin domain favors the extended conformation. Steered molecular dynamics (SMD) simulations of E-selectin and PSGL-1 in conjunction with experimental cell adhesion assays show a longer binding lifetime of E-selectin (S2Y) to PSGL-1 compared to wildtype protein. The findings in this study advance our understanding into how the structural makeup of E-selectin allosterically influences its adhesive dynamics.

6.2 INTRODUCTION

E-selectin belongs to a family of cell adhesion (E-, L-, and P-) molecules that are responsible for leukocyte recruitment to inflammation sites *(237)*. E-selectin is a Ca^{2+}-dependent lectin glycoprotein that is expressed on the plasma membrane of activated vascular endothelial cells by pro-inflammatory stimuli *(149)*. Beyond its well-characterized role in leukocyte trafficking, E-selectin is also involved in integrin activation, hematopoietic stem cell homing to the bone marrow, and cancer metastasis *(68, 145, 238–241)*. All selectins have a C-type lectin domain at the extracellular N-terminus containing a binding pocket that recognizes glycoproteins and glycolipids decorated with tetrasaccharide sialyl $Lewis^X$ and sialyl $Lewis^A$ ($sLe^{X/A}$) *(242)*. Known E-selectin's ligands include P-selectin glycoprotein ligand-1 (PSGL1), CD43 and CD44 expressed on various human leukocyte subpopulations, and E-selectin ligand-1 (ESL-1) present on mouse myeloid cells *(243–245)*. Connecting to the lectin domain is an epidermal-growth-factor (EGF-like) domain, followed by varying units of short consensus repeats (SCRs), a transmembrane portion and ending with a cytoplasmic tail *(149)*. Structural studies of selectins suggest that the molecules can exist in two conformational states: a low affinity (bent) conformation and a high affinity (extended) conformation *(159, 246–248)*. The defining characteristic differentiating the two conformational states is the interdomain angle of the hinge region, the interdomain region connecting the lectin to the EGF-like domain. The hinge region of selectin is of the focus in this study because of its allosteric modulation of selectin binding mechanics *(249, 250)*. Here we show a single amino acid substitution at the hinge region can alter

the overall macromolecular characteristics of E-selectin resulting in altered binding kinetics to ligands. The data supporting this observation will be discussed in this article.

Effective leukocyte trafficking in the vascular microenvironment under physiological shear flow requires that selectins are able to bind to ligands very quickly by having a fast on-rate. In addition, the subsequent selectin/ligand complex must able to withstand the pressure of the tensile stress. Selectin binding exhibits what is known as "catch-bond" behavior in which receptor/ligand bond formation requires a minimum threshold level of shear *(251–253)*. The bond is further strengthened as the tensile force increases until the force becomes too great, and the bond becomes an ordinary "slip-bond". Previous studies have put forth multiple models linking the structural architecture of selectin's conformational states to their catch-bond behaviors. For instance, in the "sliding-rebinding" model described by Lou et al., it is postulated that the flexibility of the hinge region in L-selectin allows it to adopt two different conformations: a low affinity (bent) conformation in the absence of force and a high affinity (extended) conformation in the presence of force *(218, 254)*. In the extended conformation, the binding surface is aligned with the direction of the force which allows bound ligands to slide along the binding interface and continuously rebuild or form new interactions, causing a high affinity conformation. Selectin crystal structures also revealed significant structural displacement at the binding interface when the molecule adopts different conformational states, which suggests an allosteric relationship between the hinge region and the binding interface *(255)*. However, the "sliding-rebinding" model does not address this allosteric relationship. Alternative theories have been proposed linking the force-induced extension of selectin molecules and allosteric changes in the ligand

binding interface *(226, 255)*. In the "prybar" model, residue 1W of the lectin domain and the EGF-like domain of L-selectin together form an L-shaped lever that is held together by a network of hydrogen bonds when the molecule is in the bent conformation. When force is applied and L-selectin transitions to the extended conformation, the lever dislodges the relatively large and hydrophobic residue, 1W, which causes a cascade of residue displacements resulting in the allosteric change of the binding interface to a high-affinity conformation.

In different species, the same selectin molecules share a high degree of amino acid sequence homology: ~72% and ~60% of amino acid sequence are conserved for the lectin and EGF-like domain, respectively *(149)*. The high degree of inter-species sequence homology enables mouse E-selectin to readily cross-react to human ligands and vice-versa *(213, 256)*. More interestingly, mouse E-selectin exhibits significantly higher affinity to human ligands than human E-selectin. This observation can be explained in part by molecular dynamics (MD) simulations that found mouse E-selectin to have a greater interdomain angle than its human counterpart, suggesting that mouse E-selectin favors the high-affinity extended conformation *(213)*. However, individual amino acid variances of E-selectin between human and mouse species and their influence on ligand binding kinetics remain largely unexplored. The goal of this study was to gain new insight into E-selectin conformational states, their corresponding ligand binding characteristics, and how strategic structural modifications of E-selectin can modulate its macromolecular behavior. Using MD simulations, we predicted possible E-selectin structural transitions between conformational states and their effects on the binding interface. We also looked at the network of non-covalent interactions

distributed over the hinge region associated with these conformational changes. Next, we introduced a key point mutation at the hinge region and examined the dynamic changes over time on E-selectin/PSGL-1 complex in the presence of a pulling force that was applied to induce unbinding. In conjunction with computational modelling, experimental cell rolling assays were used to substantiate our MD results.

6.3 METHODS

Molecular Dynamics (MD) Simulation

The bent and extended crystal structures of E-selectin (1G1T, 4CSY *(159, 247)*), were obtained from the Protein Data Bank for use as starting atomic coordinates. Free-dynamics and steered molecular dynamics (SMD) simulations were performed using the YASARA (http://yasara. org) package of MD programs with the YAMBER3 self-parameterizing force field. For all simulations, the temperature and pressure were held constant at 300 K and 1 atm, respectively. Periodic boundary conditions, the particle mesh Ewald method for electrostatic interactions, and the recommended 7.86 A$^{\circ}$ force cutoff for long-range interactions were also used. Predicted structures of PSGL-1 bound to E-selectin were obtained by aligning E-selectin (1G1T, 4CSY) crystal structures on the P-selectin/PSGL-1 complex (1G1S, subunit a) via the MUSTANG algorithm. All simulations were run at least 4 times with different starting velocities.

Principle Component Analysis (PCA) of MD simulations was performed with Bio3D, and R software packaged developed by the Grant lab *(264)*. Cartoon renditions of E-selectin was created with UCSF Chimera, an extensible molecular modelling system,

developed by the UCSF Resource for Biocomputing, Visualization, and Informatics *(265)*.

Cell lines and cell culture

The acute myeloid leukemic KG-1a cell line (ATCC number CCL-264.1) was purchased from ATCC (Manassas, VA) and cultured in RPMI 1640 media supplemented with 2 mM L-glutamine, 25 mM HEPES, 10% (v/v) FBS, and 100 U/mL penicillin-streptomycin at 37C and 5% CO_2. Cultured cells were regularly test for mycoplasma using Universal Mycoplasma Detection Kit (ATCC 30-1012K).

Microtube functionalization

The microtubes were functionalized using methods, as previously described *(61, 168)*. Briefly, micro-renathane (MRE) tubes (300 mm i.d.; Braintree Scientific, Braintree, MA) were sterilized with 75% ethanol for 15 min. After three washes with phosphate buffer saline (PBS) (Ca^{2+} and Mn^{2+} free), the microtubes were incubated with Protein G (2 μg/mL PBS) for 1 h. Next, the luminal surface was functionalized with chimeric human E-selectin (W/T, S2Y, S2W, S2C) at 5 μg/mL for 2 h. The microtubes were then incubated with dry milk powder (5% w/v) in PBS for 1 h to minimize nonspecific adhesion. For control experiments, microtubes were prepared as indicated above except that the adhesion molecule was replaced with bovine serum albumin (BSA).

Cell adhesion assay

Cell rolling experiments were conducted using methods as previously described *(136)*. KG-1a cells were suspended in flow buffer (PBS supplemented with 2 mmol Ca^{2+}) at the concentration of 10^6 cells/mL. Cell suspension was perfused through functionalized microtubes using a syringe pump at specified wall shear stresses. Videos were recorded for 1 min at 5-10 random locations along the length of the microtube after 5 min of perfusion for each shear stress.

Data acquisition

Rolling cells were recorded using a microscope-linked Hitachi CCD camera KP-M1AN (Hitachi, Japan) and a Sony DVD Recorder DVO- 1000MD (San Diego, CA). Rolling velocity was determined using ImageJ (U.S. National Institutes of Health, Bethesda, MD). Rolling cells were defined as a cell translating along the surface for >2 s at a velocity <50% of the free stream velocity of a noninteracting cell. The average rolling velocity was calculated from at least 30 rolling cells. Cell rolling experiment was done in triplicates for statistical analysis. Two-tailed unpaired t-tests were used to analyze result

6.4 RESULTS

E-selectin spontaneously transitions between the bent and extended conformations at equilibrium

Existing structural data suggest that selectins adopt two conformational states: a low affinity (bent), and a high affinity (extended) conformation. Furthermore, MD simulations predicted that L-selectin can undergo conformation switching in the

absence of force *(172)*. To determine if E-selectin exhibits spontaneous conformational change between the two conformational states in the absence of force, we simulated the molecule, as previously described *(136)*, using the published crystal structures of the two known conformational states (bent - 1G1T, extended - 4CSY) as starting coordinates. Principal component analysis (PCA), a dimensionality reduction technique *(257, 258)*, was used to transform the original high-dimensional representation of protein motion in MD simulations into a lower dimension representation that reveals the dominant structural dynamics of proteins. The vibrational fluctuation of the molecules over a period of 50 ns of simulation time was reduced to two Principal Components (PC 1, PC 2), which attributed for over 78% of total protein movement (Figure 6.7). The greatest fluctuation was observed in the EGF-like domain (residues 129-) (Figure 6.1a). In addition, the two domains moved in opposite directions of one another. In the lectin domain, the flexible region adjacent to the hinge region, and the flexible loop (residues 83-89) at the binding pocket also showed a high degree of fluctuation (Figure 6.1a). Tracing the trajectory of the structural displacement of the simulation of 4CSY (extended) we observed that the molecule spontaneously transitioned from the bent to extended conformation and back (Figure 6.1b). RMSD traces of the simulations of either 4CSY (extended conformation) or 1G1T (bent conformation) showed conformational changes occurring at 10 and 20 ns, respectively (Figure 6.1c). These conformational changes correlated with the opening and closing of the hinge region as indicated by the opening and closing of the interdomain angle (Figure 6.1d).

A dynamic network of hydrogen bonds at the interdomain hinge region stabilizes the conformational states

A closer examination of the flexible interdomain hinge region during the oscillation between the bent and extended conformational states, revealed a dynamic hydrogen bond network. Figure 6.2 shows three representative simulation time points of a MD simulation of E-selectin transitioning from a bent to an extended conformation and back. Looking directly down the X-axis of E-selectin protein, there existed a network of hydrogen bonds (H-bond) that stabilizes the interdomain region on both sides of the molecule. At time = 0, when the molecule is in the bent conformation and the interdomain angle is at its minimum, residue Q30 of the lectin domain hydrogen bonds with E135 of the EGF-like domain. This stabilizes E-selectin in the bent conformation (Figure 6.2a). Residue E34 formed an H-bond to residue Q30, thus keeping the residue facing in close proximity to residue E135. This further promotes its interaction with residue E135. On the opposite side of the molecule, residue N138 of the EGF-like domain exhibited multiple hydrogen bonds with residues on the lectin domain: residue Y37 and the carboxyl oxygen of residue W1. This network of hydrogen bonds between the lectin and the EGF-like domain collectively maintains E-selectin in a bent conformation.

As E-selectin shifted towards the extended conformation and the interdomain angle became larger (Figure 6.2b), residue E34 shifted to the right and away from Q30 and no longer hydrogen bonded to residue Q30, allowing residue Q30 to rotate upward and away from EGF-like domain. Thus, residue Q30 no longer interacted with residue E135,

which also shifted to the right. As the loop region was moving away, residue W1 swung downward and towards the right which then hydrogen bonded with residue E135 (shifted far to the right) and residue Y37. Most noticeably, residue S2 flipped its orientation towards the front and then formed a hydrogen bond with residue N138. The disproportional distribution of hydrogen bonds present here favors the extended conformation.

At t = 30 ns, E-selectin reverted back to the bent conformation (Figure 6.2c). On the left side of the interdomain region, residue Q30 re-rotated back downward and towards the front, bringing it, again, closer to EGF-like domain. Residue W1 swung upward and to the left.

The dynamic breaking and formation of hydrogen bonds and the amino acid residues involved as E-selectin transitions between conformational states suggest that these amino acids, to varying degrees, influence the macromolecular structure of E-selectin.

A substitution of residue 2 (S2Y) eliminates spontaneous transitioning between the two conformational states.

There exist 20 amino acid differences within the lectin domain between human and mouse E-selectin *(213)*. Of these 20 variations, only residue number 2 (S2) of the lectin domain is located in the hinge domain and is involved in noncovalent interaction with residues in the EGF-like domain as pointed out in Figure 6.2. Serine is a smaller amino acid, and its side chain consisting of a hydroxyl group that can noncovalently react with other molecules. On the mouse E-selectin molecule, the serine residue is replaced with

a much larger tyrosine residue that also has a distal hydroxyl group on its sidechain which can readily form H-bonds with asparagine residues (N138 and N139) on the EGF-like domain (Figure 6.3a). Based on the simulation results suggesting that interactions between residue 2 and other residues on the EGF-like domain favor the extended conformation, we postulated that a S2Y point mutation of the human E-selectin molecule would cause the molecule to favor the high affinity extended conformation over the lower affinity bent conformation. To test this hypothesis, we simulated human E-selectin (S2Y) in the similar fashion to the wildtype counterpart, E-selectin (W/T). The S2Y point mutation effectively abolished any spontaneous transitioning of E-selectin between conformational states, as evident by the RMSD trace and the interdomain angle measurements (Figure 6.3b and c). The E-selectin (S2Y) molecule remained in the high affinity extended conformation throughout the entire simulation.

High affinity extended conformation allosterically forces the binding pocket to also adopt a high-affinity conformation in E-selectin

Conformational changes in the hinge region of selectins can allosterically induce conformational changes to the binding region *(172, 259)*. We compared the structural changes occurring in our simulations between the two E-selectin variants. RMSF trace over the simulation time revealed significantly higher residue fluctuations at the flexible loop containing residues 81-85 for E-selectin (W/T) compared to E-selectin (S2Y) (Figure 6.4a). This flexible loop which is located at the binding pocket and its amino acids are involved in ligand binding *(149)*. For the wildtype E-selectin, the loop alternated between high-affinity and low-affinity conformation which reduced the

overall exposure time these amino acid residues to the bound ligand (Figure 6.4b). Conversely, for simulations involving E-selectin (S2Y), the same flexible loop remained for almost the entire simulation time in the high-conformation state.

E-selectin (S2Y) exhibits higher binding affinity to its ligand than wildtype E-selectin

To test our hypothesis that a single amino acid substitution (serine to tyrosine) at residue 2 of E-selectin would allosterically extend the binding lifetime of E-selectin to PSGL-1, we used steered molecular dynamics (SMD) simulations to manually dissociate PSGL-1 away from E-selectin like previously described *(136, 213)*. Figure 6.5 illustrates the amount of simulation time of a representative simulation necessary before PSGL-1 is completely dissociated from E-selectin (W/T and S2Y), as defined by the distance at which non-covalent intermolecular interactions between the two molecules are no longer observed. The SMD simulation showed that PSGL-1 completely dissociated from E-selectin (W/T) significantly faster than with E-selectin (S2Y) at approximately 70 ps and 95 ps, respectively (Figure 6.5a). Four SMD simulations were performed with different initial velocities for E-selectin (W/T or S2Y)/PSGL-1 complex. The average dissociation times were 52.5 ± 14.3 ps and 71.3 ± 23.5 ps for wildtype E-selectin and E-selectin (S2Y), respectively. The longer binding time between PSGL-1 and E-selectin (S2Y) was likely the result of the flexible loop at the binding pocket remaining in close proximity to PSGL-1, thus allowing residues R84 and Q85 to experience prolonged interactions with the fucose residue on PSGL-1. At 10 ps after the initial pulling of PSGL-1 away from E-selectin, the flexible loop containing residues R84 and Q85 in E-selectin (WT) already starting to fold away from

the binding pocket resulting in residues R84 and Q85 to stop interacting with PSGL-1 (Figure 6.5b, top left panel). Conversely, the same flexible loop in E-selectin (S2Y) was still facing into the binding pocket, allowing residues R84 and Q85 to maintain multiples contacts with the fucose molecule on PSGL-1 (Figure 6.5b, bottom left panel). Furthermore, PSGL-1 also maintained multiple interactions with E-selectin (S2Y) outside of the binding pocket including: residue E107 with the galactose, and serine residues (S45, S47) with the sulfated tyrosine (TYS161) on PSGL-1. These interactions were absent in the simulation involving E-selectin (W/T). At 50 ps, the flexible loop inside the binding pocket of E-selectin (W/T) had completely folded away from PSGL-1, further weakening the interaction between the two molecules (Figure 6.4b, top right panel). This is evident from the increase in dissociation distance rate that followed (Figure 6.5a). Comparing to its wildtype counterpart, the E-selectin (S2Y) still maintained multiple interactions with PSGL-1 in the binding pocket, including residue R84 interacting with one of the oxygen species of the fucose molecule on PSGL-1 (Figure 6.4b, bottom right panel).

To further corroborate the SMD simulation results, we experimentally assessed the effect of the point mutation (S2Y) on E-selectin's ligand affinity. We performed a cell rolling assay using model cell line KG-1a, in microtubes coated with the indicated E-selectin/Fc chimeric molecules and under a range of physiological shear stresses as previously described *(136, 176)*. KG-1a is a leukemic cell line expressing abundant selectin ligands on its surface, and is a commonly used model cell line in rolling assays for studies involving selectin ligand binding mechanics *(61, 195)*. Human E-selectin/Fc chimeric protein was created and purified from HEK 293 cells. Variants of wildtype

including E-selectin (S2Y, S2W, and S2C) were also created and purified to assess the allosteric effect of the hinge on E-selectin binding behavior. The average rolling velocities of KG-1a cells were significantly lower on surfaces coated with E-selectin (S2Y) at all levels of shear stress compared to E-selectin (W/T) (Figure 6.6). This is indicative of E-selectin (S2Y)'s enhanced ligand binding compared to the wildtype. We expected the capability of the tyrosine residue to hydrogen bond to asparagine residues in the EFG-like domain would shift the equilibrium in favor of the high affinity extended conformation. Therefore, we also examined the rolling velocity of KG-1a cells on surfaces coated with E-selectin (S2W). Tryptophan (W) is similar to tyrosine in structure, as it is also a bulky amino acid that has an aromatic ring. However, it cannot hydrogen bond to residues 138 and 139 because it lacks the functional OH group. As a result, the rolling velocity profile of KG-1a was observed to be very similar to that of the wildtype. We also looked at the rolling profile of cells on surfaces coated with E-Selectin (S2C). Cysteine has a similar structure to serine but has a sulfur in place of an oxygen atom at the gamma location. Not surprisingly, the rolling profile of KG-1a on this surface was also similar to that on the wildtype. The experimental data support our theory that a S2Y substitution favors the high affinity extended conformation in E-selectin.

6.5 DISCUSSION

The two-state kinetic model of selectin's catch bond behavior postulates that, in the absence of force, selectins may exist in two interchanging conformational states at equilibrium *(231, 260)*. When tensile force is applied, selectins favor the high affinity,

extended conformation. This theory is supported by structural studies of E- and P-selectin and computational modelling of L-selectin *(159, 218, 246, 247)*. Here, our MD simulation data of E-selectin also predicts that the molecule does indeed follow the two-state model, as observed by the molecule's spontaneous transitioning between the bent and extended conformational states (Figure 6.1). Furthermore, we observed conformational change in 3 out of the 4 simulation runs we performed for each starting coordinate (bent and extended). An observed 75% occurrence rate in our simulations is higher than that seen by Lou et al. (~30%) in their MD simulation of L-selectin. The frequency increase may be explained by the extended simulation time of 50 ns in our simulations, compared to 6 ns in the previous study *(218)*. In a more recent study by Preston et al. using small angle X-ray scattering (SAXS) measurement, they found that in the absence of force, ligand binding to E-selectin alone can allosterically shift the equilibrium to favor the high-affinity, extended conformation *(247)*. This observation is in contrast to earlier assertions that tensile force is required to shift the conformational equilibrium towards the extended conformation *(226)*. More importantly, these seemingly contradicting observations emphasize that while our understanding of selectin mechanochemistry is expanding, it is still incomplete. Although it was not explored in this study, it would be interesting in future studies to use MD techniques such as docking to determine if ligand binding alone can trigger an allosteric structural change from the bent to extended conformation in selectins.

Interaction between the lectin and EGF-like domain of selectins is limited in the number of contacts, as observed in published crystal structures and the results presented here (13, 14, Figure 6.2). The small number of interactions between the two domains

supports the theory that the hinge region of selectins is inherently flexible, suggesting that thermodynamically the molecule can readily transition between conformational states at equilibrium. Moreover, by modulating the degree of flexibility of the hinge region, one may influence the conformational equilibrium of selectin. This idea was previously explored in P-selectin which showed that locking P-selectin in the extended conformation can increase its adhesiveness to ligands under hydrodynamic force *(172)*. In addition, others have introduced an N138G substitution on the EGF domain of L-selectin, and showed that replacing a bulky asparagine residue with a smaller glycine residue, can stabilize the high affinity extended conformation of L-selectin *(172, 218, 226)*. Here we investigated the stabilizing effect of single amino acid substitution at residue 2 (S2Y) on the lectin domain of E-selectin. While human and mouse E-selectin share considerable sequence homology, there exist 20 amino acid variances in the lectin domain that may, to varying degrees, contribute to enhanced affinity seen in mouse E-selectin to human ligands *(213)*. Whereas residue 2 in human E-selectin is serine, mouse E-selectin has a relatively bulkier amino acid tyrosine at residue 2. A serine to tyrosine substitution of human E-selectin led to significant decrease in rolling velocity of KG-1a cells on surface coated with E-selectin across a range of shear stresses, an indication of stronger ligand affinity (Figure 6.6). The bulky aromatic ring of tyrosine forces the amino acid to adopt the most energetically favorable orientation, facing away from the lectin domain and with its distal OH group pointing at residues N138 and N139 *(261)*. In the bent conformation, neither serine nor tyrosine interacts with residues in the EGF domain. However, when E-selectin is in the extended conformation, only the larger tyrosine residue is able to make sidechain hydrogen bonds with residues 138 and 139

on the EGF domain at high frequency. We hypothesized that during one of E-selectin spontaneously transition from bent to extended conformation, the S2Y substitution affords more opportunity of H-bond formation with residues 138 and 139 on the EGF domain. As a result, the conformation equilibrium favors the extended conformation. The absence of conformational change in simulations for E-selectin (S2Y) using the extended conformation as starting coordinates supports this hypothesis (Figure 6.3). Furthermore, SMD simulations of E-selectin/PSGL-1 complex showed extended binding for E-selectin (S2Y) compared to the wildtype. Collectively these results suggest the importance of allosteric dependence of the hinge region on the binding mechanics of selectins. A better understanding of selectin structure and its influence on ligand binding can be applicable to other receptor/ligand complexes that exhibit the similar catch-bond behavior.

It is important to note that we did not observe in our simulations of E-selectin (S2Y) with the bent conformation as starting coordinates the molecule spontaneously transition to the extended conformation and remain so. This was not completely unexpected given the limitations of MD simulations. MD simulation time scale represents only a tiny fraction of the biological time scale. Therefore, extended simulation time covering multiple conformational switching would be necessary to produce a truly comprehensive representation of protein biomechanics at the biological time scales. Ultimately, MD simulation time is limited by computing power. Moreover, current molecular mechanics force fields used by many MD simulations do not fully capture the directional dependence of hydrogen bonds *(262, 263)*. This makes modelling selectins, with their extensive and complex hydrogen networks a continuing challenge.

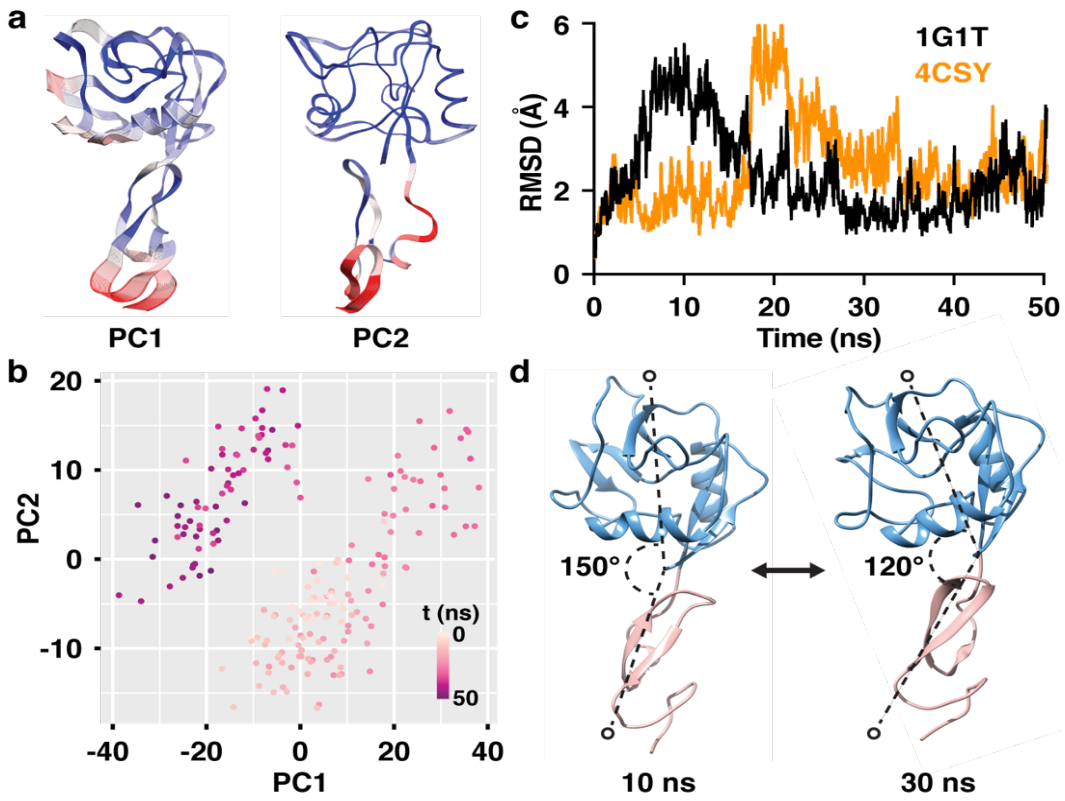

Figure 6.1: E-selectin spontaneously transitions from bent to extended conformational state and back again. (A) MD trajectory representations of E-selectin during the least displacement and the highest displacement, respectively. (B) PC1 vs PC2 shows the predicted transitioning path of E-selectin from bent, to extended, and back to bent. (C) RMSDs of MD simulations as a function of time. (D) Angle measurement of the interdomain hinge region as a function of time. (E) Ribbon representations of E-selectin and the measured angle at t = 10 ns and t = 30 ns. (Blue = lectin domain, Pink = EGF -like domain).

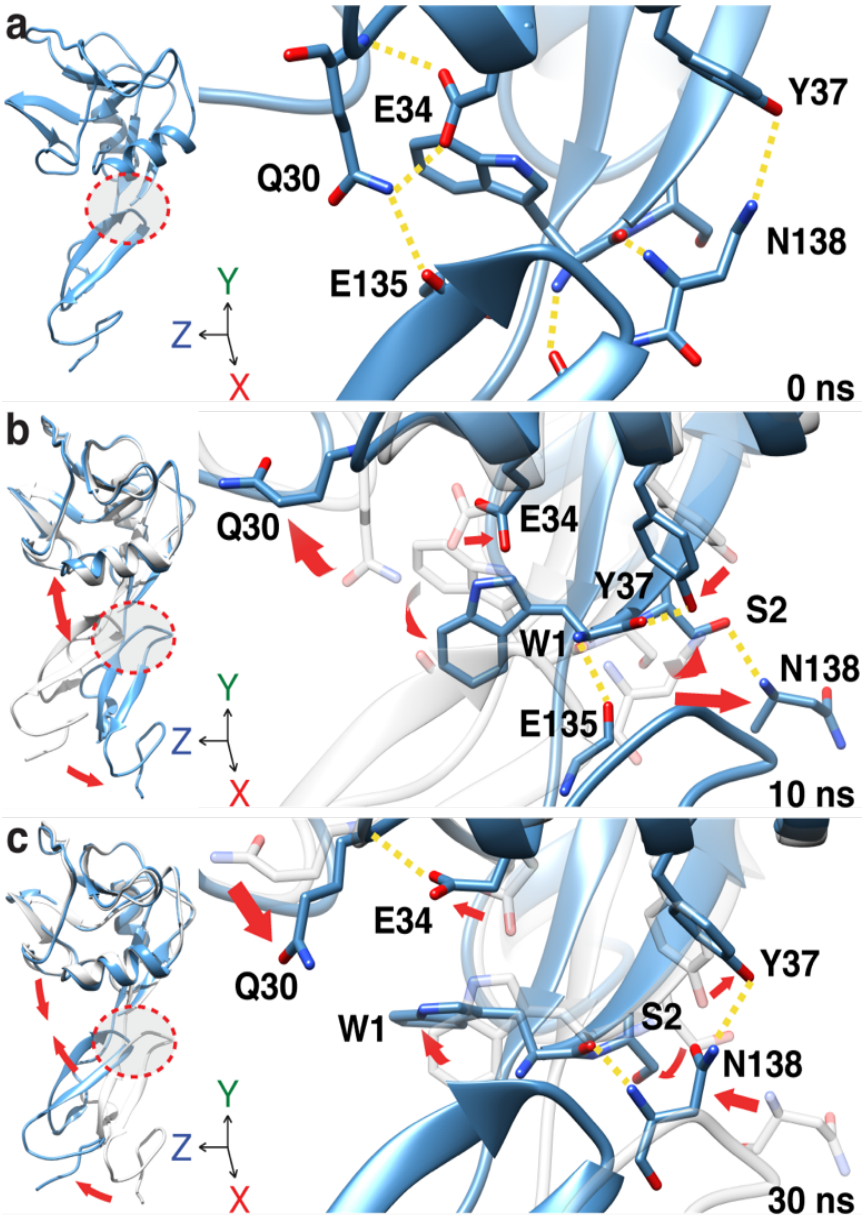

Figure 6.2: Dynamic hydrogen network stabilizes the interdomain hinge region. Representative illustrations of human E-selectin MD simulations at indicated time pointsshowing the formation and breakage of hydrogen bond network as the protein transitions from the bent to the extended conformation and back again at the interdomain region. Yellow dashed lines represent hydrogen bonds; Red arrows indicate trajectories of indicated residues.

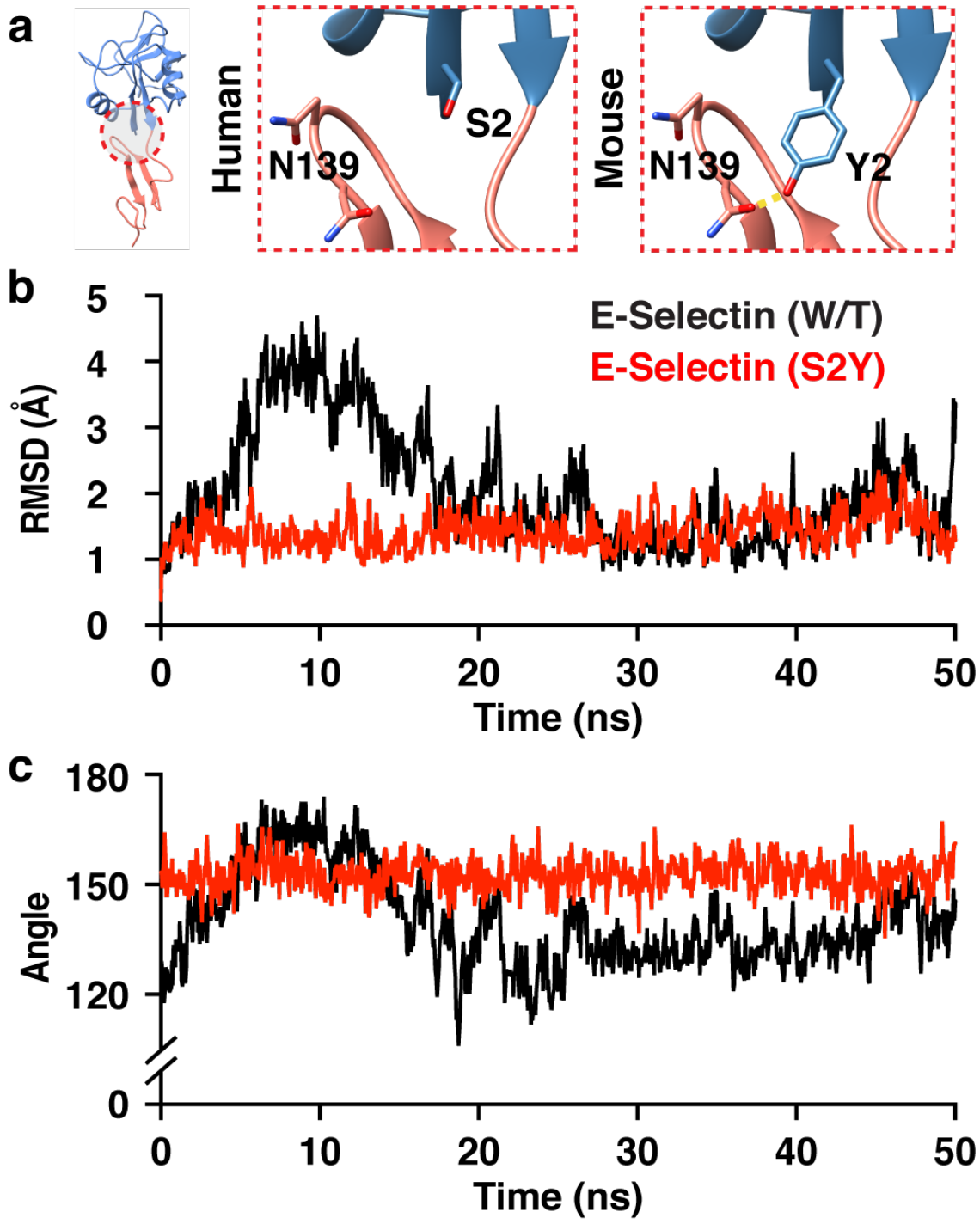

Figure 6.3: Point mutation of residue 2 from Serine to Tyrosine eliminates the spontaneous transition between the two conformational states.

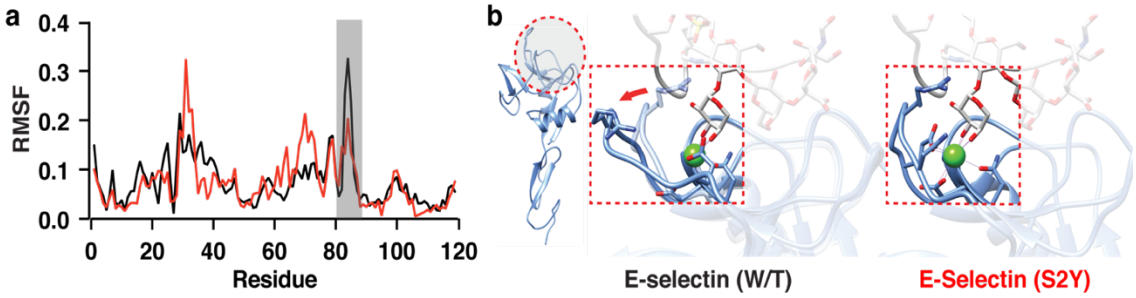

Figure 6.4: High affinity extended conformation allosterically forces the binding pocket to also adopt a high-affinity conformation in E-selectin. (A) RMSF per residue of the lectin domain of wildtype E-selectin (W/T) and variant E-selectin (S2Y). Grey rectangle highlights the flexible loop containing residues 83-85 of the binding pocket. (B) Schematics of flexible loop outlining the reduction of fluctuation in E-selectin (WT) compared to E-selectin (S2Y).

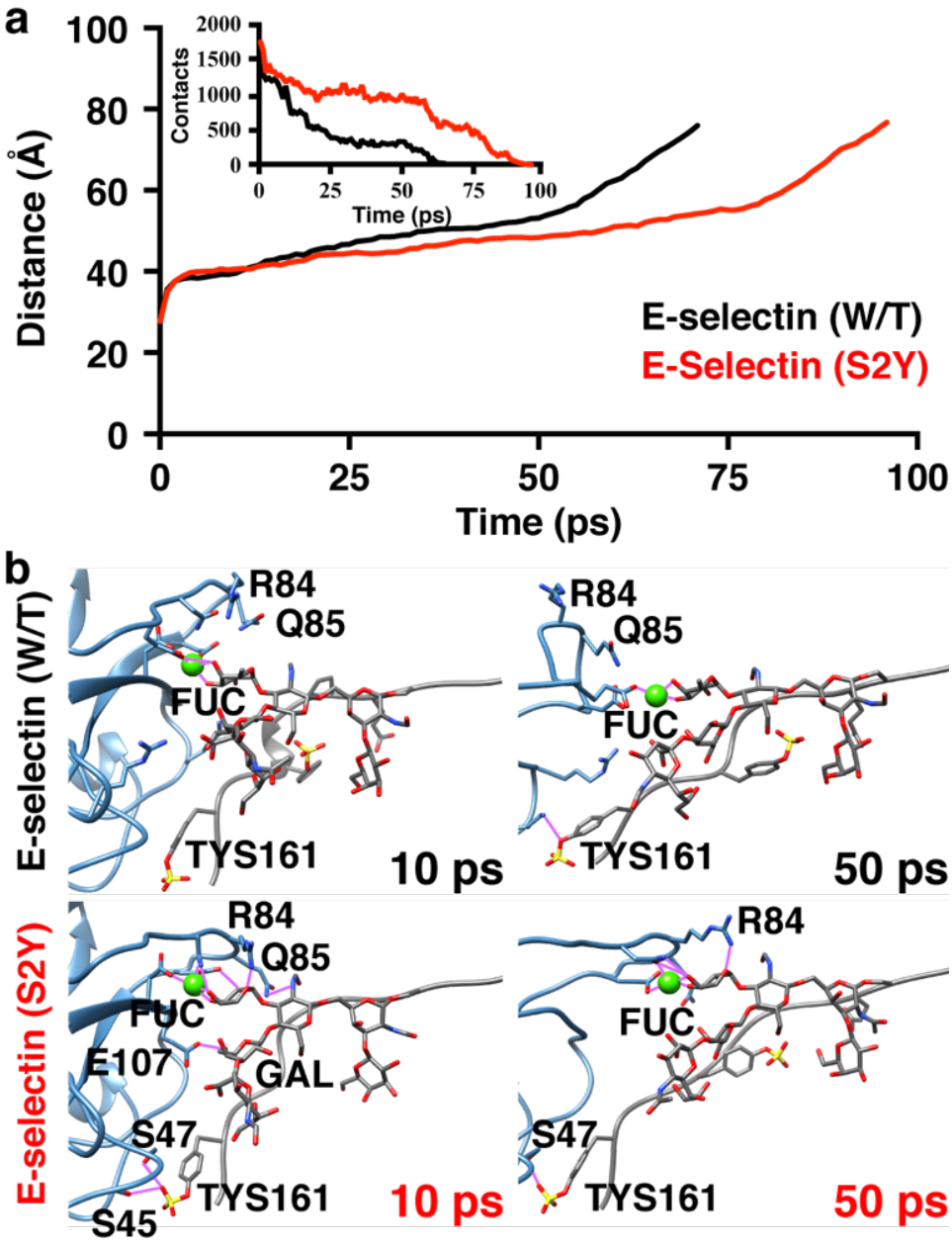

Figure 6.5: SMD simulations show PSGL-1 has higher affinity to E-Selectin (S2Y) than E-Selectin (W/T). (A) SMD simulation showing the dissociation time (in simulation time) of PSGL-1 from E-Selectin. (B) Representative illustrations of human E-selectin interaction with PSGL-1 as it is being pulled away from E-Selectin at the indicated time

points. E-selectin is blue; PSGL-1 is grey. Purple lines are representative of inter-molecular interactions.

-

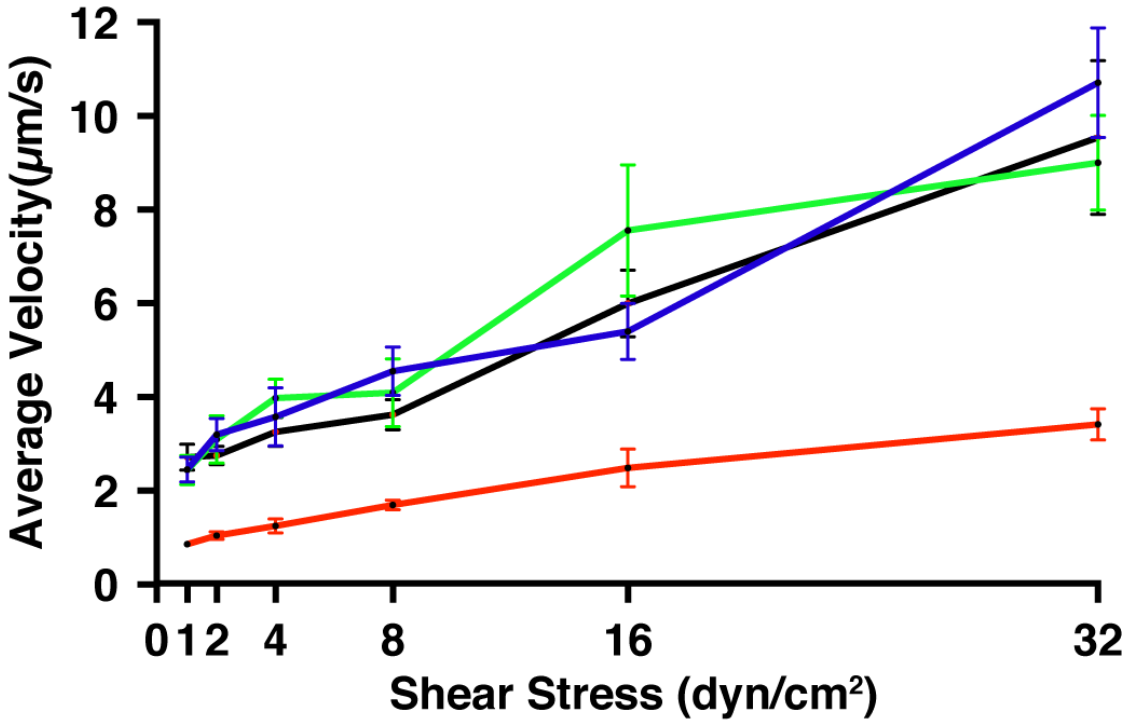

Figure 6.6: E-selectin (S2Y) has increased adhesiveness to ligands compared to the wildtype. The average rolling velocity of model cell line, KG-1a, ligands rolling on microtubes coated E-selectin-Fc chimeric protein.

■ *wildtype,* ■ *S2Y,* ■ *S2W,* ■ *S2C; n = 3)*

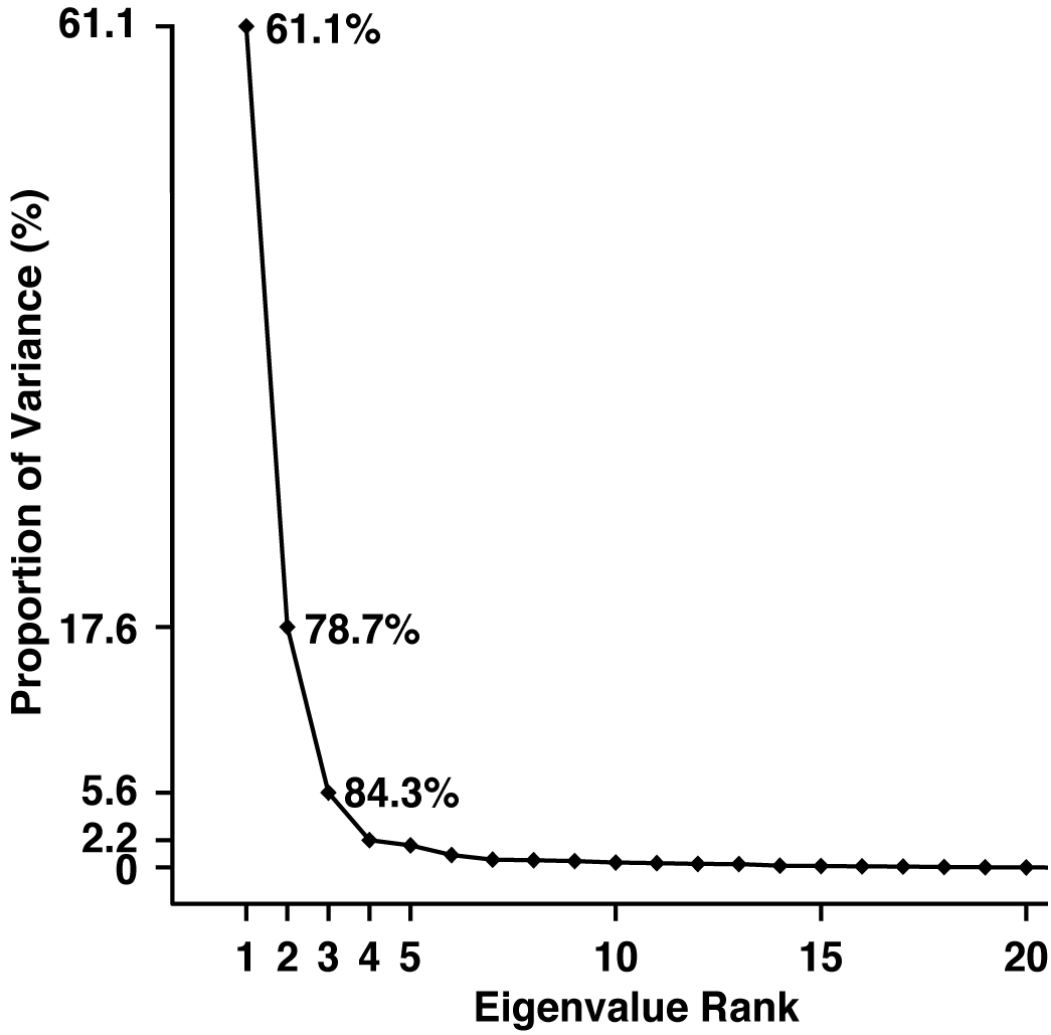

Figure 6.7: Proportion Percentage of the 20 Largest Eigenvalues (PCs). A representative distribution (%) of the 20 Largest Eigenvalues encapsulating the total displacement perturbation of an MD simulation of E-selectin.

REFERENCES

1. E. Lin, T. Cao, S. Nagrath, M. R. King, Circulating Tumor Cells: Diagnostic and Therapeutic Applications, *Annu. Rev. Biomed. Eng.* (2018), doi:10.1146/annurev-bioeng-062117-120947.

2. N. Bednarz-Knoll, C. Alix-Panabières, K. Pantel, Plasticity of disseminating cancer cells in patients with epithelial malignancies, *Cancer Metastasis Rev.* (2012), doi:10.1007/s10555-012-9370-z.

3. E. Marshall, Brawling over mammography*Science (80-.).* (2010), doi:10.1126/science.327.5968.936.

4. J. Abraham, Reduced lung cancer mortality with low-dose computed tomographic screening, *Community Oncol.* (2011), doi:10.1016/S1548-5315(12)70136-5.

5. J. M. Albert, Radiation risk from CT: Implications for cancer screening, *Am. J. Roentgenol.* (2013), doi:10.2214/AJR.12.9226.

6. B. K. Edwards, E. Ward, B. A. Kohler, C. Eheman, A. G. Zauber, R. N. Anderson, A. Jemal, M. J. Schymura, I. Lansdorp-Vogelaar, L. C. Seeff, M. Van Ballegooijen, S. L. Goede, L. A. G. Ries, Annual report to the nation on the status of cancer, 1975-2006, featuring colorectal cancer trends and impact of interventions (risk factors, screening, and treatment) to reduce future rates*Cancer* (2010), doi:10.1002/cncr.24760.

7. T. R. Ashworth, A case of cancer in which cells similar to those in the Tumours were seen in the blood after death., *Aust. Med J* (1869).

8. W. J. Allard, J. Matera, M. C. Miller, M. Repollet, M. C. Connelly, C. Rao, A. G. J.

Tibbe, J. W. Uhr, L. W. M. M. Terstappen, Tumor cells circulate in the peripheral blood of all major carcinomas but not in healthy subjects or patients with nonmalignant diseases, *Clin. Cancer Res.* (2004), doi:10.1158/1078-0432.CCR-04-0378.

9. D. Tripathy, Circulating tumor cells, disease progression, and survival in metastatic breast cancer, *Breast Dis.* (2005), doi:10.1016/S1043-321X(05)80001-3.

10. M. Cristofanilli, D. F. Hayes, G. T. Budd, M. J. Ellis, A. Stopeck, J. M. Reuben, G. V. Doyle, J. Matera, W. J. Allard, M. C. Miller, H. A. Fritsche, G. N. Hortobagyi, L. W. M. M. Terstappen, Circulating tumor cells: A novel prognostic factor for newly diagnosed metastatic breast cancer, *J. Clin. Oncol.* (2005), doi:10.1200/JCO.2005.08.140.

11. S. Riethdorf, H. Fritsche, V. Müller, T. Rau, C. Schindlbeck, B. Rack, W. Janni, C. Coith, K. Beck, F. Jänicke, S. Jackson, T. Gornet, M. Cristofanilli, K. Pantel, Detection of circulating tumor cells in peripheral blood of patients with metastatic breast cancer: A validation study of the cell search system, *Clin. Cancer Res.* (2007), doi:10.1158/1078-0432.CCR-06-1695.

12. H. Yagata, S. Nakamura, M. Toi, H. Bando, S. Ohno, A. Kataoka, Evaluation of circulating tumor cells in patients with breast cancer: Multi-institutional clinical trial in Japan, *Int. J. Clin. Oncol.* (2008), doi:10.1007/s10147-007-0748-9.

13. T. Kurihara, T. Itoi, A. Sofuni, F. Itokawa, T. Tsuchiya, S. Tsuji, K. Ishii, N. Ikeuchi, A. Tsuchida, K. Kasuya, T. Kawai, Y. Sakai, F. Moriyasu, Detection of circulating tumor cells in patients with pancreatic cancer: A preliminary result, *J. Hepatobiliary. Pancreat. Surg.* (2008), doi:10.1007/s00534-007-1250-5.

14. L. Khoja, A. Backen, R. Sloane, L. Menasce, D. Ryder, M. Krebs, R. Board, G. Clack, A. Hughes, F. Blackhall, J. W. Valle, C. Dive, A pilot study to explore circulating tumour cells in pancreatic cancer as a novel biomarker, *Br. J. Cancer* (2012), doi:10.1038/bjc.2011.545.

15. S. L. Stott, L. Richard, S. Nagrath, Y. Min, D. T. Miyamoto, L. Ulkus, E. J. Inserra, M. Ulman, S. Springer, Z. Nakamura, A. L. Moore, D. Tsukrov, M. E. Kempner, D. M. Dahl, W. Chin-lee, J. A. Iafrate, M. R. Smith, R. G. Tompkins, L. V. Sequist, M. Toner, D. A. Haber, S. Maheswaran, Isolation and characterization of circulating tumor cells from patients with localized and metastatic prostate cancer, *Sci. Transl. Med.* (2010), doi:10.1126/scitranslmed.3000403.

16. S. L. Stott, C.-H. Hsu, D. I. Tsukrov, M. Yu, D. T. Miyamoto, B. A. Waltman, S. M. Rothenberg, A. M. Shah, M. E. Smas, G. K. Korir, F. P. Floyd, A. J. Gilman, J. B. Lord, D. Winokur, S. Springer, D. Irimia, S. Nagrath, L. V. Sequist, R. J. Lee, K. J. Isselbacher, S. Maheswaran, D. A. Haber, M. Toner, Isolation of circulating tumor cells using a microvortex-generating herringbone-chip, *Proc. Natl. Acad. Sci.* (2010), doi:10.1073/pnas.1012539107.

17. S. Nagrath, L. V Sequist, S. Maheswaran, D. W. Bell, D. Irimia, L. Ulkus, M. R. Smith, E. L. Kwak, S. Digumarthy, A. Muzikansky, P. Ryan, U. J. Balis, R. G. Tompkins, D. A. Haber, M. Toner, Isolation of rare circulating tumour cells in cancer patients by microchip technology., *Nature* (2007), doi:10.1038/nature06385.

18. S. Maheswaran, L. V. Sequist, S. Nagrath, L. Ulkus, B. Brannigan, C. V. Collura, E. Inserra, S. Diederichs, A. J. Iafrate, D. W. Bell, S. Digumarthy, A. Muzikansky, D. Irimia, J. Settleman, R. G. Tompkins, T. J. Lynch, M. Toner, D. A. Haber, Detection

of Mutations in EGFR in Circulating Lung-Cancer Cells , *N. Engl. J. Med.* (2008), doi:10.1056/nejmoa0800668.

19. P. Cen, X. Ni, J. Yang, D. Y. Graham, M. Li, Circulating tumor cells in the diagnosis and management of pancreatic cancer*Biochim. Biophys. Acta - Rev. Cancer* (2012), doi:10.1016/j.bbcan.2012.05.007.

20. E. Soeth, U. Grigoleit, B. Moellmann, C. Röder, B. Schniewind, B. Kremer, H. Kalthoff, I. Vogel, Detection of tumor cell dissemination in pancreatic ductal carcinoma patients by CK 20 RT-PCR indicates poor survival, *J. Cancer Res. Clin. Oncol.* (2005), doi:10.1007/s00432-005-0008-1.

21. K. Hoffmann, C. Kerner, W. Wilfert, M. Mueller, J. Thiery, J. Hauss, H. Witzigmann, Detection of disseminated pancreatic cells by amplification of cytokeratin-19 with quantitative RT-PCR in blood, bone marrow and peritoneal lavage of pancreatic carcinoma patients, *World J. Gastroenterol.* (2007), doi:10.3748/wjg.v13.i2.257.

22. A. De Albuquerque, I. Kubisch, G. Breier, G. Stamminger, N. Fersis, A. Eichler, S. Kaul, U. Stölzel, Multimarker gene analysis of circulating tumor cells in pancreatic cancer patients: A feasibility study, *Oncology* (2012), doi:10.1159/000335479.

23. C. Alix-Panabieѐres, K. Pantel, Circulating tumor cells: Liquid biopsy of cancer*Clin. Chem.* (2013), doi:10.1373/clinchem.2012.194258.

24. P. Gazzaniga, C. Raimondi, C. Nicolazzo, R. Carletti, C. Di Gioia, A. Gradilone, E. Cortesi, The rationale for liquid biopsy in colorectal cancer: A focus on circulating tumor cells*Expert Rev. Mol. Diagn.* (2015), doi:10.1586/14737159.2015.1045491.

25. Z. Zhang, H. Shiratsuchi, J. Lin, G. Chen, R. M. Reddy, E. Azizi, S. Fouladdel, A. C. Chang, L. Lin, H. Jiang, M. Waghray, D. M. Simeone, M. S. Wicha, D. G. Beer, G. Luker, N. Ramnath, S. Nagrath, Abstract 370: Expansion of CTCs from early stage lung cancer patients using a microfluidic co-culture model, *Cancer Res.* (2015), doi:10.1158/1538-7445.am2015-370.

26. V. Murlidhar, R. M. Reddy, S. Fouladdel, L. Zhao, M. K. Ishikawa, S. Grabauskiene, Z. Zhang, J. Lin, A. C. Chang, P. Carrott, W. R. Lynch, M. B. Orringer, C. Kumar-Sinha, N. Palanisamy, D. G. Beer, M. S. Wicha, N. Ramnath, E. Azizi, S. Nagrath, Poor prognosis indicated by venous circulating tumor cell clusters in early-stage lung cancers, *Cancer Res.* (2017), doi:10.1158/0008-5472.CAN-16-2072.

27. K. Pantel, M. R. Speicher, The biology of circulating tumor cells*Oncogene* (2016), doi:10.1038/onc.2015.192.

28. J. B. Smerage, W. E. Barlow, G. N. Hortobagyi, E. P. Winer, B. Leyland-Jones, G. Srkalovic, S. Tejwani, A. F. Schott, M. A. O'Rourke, D. L. Lew, G. V. Doyle, J. R. Gralow, R. B. Livingston, D. F. Hayes, Circulating tumor cells and response to chemotherapy in metastatic breast cancer: SWOG S0500, *J. Clin. Oncol.* (2014), doi:10.1200/JCO.2014.56.2561.

29. L. Wan, K. Pantel, Y. Kang, Tumor metastasis: Moving new biological insights into the clinic*Nat. Med.* (2013), doi:10.1038/nm.3391.

30. C. Alix-Panabières, K. Pantel, Challenges in circulating tumour cell research, *Nat. Rev. Cancer* (2014), doi:10.1038/nrc3686.

31. T. M. Gorges, A. Kuske, K. Röck, O. Mauermann, V. Müller, S. Peine, K.

Verpoort, V. Novosadova, M. Kubista, S. Riethdorf, K. Pantel, Accession of tumor heterogeneity by multiplex transcriptome profiling of single circulating tumor cells, *Clin. Chem.* (2016), doi:10.1373/clinchem.2016.260299.

32. Z. Zhang, H. Shiratsuchi, N. Palanisamy, S. Nagrath, N. Ramnath, Expanded Circulating Tumor Cells from a Patient with ALK-Positive Lung Cancer Present with EML4-ALK Rearrangement Along with Resistance Mutation and Enable Drug Sensitivity Testing: A Case Study, *J. Thorac. Oncol.* (2017), doi:10.1016/j.jtho.2016.07.027.

33. N. V. Jordan, A. Bardia, B. S. Wittner, C. Benes, M. Ligorio, Y. Zheng, M. Yu, T. K. Sundaresan, J. A. Licausi, R. Desai, R. M. O'Keefe, R. Y. Ebright, M. Boukhali, S. Sil, M. L. Onozato, A. J. Iafrate, R. Kapur, D. Sgroi, D. T. Ting, M. Toner, S. Ramaswamy, W. Haas, S. Maheswaran, D. A. Haber, HER2 expression identifies dynamic functional states within circulating breast cancer cells, *Nature* (2016), doi:10.1038/nature19328.

34. B. T. Greene, A. D. Hughes, M. R. King, Circulating Tumor Cells: The Substrate of Personalized Medicine?, *Front. Oncol.* (2012), doi:10.3389/fonc.2012.00069.

35. S. Maheswaran, D. A. Haber, Circulating tumor cells: a window into cancer biology and metastasis*Curr. Opin. Genet. Dev.* (2010), doi:10.1016/j.gde.2009.12.002.

36. S. Riethdorf, H. Wikman, K. Pantel, Review: Biological relevance of disseminated tumor cells in cancer patients*Int. J. Cancer* (2008), doi:10.1002/ijc.23825.

37. A. F. Chambers, I. C. MacDonald, E. E. Schmidt, S. Koop, V. L. Morris, R. Khokha, A. C. Groom, Steps in tumor metastasis: new concepts from intravital

videomicroscopy, *Cancer Metastasis Rev.* (1995), doi:10.1007/BF00690599.

38. P. S. Steeg, Tumor metastasis: Mechanistic insights and clinical challenges*Nat. Med.* (2006), doi:10.1038/nm1469.

39. S. Chandrasekaran, M. R. King, Microenvironment of tumor-draining lymph nodes: Opportunities for liposome-based targeted therapy*Int. J. Mol. Sci.* (2014), doi:10.3390/ijms151120209.

40. C. L. Chaffer, R. A. Weinberg, A perspective on cancer cell metastasis*Science (80-.).* (2011), doi:10.1126/science.1203543.

41. W. a Franklin, J. Glaspy, S. M. Pflaumer, R. B. Jones, L. Hami, C. Martinez, J. R. Murphy, E. J. Shpall, Incidence of tumor-cell contamination in leukapheresis products of breast cancer patients mobilized with stem cell factor and granulocyte colony-stimulating factor (G-CSF) or with G-CSF alone., *Blood* (1999).

42. R. Gertler, R. Rosenberg, K. Fuehrer, M. Dahm, H. Nekarda, J. R. Siewert, Detection of circulating tumor cells in blood using an optimized density gradient centrifugation., *Recent Results Cancer Res.* (2003).

43. M. K. Baker, K. Mikhitarian, W. Osta, K. Callahan, R. Hoda, F. Brescia, R. Kneuper-Hall, M. Mitas, D. J. Cole, W. E. Gillanders, Molecular Detection of Breast Cancer Cells in the Peripheral Blood of Advanced-Stage Breast Cancer Patients Using Multimarker Real-Time Reverse Transcription-Polymerase Chain Reaction and a Novel Porous Barrier Density Gradient Centrifugation Technology, *Clin. Cancer Res.* (2003).

44. G. Vona, L. Estepa, C. Béroud, D. Damotte, F. Capron, B. Nalpas, A. Mineur, D.

Franco, B. Lacour, S. Pol, C. Bréchot, P. Paterlini-Bréchot, Impact of Cytomorphological Detection of Circulating Tumor Cells in Patients with Liver Cancer, *Hepatology* (2004), doi:10.1002/hep.20091.

45. R. L. Eifler, J. Lind, D. Falkenhagen, V. Weber, M. B. Fischer, R. Zeillinger, Enrichment of circulating tumor cells from a large blood volume using leukapheresis and elutriation: Proof of concept, *Cytom. Part B - Clin. Cytom.* (2011), doi:10.1002/cyto.b.20560.

46. J. C. Fischer, D. Niederacher, S. A. Topp, E. Honisch, S. Schumacher, N. Schmitz, L. Zacarias Fohrding, C. Vay, I. Hoffmann, N. S. Kasprowicz, P. G. Hepp, S. Mohrmann, U. Nitz, A. Stresemann, T. Krahn, T. Henze, E. Griebsch, K. Raba, J. M. Rox, F. Wenzel, C. Sproll, W. Janni, T. Fehm, C. A. Klein, W. T. Knoefel, N. H. Stoecklein, Diagnostic leukapheresis enables reliable detection of circulating tumor cells of nonmetastatic cancer patients, *Proc. Natl. Acad. Sci.* (2013), doi:10.1073/pnas.1313594110.

47. A. A. Ross, B. W. Cooper, H. M. Lazarus, W. Mackay, T. J. Moss, N. Ciobanu, M. S. Tallman, M. J. Kennedy, N. E. Davidson, D. Sweet, Detection and viability of tumor cells in peripheral blood stem cell collections from breast cancer patients using immunocytochemical and clonogenic assay techniques., *Blood* (1993).

48. G. Mazzolini, C. Alfaro, B. Sangro, E. Feijoó, J. Ruiz, A. Benito, I. Tirapu, A. Arina, J. Sola, M. Herraiz, F. Lucena, C. Olagüe, J. Subtil, J. Quiroga, I. Herrero, B. Sádaba, M. Bendandi, C. Qian, J. Prieto, I. Melero, Intratumoral injection of dendritic cells engineered to secrete interleukin-12 by recombinant adenovirus in patients with metastatic gastrointestinal carcinomas, *J. Clin. Oncol.* (2005),

doi:10.1200/JCO.2005.00.463.

49. A. M. Dohnal, S. Graffi, V. Witt, C. Eichstill, D. Wagner, S. Ul-Haq, D. Wimmer, T. Felzmann, Comparative evaluation of techniques for the manufacturing of dendritic cell-based cancer vaccines, *J. Cell. Mol. Med.* (2009), doi:10.1111/j.1582-4934.2008.00304.x.

50. M. E. Warkiani, L. Wu, A. K. P. Tay, J. Han, Large-Volume Microfluidic Cell Sorting for Biomedical Applications, *Annu. Rev. Biomed. Eng.* (2015), doi:10.1146/annurev-bioeng-071114-040818.

51. T. M. Gorges, K. Pantel, Circulating tumor cells as therapy-related biomarkers in cancer patients*Cancer Immunol. Immunother.* (2013), doi:10.1007/s00262-012-1387-1.

52. D. A. Nedosekin, M. Sarimollaoglu, J. H. Ye, E. I. Galanzha, V. P. Zharov, In vivo ultra-fast photoacoustic flow cytometry of circulating human melanoma cells using near-infrared high-pulse rate lasers, *Cytom. Part A* (2011), doi:10.1002/cyto.a.21102.

53. W. He, H. Wang, L. C. Hartmann, J.-X. Cheng, P. S. Low, In vivo quantitation of rare circulating tumor cells by multiphoton intravital flow cytometry, *Proc. Natl. Acad. Sci.* (2007), doi:10.1073/pnas.0703875104.

54. J. W. Kim, E. I. Galanzha, D. A. Zaharoff, R. J. Griffin, V. P. Zharov, Nanotheranostics of circulating tumor cells, infections and other pathological features in vivo*Mol. Pharm.* (2013), doi:10.1021/mp300577s.

55. V. P. Zharov, E. I. Galanzha, E. V. Shashkov, N. G. Khlebtsov, V. V. Tuchin, In vivo photoacoustic flow cytometry for monitoring of circulating single cancer cells

and contrast agents, *Opt. Lett.* (2006), doi:10.1364/OL.31.003623.

56. J. Novak, I. Georgakoudi, X. Wei, A. Prossin, C. P. Lin, In vivo flow cytometer for real-time detection and quantification of circulating cells, *Opt. Lett.* (2004), doi:10.1364/ol.29.000077.

57. E. I. Galanzha, J. W. Kim, V. P. Zharov, Nanotechnology-based molecular photoacoustic and photothermal flow cytometry platform for in-vivo detection and killing of circulating cancer stem cells, *J. Biophotonics* (2009), doi:10.1002/jbio.200910078.

58. A. F. Chambers, G. N. Naumov, S. A. Vantyghem, A. B. Tuck, Molecular biology of breast cancer metastasis. Clinical implications of experimental studies on metastatic inefficiency*Breast Cancer Res.* (2000), doi:10.1186/bcr86.

59. I. C. MacDonald, A. C. Groom, A. F. Chambers, Cancer spread and micrometastasis development: Quantitative approaches for in vivo models*BioEssays* (2002), doi:10.1002/bies.10156.

60. G. Gakhar, V. N. Navarro, M. Jurish, G. Y. Lee, S. T. Tagawa, N. H. Akhtar, M. Seandel, Y. Geng, H. Liu, N. H. Bander, P. Giannakakou, P. J. Christos, M. R. King, D. M. Nanus, Circulating tumor cells from prostate cancer patients interact with E-selectin under physiologic blood flow, *PLoS One* (2013), doi:10.1371/journal.pone.0085143.

61. K. Rana, J. L. Liesveld, M. R. King, Delivery of apoptotic signal to rolling cancer cells: A novel biomimetic technique using immobilized TRAIL and E-Selectin, *Biotechnol. Bioeng.* **102**, 1692–1702 (2009).

62. S. Wang, W. S. El-Deiry, TRAIL and apoptosis induction by TNF-family death receptors*Oncogene* (2003), doi:10.1038/sj.onc.1207232.

63. L. E. Phipps, S. Hino, R. J. Muschel, Targeting Cell Spreading: A Method of Sensitizing Metastatic Tumor Cells to TRAIL-Induced Apoptosis, *Mol. Cancer Res.* (2011), doi:10.1158/1541-7786.mcr-11-0021.

64. M. J. Mitchell, M. R. King, Fluid shear stress sensitizes cancer cells to receptor-mediated apoptosis via trimeric death receptors, *New J. Phys.* (2013), doi:10.1088/1367-2630/15/1/015008.

65. V. T. Turitto, Blood viscosity, mass transport, and thrombogenesis., *Prog Hemost Thromb* (1982).

66. M. J. Mitchell, M. R. King, Computational and Experimental Models of Cancer Cell Response to Fluid Shear Stress, *Front. Oncol.* (2013), doi:10.3389/fonc.2013.00044.

67. C. W. Luo, C. C. Wu, H. J. Ch'ang, Radiation sensitization of tumor cells induced by shear stress: The roles of integrins and FAK, *Biochim. Biophys. Acta - Mol. Cell Res.* (2014), doi:10.1016/j.bbamcr.2014.06.007.

68. M. J. Mitchell, E. Wayne, K. Rana, C. B. Schaffer, M. R. King, TRAIL-coated leukocytes that kill cancer cells in the circulation, *Proc. Natl. Acad. Sci.* **111**, 930–935 (2014).

69. E. C. Wayne, S. Chandrasekaran, M. J. Mitchell, M. F. Chan, R. E. Lee, C. B. Schaffer, M. R. King, TRAIL-coated leukocytes that prevent the bloodborne metastasis of prostate cancer, *J. Control. Release* (2016),

doi:10.1016/j.jconrel.2015.12.048.

70. M. Labelle, R. O. Hynes, The initial hours of metastasis: The importance of cooperative host-tumor cell interactions during hematogenous dissemination*Cancer Discov.* (2012), doi:10.1158/2159-8290.CD-12-0329.

71. L. J. Gay, B. Felding-Habermann, Contribution of platelets to tumour metastasis*Nat. Rev. Cancer* (2011), doi:10.1038/nrc3004.

72. L. J. Gay, B. Felding-Habermann, Platelets Alter Tumor Cell Attributes to Propel Metastasis: Programming in Transit*Cancer Cell* (2011), doi:10.1016/j.ccr.2011.11.001.

73. B. Nieswandt, M. Hafner, B. Echtenacher, D. N. Männel, Lysis of tumor cells by natural killer cells in mice is impeded by platelets, *Cancer Res.* (1999).

74. N. M. Bambace, C. E. Holmes, The platelet contribution to cancer progression*J. Thromb. Haemost.* (2011), doi:10.1111/j.1538-7836.2010.04131.x.

75. M. R. Weber, M. Zuka, M. Lorger, M. Tschan, B. E. Torbett, A. Zijlstra, J. P. Quigley, K. Staflin, B. P. Eliceiri, J. S. Krueger, P. Marchese, Z. M. Ruggeri, B. H. Felding, Activated tumor cell integrin αvβ3 cooperates with platelets to promote extravasation and metastasis from the blood stream, *Thromb. Res.* (2016), doi:10.1016/S0049-3848(16)30095-0.

76. M. Labelle, S. Begum, R. O. Hynes, Direct Signaling between Platelets and Cancer Cells Induces an Epithelial-Mesenchymal-Like Transition and Promotes Metastasis, *Cancer Cell* (2011), doi:10.1016/j.ccr.2011.09.009.

77. J. Wenzel, R. Zeisig, I. Fichtner, Inhibition of metastasis in a murine 4T1 breast

cancer model by liposomes preventing tumor cell-platelet interactions, *Clin. Exp. Metastasis* (2010), doi:10.1007/s10585-009-9299-y.

78. Y. Zhang, J. Wei, S. Liu, J. Wang, X. Han, H. Qin, J. Lang, K. Cheng, Y. Li, Y. Qi, G. J. Anderson, S. Sukumar, S. Li, G. Nie, Inhibition of platelet function using liposomal nanoparticles blocks tumor metastasis, *Theranostics* (2017), doi:10.7150/thno.17908.

79. W. Zhang, S. Dang, T. Hong, J. Tang, J. Fan, D. Bu, Y. Sun, Z. Wang, T. Wisniewski, Ahumanized single-chain antibody against beta 3 integrin inhibits pulmonary metastasis by preferentially fragmenting activated platelets in the tumor microenvironment, *Blood* (2012), doi:10.1182/blood-2012-04-425207.

80. J. Li, C. C. Sharkey, B. Wun, J. L. Liesveld, M. R. King, Genetic engineering of platelets to neutralize circulating tumor cells, *J. Control. Release* **228**, 38–47 (2016).

81. J. Li, Y. Ai, L. Wang, P. Bu, C. C. Sharkey, Q. Wu, B. Wun, S. Roy, X. Shen, M. R. King, Targeted drug delivery to circulating tumor cells via platelet membrane-functionalized particles, *Biomaterials* (2016), doi:10.1016/j.biomaterials.2015.10.046.

82. M. G. Best, N. Sol, I. Kooi, J. Tannous, B. A. Westerman, F. Rustenburg, P. Schellen, H. Verschueren, E. Post, J. Koster, B. Ylstra, N. Ameziane, J. Dorsman, E. F. Smit, H. M. Verheul, D. P. Noske, J. C. Reijneveld, R. J. A. Nilsson, B. A. Tannous, P. Wesseling, T. Wurdinger, RNA-Seq of Tumor-Educated Platelets Enables Blood-Based Pan-Cancer, Multiclass, and Molecular Pathway Cancer Diagnostics, *Cancer Cell* (2015), doi:10.1016/j.ccell.2015.09.018.

83. D. L. Morton, D. R. Wen, J. H. Wong, J. S. Economou, L. A. Cagle, F. K. Storm,

L. J. Foshag, A. J. Cochran, Technical Details of Intraoperative Lymphatic Mapping for Early Stage Melanoma, *Arch. Surg.* (1992), doi:10.1001/archsurg.1992.01420040034005.

84. M. I. Ross, Lymphatic mapping and sentinel node biopsy for early stage melanoma: How we do it at the M.D. Anderson cancer center, *J. Surg. Oncol.* (1997), doi:10.1002/(SICI)1096-9098(199712)66:4<273::AID-JSO11>3.0.CO;2-1.

85. P. O. Van Trappen, M. S. Pepper, Lymphatic dissemination of tumour cells and the formation of micrometastases*Lancet Oncol.* (2002), doi:10.1016/S1470-2045(01)00621-0.

86. S. P. L. Leong, E. K. Nakakura, R. Pollock, M. A. Choti, D. L. Morton, W. D. Henner, A. Lal, R. Pillai, O. H. Clark, B. Cady, Unique patterns of metastases in common and rare types of malignancy, *J. Surg. Oncol.* (2011), doi:10.1002/jso.21841.

87. P. Massucco, D. Ribero, E. Sgotto, A. Mellano, A. Muratore, L. Capussotti, Prognostic significance of lymph node metastases in pancreatic head cancer treated with extended lymphadenectomy: Not just a matter of numbers, *Ann. Surg. Oncol.* (2009), doi:10.1245/s10434-009-0672-5.

88. Y. Murakami, K. Uemura, T. Sudo, Y. Hayashidani, Y. Hashimoto, A. Nakashima, Y. Yuasa, N. Kondo, H. Ohge, T. Sueda, Number of metastatic lymph nodes, but not lymph node ratio, is an independent prognostic factor after resection of pancreatic carcinoma, *J. Am. Coll. Surg.* (2010), doi:10.1016/j.jamcollsurg.2010.03.037.

89. G. Gugliemetti, R. Sukhu, M. A. Conca Baenas, J. Meeks, D. D. Sjoberg, J. A. Eastham, P. T. Scardino, K. Touijer, Number of metastatic lymph nodes as

determinant of outcome after salvage radical prostatectomy for radiation-recurrent prostate cancer, *Actas Urológicas Españolas (English Ed.* (2016), doi:10.1016/j.acuroe.2016.06.004.

90. L. Maccio, V. Barresi, F. Domati, E. Martorana, A. M. Cesinaro, M. Migaldi, F. Iachetta, A. Ieni, L. R. Bonetti, Clinical significance of pelvic lymph node status in prostate cancer: review of 1690 cases, *Intern. Emerg. Med.* (2016), doi:10.1007/s11739-015-1375-5.

91. U. H. Von Andrian, T. R. Mempel, Homing and cellular traffic in lymph nodes*Nat. Rev. Immunol.* (2003), doi:10.1038/nri1222.

92. J. Weiden, J. Tel, C. G. Figdor, Synthetic immune niches for cancer immunotherapy*Nat. Rev. Immunol.* (2018), doi:10.1038/nri.2017.89.

93. D. H. Munn, A. L. Mellor, The tumor-draining lymph node as an immune-privileged site*Immunol. Rev.* (2006), doi:10.1111/j.1600-065X.2006.00444.x.

94. A. Bhatia, Y. Kumar, Cellular and molecular mechanisms in cancer immune escape: A comprehensive review*Expert Rev. Clin. Immunol.* (2014), doi:10.1586/1744666X.2014.865519.

95. L. Zamai, M. Ahmad, I. M. Bennett, L. Azzoni, E. S. Alnemri, B. Perussia, Natural Killer (NK) Cell–mediated Cytotoxicity: Differential Use of TRAIL and Fas Ligand by Immature and Mature Primary Human NK Cells, *J. Exp. Med.* (2002), doi:10.1084/jem.188.12.2375.

96. M. J. Smyth, E. Cretney, K. Takeda, R. H. Wiltrout, L. M. Sedger, N. Kayagaki, H. Yagita, K. Okumura, Tumor necrosis factor-related apoptosis-inducing ligand

(TRAIL) contributes to interferon gamma-dependent natural killer cell protection from tumor metastasis., *J. Exp. Med.* (2001).

97. I. S. Schuster, M. E. Wikstrom, G. Brizard, J. D. Coudert, M. J. Estcourt, M. Manzur, L. A. O'Reilly, M. J. Smyth, J. A. Trapani, G. R. Hill, C. E. Andoniou, M. A. Degli-Esposti, TRAIL+ NK Cells Control CD4+ T Cell Responses during Chronic Viral Infection to Limit Autoimmunity, *Immunity* (2014), doi:10.1016/j.immuni.2014.09.013.

98. J. D. Wu, L. M. Higgins, A. Steinle, D. Cosman, K. Haugk, S. R. Plymate, Prevalent expression of the immunostimulatory MHC class I chain-related molecule is counteracted by shadding in prostate cancer, *J. Clin. Invest.* (2004), doi:10.1172/JCI200422206.

99. A. Garcia-Lora, I. Algarra, F. Garrido, MHC class I antigens, immune surveillance, and tumor immune escape*J. Cell. Physiol.* (2003), doi:10.1002/jcp.10290.

100. V. Groh, J. Wu, C. Yee, T. Spies, Tumour-derived soluble MIC ligands impair expression of NKG2D and T-cell activation, *Nature* (2002), doi:10.1038/nature01112.

101. J.-C. Lee, K.-M. Lee, D.-W. Kim, D. S. Heo, Elevated TGF-beta1 secretion and down-modulation of NKG2D underlies impaired NK cytotoxicity in cancer patients., *J. Immunol.* (2004).

102. L. Ruggeri, M. Capanni, E. Urbani, K. Perruccio, W. D. Shlomchik, A. Tosti, S. Posati, D. Rogaia, F. Frassoni, F. Aversa, M. F. Martelli, A. Velardi, Effectiveness of donor natural killer cell aloreactivity in mismatched hematopoietic transplants,

Science (80-.). (2002), doi:10.1126/science.1068440.

103. E. Ishikawa, K. Tsuboi, K. Saijo, H. Harada, S. Takano, T. Nose, T. Ohno, Autologous natural killer cell therapy for human recurrent malignant glioma, *Anticancer Res.* (2004).

104. A. Lundqvist, J. P. McCoy, L. Samsel, R. Childs, Reduction of GVHD and enhanced antitumor effects after adoptive infusion of alloreactive Ly49-mismatched NK cells from MHC-matched donors, *Blood* (2007), doi:10.1182/blood-2006-05-024315.

105. M. Cheng, Y. Chen, W. Xiao, R. Sun, Z. Tian, NK cell-based immunotherapy for malignant diseases*Cell. Mol. Immunol.* (2013), doi:10.1038/cmi.2013.10.

106. S. Chandrasekaran, M. J. McGuire, M. R. King, Sweeping lymph node micrometastases off their feet: An engineered model to evaluate natural killer cell mediated therapeutic intervention of circulating tumor cells that disseminate to the lymph nodes, *Lab Chip* (2014), doi:10.1039/c3lc50584g.

107. S. Chandrasekaran, M. F. Chan, J. Li, M. R. King, Super natural killer cells that target metastases in the tumor draining lymph nodes, *Biomaterials* (2016), doi:10.1016/j.biomaterials.2015.11.001.

108. J. Banchereau, R. M. Steinman, Dendritic cells and the control of immunity*Nature* (1998), doi:10.1038/32588.

109. Y. Ma, G. V. Shurin, Z. Peiyuan, M. R. Shurin, Dendritic cells in the cancer microenvironment*J. Cancer* (2013), doi:10.7150/jca.5046.

110. W. H. Fridman, F. Pagès, C. Sautès-Fridman, J. Galon, The immune contexture in

human tumours: Impact on clinical outcome*Nat. Rev. Cancer* (2012), doi:10.1038/nrc3245.

111. M. Azuma, T. Ebihara, H. Oshiumi, M. Matsumoto, T. Seya, Cross-priming for antitumor ctl induced by soluble ag + polyi: C depends on the ticam-1 pathway in mouse cd11c+/CD8α+ dendritic cells, *Oncoimmunology* (2012), doi:10.4161/onci.19893.

112. W. A., O. S., G. S., V. R.N., E. K., L. W.C., C. W., In vivo vaccination with tumor cell lysate plus CpG oligodeoxynucleotides eradicates murine glioblastoma, *J. Immunother.* (2007), doi:http://dx.doi.org/10.1097/CJI.0b013e318155a0f6.

113. A. Pinzon-Charry, T. Maxwell, J. A. López, Dendritic cell dysfunction in cancer: A mechanism for immunosuppression*Immunol. Cell Biol.* (2005), doi:10.1111/j.1440-1711.2005.01371.x.

114. J. Banchereau, A. K. Palucka, M. Dhodapkar, S. Burkeholder, N. Taquet, A. Rolland, S. Taquet, S. Coquery, K. M. Wittkowski, N. Bhardwaj, L. Pineiro, R. Steinman, J. Fay, Immune and clinical responses in patients with metastatic melanoma to CD34+ progenitor-derived dendritic cell vaccine, *Cancer Res.* (2001).

115. L. Jeanbart, M. Ballester, A. de Titta, P. Corthesy, P. Romero, J. A. Hubbell, M. A. Swartz, Enhancing Efficacy of Anticancer Vaccines by Targeted Delivery to Tumor-Draining Lymph Nodes, *Cancer Immunol. Res.* (2014), doi:10.1158/2326-6066.CIR-14-0019-T.

116. S. N. Thomas, E. Vokali, A. W. Lund, J. A. Hubbell, M. A. Swartz, Targeting the tumor-draining lymph node with adjuvanted nanoparticles reshapes the anti-tumor

immune response, *Biomaterials* (2014), doi:10.1016/j.biomaterials.2013.10.003.

117. Y. Liu, L. Xiao, K. Il Joo, B. Hu, J. Fang, P. Wang, In situ modulation of dendritic cells by injectable thermosensitive hydrogels for cancer vaccines in mice, *Biomacromolecules* (2014), doi:10.1021/bm501166j.

118. O. A. Ali, N. Huebsch, L. Cao, G. Dranoff, D. J. Mooney, Infection-mimicking materials to program dendritic cells in situ, *Nat. Mater.* (2009), doi:10.1038/nmat2357.

119. O. A. Ali, S. A. Lewin, G. Dranoff, D. J. Mooney, Vaccines Combined with Immune Checkpoint Antibodies Promote Cytotoxic T-cell Activity and Tumor Eradication, *Cancer Immunol. Res.* (2016), doi:10.1158/2326-6066.cir-14-0126.

120. R. W. L. Godschalk, A. M. Knaapen, N. Gungor, R. K. Chiu, A. Munnia, G. R. Haenen, M. Peluso, F. J. van Schooten, Genotoxic effects of neutrophils and hypochlorous acid, *Mutagenesis* **25**, 149–154 (2009).

121. M. Atkins, J. Zabaleta, M. S. Ernstoff, A. C. Ochoa, P. C. Rodriguez, C. Hernandez, R. Sierra, Arginase I–Producing Myeloid-Derived Suppressor Cells in Renal Cell Carcinoma Are a Subpopulation of Activated Granulocytes, *Cancer Res.* **69**, 1553–1560 (2009).

122. D. Jurk, N. Fullard, A. Page, A. M. Elsharkawy, S. Luli, C. L. Wilson, D. A. Mann, K. Callaghan, A. Lagnado, J. Mann, G. R. Smith, C. Richardson, A. J. Moore, F. Oakley, J. B. Chakraborty, D. G. Tiniakos, G. E. Blair, N. Fox, J. F. Passos, P. Banks, R. G. Gieling, C. Fox, NFκB1 is a suppressor of neutrophil-driven hepatocellular carcinoma, *Nat. Commun.* **6**, 6818 (2015).

123. A. D. Gregory, A. M. Houghton, Tumor-associated neutrophils: New targets for cancer therapy*Cancer Res.* **71**, 2411–2416 (2011).

124. H. Nozawa, C. Chiu, D. Hanahan, Infiltrating neutrophils mediate the initial angiogenic switch in a mouse model of multistage carcinogenesis, *Proc. Natl. Acad. Sci.* **103**, 12493–12498 (2006).

125. S. M. Albelda, G. S. Worthen, G. Cheng, S. Kim, L. Ling, J. Sun, V. Kapoor, Z. G. Fridlender, Polarization of Tumor-Associated Neutrophil Phenotype by TGF-β: "N1" versus "N2" TAN, *Cancer Cell* **16**, 183–194 (2009).

126. S. G. Thacker, S. Yalavarthi, M. J. Kaplan, A. R. Sandy, W. Zhao, M. Anderson, W. J. McCune, M. F. Denny, A Distinct Subset of Proinflammatory Neutrophils Isolated from Patients with Systemic Lupus Erythematosus Induces Vascular Damage and Synthesizes Type I IFNs, *J. Immunol.* **184**, 3284–3297 (2010).

127. B. M. Szczerba, F. Castro-Giner, M. Vetter, I. Krol, S. Gkountela, J. Landin, M. C. Scheidmann, C. Donato, R. Scherrer, J. Singer, C. Beisel, C. Kurzeder, V. Heinzelmann-Schwarz, C. Rochlitz, W. P. Weber, N. Beerenwinkel, N. Aceto, Neutrophils escort circulating tumour cells to enable cell cycle progression, *Nature* **566**, 553–557 (2019).

128. S. K. Wculek, I. Malanchi, Neutrophils support lung colonization of metastasis-initiating breast cancer cells, *Nature* **528**, 413–417 (2015).

129. V. Brinkmann, U. Reichard, C. Goosmann, B. Fauler, Y. Uhlemann, D. S. Weiss, Y. Weinrauch, A. Zychlinsky, Neutrophil Extracellular Traps Kill Bacteria, *Science (80-.).* **303**, 1532–1535 (2004).

130. V. Papayannopoulos, Neutrophil extracellular traps in immunity and disease*Nat. Rev. Immunol.* **18**, 134–147 (2018).

131. J. E. De Larco, B. R. K. Wuertz, L. T. Furcht, J. E. De Larco, The Potential Role of Neutrophils in Promoting the Metastatic Phenotype of Tumors Releasing Interleukin-8 The Potential Role of Neutrophils in Promoting the Metastatic Phenotype of Tumors Releasing Interleukin-8, *Clin. Cancer Res.* **10**, 4895–4900 (2004).

132. M. Demers, D. D. Wagner, D. Schatzberg, T. A. Fuchs, J. R. Voorhees, D. T. Scadden, D. S. Krause, K. Martinod, Cancers predispose neutrophils to release extracellular DNA traps that contribute to cancer-associated thrombosis, *Proc. Natl. Acad. Sci.* **109**, 13076–13081 (2012).

133. B. Giannias, L. Ferri, J. Cools-Lartigue, S. Gowing, F. Bourdeau, J. Spicer, B. McDonald, P. Kubes, S. Chow, Neutrophil extracellular traps sequester circulating tumor cells and promote metastasis, *J. Clin. Invest.* **123**, 3446–3458 (2013).

134. E. Pedruzzi, M. Fay, C. Elbim, M. Gaudry, M.-A. Gougerot-Pocidalo, Differentiation of PLB-985 myeloid cells into mature neutrophils, shown by degranulation of terminally differentiated compartments in response to N-formyl peptide and priming of superoxide anion production by granulocyte-macrophage colony-stimulating fact, *Br. J. Haematol.* **117**, 719–26 (2002).

135. V. Lievin-Le Moal, S. Chollet-Martin, A. Gleizes, A. L. Servin, I. Turbica, C. Sandré, V. Marin-Esteban, N. Semiramoth, G. Dufour, R. Gorges, I. Beau, S. M. Payne, Ed. Afa/Dr Diffusely Adhering Escherichia coli Strain C1845 Induces Neutrophil Extracellular Traps That Kill Bacteria and Damage Human Enterocyte-

Like Cells, *Infect. Immun.* **80**, 1891–1899 (2012).

136. T. M. Cao, T. Takatani, M. R. King, Effect of Extracellular pH on Selectin Adhesion: Theory and Experiment, *Biophys. J.* **104**, 292–299 (2013).

137. K. Ley, P. Gaehtgens, C. Fennie, M. S. Singer, L. a Lasky, S. D. Rosen, Lectin-like cell adhesion molecule 1 mediates leukocyte rolling in mesenteric venules in vivo., *Blood* (1991).

138. R. Alon, H. Rossiter, X. Wang, T. A. Springer, T. S. Kupper, Distinct cell surface ligands mediate T lymphocyte attachment and rolling on P and E selectin under physiological flow, *J. Cell Biol.* (1994), doi:10.1083/jcb.127.5.1485.

139. T. A. Springer, Traffic signals for lymphocyte recirculation and leukocyte emigration: The multistep paradigm*Cell* (1994), doi:10.1016/0092-8674(94)90337-9.

140. B. W. Weston, K. M. Hiller, J. P. Mayben, G. A. Manousos, K. M. Bendt, R. Liu, J. C. Cusack, Expression of human α(1,3)fucosyltransferase antisense sequences inhibits selectin-mediated adhesion and liver metastasis of colon carcinoma cells, *Cancer Res.* (1999).

141. Y. Geng, J. R. Marshall, M. R. King, Glycomechanics of the metastatic cascade: Tumor cell-endothelial cell interactions in the circulation*Ann. Biomed. Eng.* (2012), doi:10.1007/s10439-011-0463-6.

142. P. Harrison, E. M. Cramer, Platelet alpha-granules., *Blood Rev.* (1993).

143. R. P. McEver, K. L. Moore, R. D. Cummings, Leukocyte trafficking mediated by selectin-carbohydrate interactions*J. Biol. Chem.* (1995), doi:10.1074/jbc.270.19.11025.

144. K. Ley, G. S. Kansas, Selectins in T-cell recruitment to non-lymphoid tissues and sites of inflammation, *Nat. Rev. Immunol.* **4**, 325–336 (2004).

145. Y. Katayama, A. Hidalgo, B. C. Furie, D. Vestweber, B. Furie, P. S. Frenette, PSGL-1 participates in E-selectin-mediated progenitor homing to bone marrow: Evidence for cooperation between E-selectin ligands and α4 integrin, *Blood* **102**, 2060–2067 (2003).

146. G. S. Kansas, G. S. Wood, D. M. Fishwild, E. G. Engleman, Functional characterization of human T lymphocyte subsets distinguished by monoclonal anti-leu-8., *J. Immunol.* (1985).

147. R. P. McEVER, Role of Selectins in Leukocyte Adhesion to Platelets and Endothelium, *Ann. N. Y. Acad. Sci.* (1994), doi:10.1111/j.1749-6632.1994.tb12043.x.

148. A. Varki, Selectin ligands., *Proc. Natl. Acad. Sci.* (2006), doi:10.1073/pnas.91.16.7390.

149. G. S. Kansas, Selectins and their ligands: current concepts and contreoversies, *Blood* **88**, 3259–3287 (1996).

150. C. J. Dimitroff, J. Y. Lee, R. C. Fuhlbrigge, R. Sackstein, A distinct glycoform of CD44 is an L-selectin ligand on human hematopoietic cells, *Proc. Natl. Acad. Sci.* (2002), doi:10.1073/pnas.250484797.

151. M. Kitakaze, M. L. Weisfeldt, E. Marban, Acidosis during early reperfusion prevents myocardial stunning in perfused ferret hearts, *J. Clin. Invest.* (1988), doi:10.1172/JCI113699.

152. C. H. Orchard, J. C. Kentish, Effects of changes of pH on the contractile function

of cardiac muscle, *Am. J. Physiol. Physiol.* (2017), doi:10.1152/ajpcell.1990.258.6.c967.

153. A. Lengheden, L. Jansson, PH effects on experimental wound healing of human fibroblasts in vitro, *Eur. J. Oral Sci.* (1995), doi:10.1111/j.1600-0722.1995.tb00016.x.

154. Y. Liu, A. Kalén, O. Risto, O. Wahlström, Fibroblast proliferation due to exposure to a platelet concentrate in vitro is pH dependent, *Wound Repair Regen.* (2002), doi:10.1046/j.1524-475X.2002.10510.x.

155. C. V. Serrano, A. Fraticelli, R. Paniccia, A. Teti, B. Noble, S. Corda, T. Faraggiana, R. C. Ziegelstein, J. L. Zweier, M. C. Capogrossi, pH dependence of neutrophil-endothelial cell adhesion and adhesion molecule expression, *Am. J. Physiol. Physiol.* (2017), doi:10.1152/ajpcell.1996.271.3.c962.

156. D. R. Knighton, T. K. Hunt, H. Scheuenstuhl, B. J. Halliday, Z. Werb, M. J. Banda, Oxygen Tension Regulates the Expression of Angiogenesis Factor by Macrophages, *Science (80-.).* (1983), doi:10.1126/science.6612342.

157. R. A. Gatenby, R. J. Gillies, Why do cancers have high aerobic glycolysis?*Nat. Rev. Cancer* (2004), doi:10.1038/nrc1478.

158. M. C. Brahimi-Horn, G. Bellot, J. Pouysségur, Hypoxia and energetic tumour metabolism*Curr. Opin. Genet. Dev.* (2011), doi:10.1016/j.gde.2010.10.006.

159. W. S. Somers, J. Tang, G. D. Shaw, R. T. Camphausen, Insights into the molecular basis of leukocyte tethering and rolling revealed by structures of P-and E-seiectin bound to SLe(X) and PSGL-1, *Cell* **103**, 467–479 (2000).

160. E. Krieger, T. Darden, S. B. Nabuurs, A. Finkelstein, G. Vriend, Making optimal

use of empirical energy functions: Force-field parameterization in crystal space, *Proteins Struct. Funct. Genet.* (2004), doi:10.1002/prot.20251.

161. U. Essmann, L. Perera, M. L. Berkowitz, T. Darden, H. Lee, L. G. Pedersen, A smooth particle mesh Ewald method, *J. Chem. Phys.* (1995), doi:10.1063/1.470117.

162. E. Krieger, J. E. Nielsen, C. A. E. M. Spronk, G. Vriend, Fast empirical pKa prediction by Ewald summation, *J. Mol. Graph. Model.* (2006), doi:10.1016/j.jmgm.2006.02.009.

163. A. S. Konagurthu, J. C. Whisstock, P. J. Stuckey, A. M. Lesk, MUSTANG: A multiple structural alignment algorithm, *Proteins Struct. Funct. Genet.* (2006), doi:10.1002/prot.20921.

164. A. G. Klopocki, T. Yago, P. Mehta, J. Yang, T. Wu, A. Leppänen, N. V. Bovin, R. D. Cummings, C. Zhu, R. P. McEver, Replacing a lectin domain residue in L-selectin enhances binding to P-selectin glycoprotein ligand-1 but not to 6-sulfo-sialyl Lewis x, *J. Biol. Chem.* (2008), doi:10.1074/jbc.M709785200.

165. K. K. Sarangapani, J. Qian, W. Chen, V. I. Zarnitsyna, P. Mehta, T. Yago, R. P. McEver, C. Zhu, Regulation of catch bonds by rate of force application, *J. Biol. Chem.* (2011), doi:10.1074/jbc.M111.240044.

166. J. Lou, C. Zhu, A structure-based sliding-rebinding mechanism for catch bonds, *Biophys. J.* (2007), doi:10.1529/biophysj.106.097048.

167. C. J. Ball, M. R. King, Role of c-Abl in L-selectin shedding from the neutrophil surface, *Blood Cells, Mol. Dis.* (2011), doi:10.1016/j.bcmd.2010.12.010.

168. D. Lee, J. B. Schultz, P. A. Knauf, M. R. King, Mechanical shedding of L-

selectin from the neutrophil surface during rolling on sialyl Lewis x under flow, *J. Biol. Chem.* **282**, 4812–4820 (2007).

169. S. D. Narasipura, J. C. Wojciechowski, N. Charles, J. L. Liesveld, M. R. King, P-selectin-coated microtube for enrichment of CD34+ hematopoietic stem and progenitor cells from human bone marrow, *Clin. Chem.* (2008), doi:10.1373/clinchem.2007.089896.

170. R. P. McEver, C. Zhu, Rolling Cell Adhesion, *Annu. Rev. Cell Dev. Biol.* (2010), doi:10.1146/annurev.cellbio.042308.113238.

171. J. Etulain, S. Negrotto, A. Carestia, R. G. Pozner, M. A. Romaniuk, L. P. D'Atri, G. L. Klement, M. Schattner, Acidosis downregulates platelet haemostatic functions and promotes neutrophil proinflammatory responses mediated by platelets, *Thromb. Haemost.* (2012), doi:10.1160/TH11-06-0443.

172. U. T. Phan, T. T. Waldron, T. A. Springer, Remodeling of the lectin-EGF-like domain interface in P- and L-selectin increases adhesiveness and shear resistance under hydrodynamic force, *Nat. Immunol.* **7**, 883–889 (2006).

173. T. K. Kishimoto, M. A. Jutila, E. C. Butcher, Identification of a human peripheral lymph node homing receptor: a rapidly down-regulated adhesion molecule., *Proc. Natl. Acad. Sci.* (2006), doi:10.1073/pnas.87.6.2244.

174. S. Chen, T. A. Springer, An automatic braking system that stabilizes leukocyte rolling by an increase in selectin bond number with shear, *J. Cell Biol.* (1999), doi:10.1083/jcb.144.1.185.

175. P. Pawar, S. Jadhav, C. D. Eggleton, K. Konstantopoulos, Roles of cell and

microvillus deformation and receptor-ligand binding kinetics in cell rolling, *Am. J. Physiol. Circ. Physiol.* (2008), doi:10.1152/ajpheart.91536.2007.

176. A. D. Hughes, J. Mattison, L. T. Western, J. D. Powderly, B. T. Greene, M. R. King, Microtube device for selectin-mediated capture of viable circulating tumor cells from blood, *Clin. Chem.* **58**, 846–853 (2012).

177. T. M. Cao, M. J. Mitchell, J. Liesveld, M. R. King, Stem cell enrichment with selectin receptors: Mimicking the pH environment of trauma, *Sensors (Switzerland)* (2013), doi:10.3390/s130912516.

178. M. Ogawa, Differentiation and proliferation of hematopoietic stem cells., *Blood* (1993).

179. M. Kondo, A. J. Wagers, M. G. Manz, S. S. Prohaska, D. C. Scherer, G. F. Beilhack, J. A. Shizuru, I. L. Weissman, B IOLOGY OF H EMATOPOIETIC S TEM C ELLS AND P ROGENITORS : Implications for Clinical Application , *Annu. Rev. Immunol.* (2003), doi:10.1146/annurev.immunol.21.120601.141007.

180. B. R. Dey, J. Shaffer, A. J. Yee, S. McAfee, M. Caron, K. Power, D. T. Ting, C. Colby, F. Preffer, K. Ballen, E. Attar, S. Saidman, N. Tarbell, D. Sachs, M. Sykes, T. R. Spitzer, Comparison of outcomes after transplantation of peripheral blood stem cells versus bone marrow following an identical nonmyeloablative conditioning regimen, *Bone Marrow Transplant.* (2007), doi:10.1038/sj.bmt.1705688.

181. A. Dodero, C. Carniti, A. Raganato, A. Vendramin, L. Farina, F. Spina, C. Carlo-Stella, S. Di Terlizzi, M. Milanesi, P. Longoni, L. Gandola, C. Lombardo, P. Corradini, Haploidentical stem cell transplantation after a reduced-intensity

conditioning regimen for the treatment of advanced hematologic malignancies: Posttransplantation CD8-depleted donor lymphocyte infusions contribute to improve T-cell recovery, *Blood* (2009), doi:10.1182/blood-2008-10-183723.

182. S. H. Chu, D. Heiser, L. Li, I. Kaplan, M. Collector, D. Huso, S. J. Sharkis, C. Civin, D. Small, FLT3-ITD knockin impairs hematopoietic stem cell quiescence/homeostasis, leading to myeloproliferative neoplasm, *Cell Stem Cell* (2012), doi:10.1016/j.stem.2012.05.027.

183. Y. Zhang, X. Yan, G. Sashida, X. Zhao, Y. Rao, S. Goyama, S. P. Whitman, N. Zorko, K. Bernot, R. M. Conway, D. Witte, Q. F. Wang, D. G. Tenen, Z. Xiao, G. Marcucci, J. C. Mulloy, H. L. Grimes, M. A. Caligiuri, G. Huang, Stress hematopoiesis reveals abnormal control of self-renewal, lineage bias, and myeloid differentiation in Mll partial tandem duplication (Mll-PTD) hematopoietic stem/progenitor cells, *Blood* (2012), doi:10.1182/blood-2012-02-412379.

184. S. H. Orkin, L. I. Zon, Hematopoiesis: an evolving paradigm for stem cell biology., *Cell* (2008), doi:10.1016/j.cell.2008.01.025.

185. A. D. Bearpark, M. Y. Gordon, Adhesive properties distinguish sub-populations of haemopoietic stem cells with different spleen colony-forming and marrow repopulating capacities, *Bone Marrow Transpl.* (1989).

186. D. E. Wright, A. J. Wagers, A. Pathak Gulati, F. L. Johnson, I. L. Weissman, Physiological migration of hematopoietic stem and progenitor cells, *Science (80-.).* (2001), doi:10.1126/science.1064081.

187. W. H. Fleming, E. J. Alpern, N. Uchida, K. Ikuta, I. L. Weissman, Steel factor

influences the distribution and activity of murine hematopoietic stem cells in vivo., *Proc. Natl. Acad. Sci.* (2006), doi:10.1073/pnas.90.8.3760.

188. A. G. Smith, Embryo-Derived Stem Cells: Of Mice and Men, *Annu. Rev. Cell Dev. Biol.* (2002), doi:10.1146/annurev.cellbio.17.1.435.

189. D. J. Laird, U. H. von Andrian, A. J. Wagers, Stem Cell Trafficking in Tissue Development, Growth, and Disease*Cell* (2008), doi:10.1016/j.cell.2008.01.041.

190. A. M. Müller, A. Medvinsky, J. Strouboulis, F. Grosveld, E. Dzierzakt, Development of hematopoietic stem cell activity in the mouse embryo, *Immunity* (1994), doi:10.1016/1074-7613(94)90081-7.

191. S. Massberg, P. Schaerli, I. Knezevic-Maramica, M. Köllnberger, N. Tubo, E. A. Moseman, I. V. Huff, T. Junt, A. J. Wagers, I. B. Mazo, U. H. von Andrian, Immunosurveillance by Hematopoietic Progenitor Cells Trafficking through Blood, Lymph, and Peripheral Tissues, *Cell* (2007), doi:10.1016/j.cell.2007.09.047.

192. H. M. Lee, M. Z. Ratajczak, Innate immunity: a key player in the mobilization of hematopoietic stem/progenitor cells.*Arch. Immunol. Ther. Exp. (Warsz).* (2009), doi:10.1007/s00005-009-0037-6.

193. M. Z. Ratajczak, C. H. Kim, W. Wojakowski, A. Janowska-Wieczorek, M. Kucia, J. Ratajczak, Innate immunity as orchestrator of stem cell mobilization*Leukemia* (2010), doi:10.1038/leu.2010.162.

194. C. J. Dimitroff, J. Y. Lee, K. S. Schor, B. M. Sandmaier, R. Saekstein, Differential L-Selectin Binding Activities of Human Hematopoietic Cell L-Selectin Ligands, HCELL and PSGL-1, *J. Biol. Chem.* (2001), doi:10.1074/jbc.M105997200.

195. J. S. Merzaban, M. M. Burdick, S. Z. Gadhoum, N. M. Dagia, J. T. Chu, R. C. Fuhlbrigge, R. Sackstein, Analysis of glycoprotein E-selectin ligANDs on human and mouse marrow cells enriched for hematopoietic stem/progenitor cells, *Blood* **118**, 1774–1783 (2011).

196. D. A. Sultana, S. L. Zhang, S. P. Todd, A. Bhandoola, Expression of Functional P-Selectin Glycoprotein Ligand 1 on Hematopoietic Progenitors Is Developmentally Regulated, *J. Immunol.* (2012), doi:10.4049/jimmunol.1101116.

197. M. J. Mitchell, M. R. King, Shear-induced resistance to neutrophil activation via the formyl peptide receptor*Biophys. J.* (2012), doi:10.1016/j.bpj.2012.03.053.

198. D. Martinez, M. Vermeulen, A. Trevani, A. Ceballos, J. Sabatte, R. Gamberale, M. E. Alvarez, G. Salamone, T. Tanos, O. A. Coso, J. Geffner, Extracellular Acidosis Induces Neutrophil Activation by a Mechanism Dependent on Activation of Phosphatidylinositol 3-Kinase/Akt and ERK Pathways, *J. Immunol.* (2014), doi:10.4049/jimmunol.176.2.1163.

199. A. Lardner, The effects of extracellular pH on immune function., *J. Leukoc. Biol.* (2001).

200. D. N. Cook, The role of MIP-1α in inflammation and hematopoiesis*J. Leukoc. Biol.* (1996), doi:10.1002/jlb.59.1.61.

201. F. Mourkioti, N. Rosenthal, IGF-1, inflammation and stem cells: Interactions during muscle regeneration*Trends Immunol.* (2005), doi:10.1016/j.it.2005.08.002.

202. S. Amselem, R. Cohen, S. Druckmann, A. Gabizon, D. Goren, R. M. Abra, A. Huang, R. New, Y. Barenholz, Preparation and characterization of liposomal

doxorubicin for human use, *J. Liposome Res.* (1992), doi:10.3109/08982109209039903.

203. G. Haran, R. Cohen, L. K. Bar, Y. Barenholz, Transmembrane ammonium sulfate gradients in liposomes produce efficient and stable entrapment of amphipathic weak bases, *BBA - Biomembr.* (1993), doi:10.1016/0005-2736(93)90105-9.

204. M. J. Mitchell, C. S. Chen, V. Ponmudi, A. D. Hughes, M. R. King, E-selectin liposomal and nanotube-targeted delivery of doxorubicin to circulating tumor cells, *J. Control. Release* (2012), doi:10.1016/j.jconrel.2012.02.018.

205. M. J. Mitchell, C. A. Castellanos, M. R. King, Nanostructured Surfaces to Target and Kill Circulating Tumor Cells While Repelling Leukocytes, *J. Nanomater.* (2012), doi:10.1155/2012/831263.

206. Z. Huang, M. R. King, An immobilized nanoparticle-based platform for efficient gene knockdown of targeted cells in the circulation, *Gene Ther.* (2009), doi:10.1038/gt.2009.76.

207. M. B. Lawrence, T. A. Springer, Neutrophils roll on E-selectin., *J. Immunol.* (1993).

208. M. P. Bevilacqua, R. M. Nelson, Selectins*J. Clin. Invest.* (1993), doi:10.1172/JCI116210.

209. a W. Greenberg, W. G. Kerr, D. a Hammer, Relationship between selectin-mediated rolling of hematopoietic stem and progenitor cells and progression in hematopoietic development., *Blood* (2000).

210. J. C. Wojciechowski, S. D. Narasipura, N. Charles, D. Mickelsen, K. Rana, M. L.

Blair, M. R. King, Capture and enrichment of CD34-positive haematopoietic stem and progenitor cells from blood circulation using P-selectin in an implantable device, *Br. J. Haematol.* (2008), doi:10.1111/j.1365-2141.2007.06967.x.

211. N. Charles, J. L. Liesveld, M. R. King, Investigating the feasibility of stem cell enrichment mediated by immobilized selectins, *Biotechnol. Prog.* (2007), doi:10.1021/bp0702222.

212. A. D. Hughes, J. Mattison, J. D. Powderly, B. T. Greene, M. R. King, Rapid Isolation of Viable Circulating Tumor Cells from Patient Blood Samples, *J. Vis. Exp.* (2012), doi:10.3791/4248.

213. A. D. Rocheleau, T. M. Cao, T. Takitani, M. R. King, Comparison of human and mouse E-selectin binding to Sialyl-Lewisx, *BMC Struct. Biol.* **16** (2016) (available at https://bmcstructbiol.biomedcentral.com/track/pdf/10.1186/s12900-016-0060-x).

214. W. D. Hanley, Distinct kinetic and mechanical properties govern selectin-leukocyte interactions, *J. Cell Sci.* (2004), doi:10.1242/jcs.01088.

215. K. Ley, The role of selectins in inflammation and disease., *Trends Mol. Med.* (2003).

216. A. Titz, A. Marra, B. Cutting, M. Smieško, G. Papandreou, A. Dondoni, B. Ernst, Conformational constraints: Nature does it best with sialyl Lewis x, *European J. Org. Chem.* (2012), doi:10.1002/ejoc.201200744.

217. C. A. Pierse, O. K. Dudko, Kinetics and energetics of biomolecular folding and binding, *Biophys. J.* (2013), doi:10.1016/j.bpj.2013.09.023.

218. J. Lou, T. Yago, A. G. Klopocki, P. Mehta, W. Chen, V. I. Zarnitsyna, N. V.

Bovin, C. Zhu, R. P. McEver, Flow-enhanced adhesion regulated by a selectin interdomain hinge, *J. Cell Biol.* **174**, 1107–1117 (2006).

219. C. Zhu, T. Yago, J. Lou, V. I. Zarnitsyna, R. P. McEver, Mechanisms for flow-enhanced cell adhesion, *Ann. Biomed. Eng.* (2008), doi:10.1007/s10439-008-9464-5.

220. S. Lü, M. Long, Forced dissociation of selectin-ligand complexes using steered molecular dynamics simulation., *Mol. Cell. Biomech.* (2005).

221. Monticelli, *Biomolecular Simulations: Methods and Protocols* (2013).

222. M. R. King, D. A. Hammer, Multiparticle adhesive dynamics. Interactions between stably rolling cells, *Biophys. J.* (2001), doi:10.1016/S0006-3495(01)75742-6.

223. Y. Geng, K. Yeh, T. Takatani, M. R. King, Three to Tango: MUC1 as a Ligand for Both E-Selectin and ICAM-1 in the Breast Cancer Metastatic Cascade, *Front. Oncol.* (2012), doi:10.3389/fonc.2012.00076.

224. Y. Geng, S. Chandrasekaran, J. W. Hsu, M. Gidwani, A. D. Hughes, M. R. King, Phenotypic Switch in Blood: Effects of Pro-Inflammatory Cytokines on Breast Cancer Cell Aggregation and Adhesion, *PLoS One* (2013), doi:10.1371/journal.pone.0054959.

225. F. S. Legge, A. Budi, H. Treutlein, I. Yarovsky, Protein flexibility: Multiple molecular dynamics simulations of insulin chain B, *Biophys. Chem.* (2006), doi:10.1016/j.bpc.2005.08.002.

226. T. A. Springer, Structural basis for selectin mechanochemistry, *Proc. Natl. Acad. Sci. U. S. A.* **106**, 91–96 (2009).

227. N. Okimoto, N. Futatsugi, H. Fuji, A. Suenaga, G. Morimoto, R. Yanai, Y. Ohno,

T. Narumi, M. Taiji, High-performance drug discovery: Computational screening by combining docking and molecular dynamics simulations, *PLoS Comput. Biol.* (2009), doi:10.1371/journal.pcbi.1000528.

228. S. Cosconati, S. Forli, A. L. Perryman, R. Harris, D. S. Goodsell, A. J. Olson, Virtual screening with AutoDock: theory and practice, *Expert Opin. Drug Discov.* (2010), doi:10.1517/17460441.2010.484460.

229. T. A. Springer, Structural basis for selectin mechanochemistry, *Proc. Natl. Acad. Sci.* (2009), doi:10.1073/pnas.0810784105.

230. Y. Kang, S. Lü, P. Ren, B. Huo, M. Long, Molecular dynamics simulation of shear- and stretch-induced dissociation of P-selectin/PSGL-1 complex, *Biophys. J.* (2012), doi:10.1016/j.bpj.2011.11.4002.

231. M. T. Beste, D. A. Hammer, Selectin catch-slip kinetics encode shear threshold adhesive behavior of rolling leukocytes, *Proc. Natl. Acad. Sci.* **105**, 20716–20721 (2008).

232. M. R. King, V. Heinrich, E. Evans, D. A. Hammer, Nano-to-micro scale dynamics of P-selectin detachment from leukocyte interfaces. III. Numerical simulation of tethering under flow, *Biophys. J.* (2005), doi:10.1529/biophysj.104.051805.

233. H. Park, M. S. Yeom, S. Lee, Loop flexibility and solvent dynamics as determinants for the selective inhibition of cyclin-dependent kinase 4: Comparative molecular dynamics simulation studies of CDK2 and CDK4, *ChemBioChem* (2004), doi:10.1002/cbic.200400214.

234. D. Mao, S. Lü, N. Li, Y. Zhang, M. Long, Conformational stability analyses of alpha subunit I domain of LFA-1 and Mac-1, *PLoS One* (2011), doi:10.1371/journal.pone.0024188.

235. J. Shen, W. Zhang, H. Fang, R. Perkins, W. Tong, H. Hong, Homology modeling, molecular docking, and molecular dynamics simulations elucidated α-fetoprotein binding modes, *BMC Bioinformatics* (2013), doi:10.1186/1471-2105-14-S14-S6.

236. I. A. Vakser, Protein-protein docking: From interaction to interactome*Biophys. J.* (2014), doi:10.1016/j.bpj.2014.08.033.

237. K. Ley, C. Laudanna, M. I. Cybulsky, S. Nourshargh, Getting to the site of inflammation: The leukocyte adhesion cascade updated*Nat. Rev. Immunol.* **7**, 678–689 (2007).

238. C. J. Dimitroff, M. Lechpammer, D. Long-Woodward, J. L. Kutok, Rolling of human bone-metastatic prostate tumor cells on human bone marrow endothelium under shear flow is mediated by E-selectin, *Cancer Res.* **64**, 5261–5269 (2004).

239. K. Sakuma, M. Aoki, R. Kannagi, Transcription factors c-Myc and CDX2 mediate E-selectin ligand expression in colon cancer cells undergoing EGF/bFGF-induced epithelial-mesenchymal transition, *Proc. Natl. Acad. Sci.* **109**, 7776–7781 (2012).

240. V. A. Morikis, S. Chase, T. Wun, E. L. Chaikof, J. L. Magnani, S. I. Simon, Selectin catch-bonds mechanotransduce integrin activation and neutrophil arrest on inflamed endothelium under shear flow, *Blood* **130**, 2101–2110 (2017).

241. T. Yago, N. Zhang, L. Zhao, C. S. Abrams, R. P. McEver, Selectins and chemokines use shared and distinct signals to activate β2 integrins in neutrophils, *Blood Adv.* **2**, 731–744 (2018).

242. D. Tyrrell, P. James, N. Rao, C. Foxall, S. Abbas, F. Dasgupta, M. Nashed, A. Hasegawa, M. Kiso, D. Asa, Structural requirements for the carbohydrate ligand of E-selectin, *Proc Natl Acad Sci U S A* **88**, 10372–10376 (1991).

243. A. Levinovitz, J. Muhlhoff, S. Isenmann, D. Vestweber, Identification of a glycoprotein ligand for E-selectin on mouse myeloid cells, *J. Cell Biol.* **121**, 449–459 (1993).

244. R. C. Fuhlbrigge, S. L. King, R. Sackstein, T. S. Kupper, CD43 is a ligand for E-selectin on CLA+ human T cells, *Blood* **107**, 1421–1426 (2006).

245. A. Hidalgo, A. J. Peired, M. K. Wild, D. Vestweber, P. S. Frenette, Complete Identification of E-Selectin Ligands on Neutrophils Reveals Distinct Functions of PSGL-1, ESL-1, and CD44, *Immunity* **26**, 477–489 (2007).

246. B. J. Graves, R. L. Crowther, C. Chandran, J. M. Rumberger, S. Li, K. Sen Huang, D. H. Presky, P. C. Familletti, B. A. Wolitzky, D. K. Burns, Insight into E-selectin/ligand interaction from the crystal structure and mutagenesis of the lec/EGF domains, *Nature* **367**, 532–538 (1994).

247. R. C. Preston, R. P. Jakob, F. P. C. Binder, C. P. Sager, B. Ernst, T. Maier, E-selectin ligand complexes adopt an extended high-affinity conformation, *J. Mol. Cell Biol.* **8**, 67–72 (2016).

248. P. Mehta-D'souza, A. G. Klopocki, V. Oganesyan, S. Terzyan, T. Mather, Z. Li,

S. R. Panicker, C. Zhu, R. P. McEver, Glycan bound to the selectin low affinity state engages Glu-88 to stabilize the high affinity state under force, *J. Biol. Chem.* **292**, 2510–2518 (2017).

249. Y. V. Pereverzev, O. V. Prezhdo, E. V. Sokurenko, Allosteric role of the large-scale domain opening in biological catch-binding, *Phys. Rev. E - Stat. Nonlinear, Soft Matter Phys.* **79**, 051913 (2009).

250. S. B. Riese, C. Kuehne, T. F. Tedder, R. Hallmann, E. Hohenester, K. Buscher, Heterotropic Modulation of Selectin Affinity by Allosteric Antibodies Affects Leukocyte Rolling, *J. Immunol.* **192**, 1862–1869 (2014).

251. E. B. Finger, K. D. Purl, R. Alon, M. B. Lawrence, U. H. von Andrian, T. A. Springer, Adhesion through L-selectin requires a threshold hydrodynamic shear, *Nature* **379**, 266–269 (1996).

252. B. T. Marshall, M. Long, J. W. Piper, T. Yago, R. P. McEver, C. Zhu, Direct observation of catch bonds involving cell-adhesion molecules, *Nature* **423**, 190–193 (2003).

253. A. M. Wayman, W. Chen, R. P. McEver, C. Zhu, Triphasic force dependence of E-selectin/ligand dissociation governs cell rolling under flow, *Biophys. J.* **99**, 1166–1174 (2010).

254. J. Lou, C. Zhu, A structure-based sliding-rebinding mechanism for catch bonds, *Biophys. J.* **92**, 1471–1485 (2007).

255. T. T. Waldron, T. A. Springer, Transmission of allostery through the lectin domain in selectin-mediated cell adhesion, *Proc. Natl. Acad. Sci. U. S. A.* **106**, 85–90

(2009).

256. R. E. Mebius, S. R. Watson, L- and E-selectin can recognize the same naturally occurring ligands on high endothelial venules, *J Immunol* **151**, 3252–3260 (1993).

257. A. A. Gorfe, B. J. Grant, J. A. McCammon, Mapping the Nucleotide and Isoform-Dependent Structural and Dynamical Features of Ras Proteins, *Structure* **16**, 885–896 (2008).

258. X. Q. Yao, M. C. Cato, E. Labudde, T. S. Beyett, J. J. G. Tesmer, B. J. Grant, Navigating the conformational landscape of G protein–coupled receptor kinases during allosteric activation, *J. Biol. Chem.* **292**, 16032–16043 (2017).

259. O. Dwir, G. S. Kansas, R. Alon, An activated L-selectin mutant with conserved equilibrium binding properties but enhanced ligand recognition under shear flow, *J. Biol. Chem.* **275**, 18682–18691 (2000).

260. E. Evans, A. Leung, V. Heinrich, C. Zhu, Mechanical switching and coupling between two dissociation pathways in a P-selectin adhesion bond, *Proc. Natl. Acad. Sci.* **101**, 11281–11286 (2004).

261. I. W. Davis, A. Leaver-Fay, V. B. Chen, J. N. Block, G. J. Kapral, X. Wang, L. W. Murray, W. B. Arendall, J. Snoeyink, J. S. Richardson, D. C. Richardson, MolProbity: All-atom contacts and structure validation for proteins and nucleic acids, *Nucleic Acids Res.* **35**, W375–W383 (2007).

262. A. V Morozov, T. Kortemme, K. Tsemekhman, D. Baker, Close agreement between the orientation dependence of hydrogen bonds observed in protein structures and quantum mechanical calculations, *Proc. Natl. Acad. Sci.* **101**, 6946–6951 (2004).

263. O. Schueler-Furman, C. Wang, P. Bradley, K. Misura, D. Baker, Progress in modeling of protein structures and interactions*Science (80-.).* **310**, 638–642 (2005).

264. B. J. Grant, A. P. C. Rodrigues, K. M. ElSawy, J. A. McCammon, L. S. D. Caves, Bio3d: An R package for the comparative analysis of protein structures, *Bioinformatics* **22**, 2695–2696 (2006).

265. E. F. Pettersen, T. D. Goddard, C. C. Huang, G. S. Couch, D. M. Greenblatt, E. C. Meng, T. E. Ferrin, UCSF Chimera - A visualization system for exploratory research and analysis, *J. Comput. Chem.* **25**, 1605–1612 (2004).